

# COMPUTER-ASSISTED GLOBAL ANALYSIS FOR VIBRO-IMPACT DYNAMICS: A REDUCED SMOOTH MAPS APPROACH \*

LANJING BAO<sup>†</sup>, RACHEL KUSKE<sup>‡</sup>, DANIIL YURCHENKO<sup>§</sup>, AND IGOR BELYKH<sup>¶</sup>

**Abstract.** We present a novel approach for studying the global dynamics of a vibro-impact pair, that is, a ball moving in a harmonically forced capsule. Motivated by a specific context of vibro-impact energy harvesting, we develop the method with broader non-smooth systems in mind. The seeming complications of the impacts of the ball with the capsule are exploited as useful non-smooth features in selecting appropriate return maps. This choice yields a computationally efficient framework for constructing return maps on short-time realizations from the state space of possible initial conditions rather than via long-time simulations often used to generate more traditional maps. The different dynamics in sub-regions in the state space yield a small collection of reduced polynomial approximations. Combined into a piecewise composite map, these capture transient and attracting behaviors and reproduce bifurcation sequences of the full system. Further “separable” reductions of the composite map provide insight into both transient and global dynamics. This composite map is valuable for cobweb analysis, which opens the door to computer-assisted global analysis and is realized via conservative auxiliary maps based on the extreme bounds of the maps in each subregion. We study the global dynamics of energetically favorable states and illustrate the potential of this approach in broader classes of dynamics.

**Key words.** Non-smooth dynamics, Vibro-impact system, Global dynamics, Reduction methods, Auxiliary maps

**AMS subject classifications.** 58-08

**1. Introduction.** The prevalence of non-smooth dynamics, characterized by switches, impacts, sliding, and other abrupt alterations in behavior, permeates various fields, including physics, biology, and engineering [3, 21, 15]. Non-smooth dynamical models are essential for understanding phenomena such as body component interactions with non-smooth contacts, impacts, friction, and switching in mechanical systems [17, 49, 32, 5], and relay systems, switched power converters, and packet-switched networks in electrical and control engineering [17, 18, 9, 24]. In the life sciences, non-smooth dynamics are evident in diverse systems such as gene regulatory networks [43, 1] and pulse-coupled neurons [20]. While piecewise smooth, non-smooth, and vibro-impact dynamical systems represent vast research fields in nonlinear science, historically, non-smooth systems have received far less attention than their smooth counterparts. In recent decades, increased efforts have pursued a comprehensive understanding of non-smooth bifurcations and related nonlinearities (see extensive reviews [15, 26, 27, 6] and references therein).

Vibro-impact (VI) systems constitute a distinct class of dynamical systems where impacts substantially influence the nonlinear behavior. Typical classes of VI systems include a forced mass and one or more stationary rigid barriers or, alternatively, a pair of moving impacting masses, each of which may be subject to external forcing. Classic examples include balls bouncing on moving surfaces [36, 32, 31], pendulums impacting barriers [50, 16], and VI pairs composed of two oscillating masses that impact each other [37]. Generally, both masses in the VI pair may undergo forcing, complemented by elastic or inelastic impacts. A canonical VI pair, considered in this paper, consists of a forced capsule, with an inner mass moving freely within a cavity of a given length and impacting the ends of the capsule. This concept has been explored as an effective vibration mitigation alternative to linear tuned mass dampers or continuous nonlinear dampers [56, 54, 58, 39, 33, 34, 13, 38]. Recently, a VI pair was proposed as an energy harvesting mechanism, where the impacts between the inner mass and the capsule deform flexible dielectric polymer membranes on the capsule ends [57]. These membranes serve as capacitors, as the impacts deform them and change their capacitance, thus enabling energy harvesting [30]. Previously VI pairs have been studied by approximate methods, including averaging, multiple scales, and complexification averaging [19, 25, 34, 55], but with limited applicability to non-smooth systems with impacts.

---

\* This work was supported by the National Science Foundation (USA) under collaborative grants No. CMMI-2009329 and CMMI 2009270, and Engineering and Physical Sciences Research Council (UK) under grant EPSRC EP/V034391/1.

<sup>†</sup>Department of Mathematics and Statistics, Georgia State University, P.O. Box 4110, Atlanta, Georgia, 30302-410, USA (lbao1@student.gsu.edu)

<sup>‡</sup>School of Mathematics, Georgia Institute of Technology, 686 Cherry Street Atlanta, GA 30332-0160 USA (rachel@math.gatech.edu)

<sup>§</sup>Institute for Sound and Vibration Research, University of Southampton, (d.yurchenko@soton.ac.uk)

<sup>¶</sup>Department of Mathematics and Statistics and Neuroscience Institute, Georgia State University, P.O. Box 4110, Atlanta, Georgia, 30302-410, USA (ibelykh@gsu.edu)

44 Recently, VI pair systems have been studied precisely using maps, combining the system’s motion be-  
45 tween the impacts and the impact conditions. The semi-analytical solution of these exact equations can  
46 provide exhaustive information regarding the bifurcation structure and local stability of different types of  
47 motion. In the case when the smaller mass is negligible relative to the larger one this two-degree-of-freedom  
48 system can be reduced to a single differential equation for the relative displacement of the two masses [46, 37],  
49 used to explore, e.g., the interplay between classical and grazing bifurcations [48] and comparisons of instan-  
50 taneous and compliant impact conditions [12]. In settings where the smaller mass is non-negligible, such as  
51 in targeted energy transfer, exact maps for the full system allow bifurcation analyses over a large range of  
52 parameters for modes with efficient energy transfer and their loss of stability to inefficient alternating chatter  
53 behaviors [28].

54 These previous map-based results are primarily based on linear stability analyses, leaving a critical gap  
55 in analyzing the global, possibly chaotic dynamics of VI systems due to severe limitations of the existing  
56 global stability methods in handling impacts. One contributing factor for the forced VI pair is the fact it is  
57 non-autonomous, yielding analytically intractable coupled transcendental maps for the system response and  
58 impact time that prevent explicit expressions for the state of the system.

59 In a broader context, global stability approaches for non-autonomous, non-smooth systems are few and  
60 far between. One notable example is an extension of the Lyapunov function method to prove the global  
61 stability of the equilibrium state of a non-autonomous bouncing ball [31]. In this setting, the Lyapunov-type  
62 method involves non-autonomous measure differential inclusions and constructs a decreasing step function  
63 above an oscillating Lyapunov function. However, its application to non-trivial dynamics of VI pairs with two-  
64 sided impacts seems elusive. Another notable sample is an averaging Lyapunov function approach developed  
65 to prove global convergence to absorbing domains of non-trivial attractors in non-smooth dynamical systems  
66 with a non-autonomous stochastic switching parameter rule [24]. However, this approach is not relevant for  
67 non-autonomous VI systems as it is based on knowledge of the averaged autonomous system’s attractor.  
68 Recently, a computer-assisted proof of chaos in piecewise linear maps was obtained by explicit construction  
69 of trapping regions and invariant cones based on word sets representing the dynamics symbolically [52]. An  
70 area-preserving map-based analysis for the global behavior of a rare, restricted behavior of the VI pair was  
71 proposed in [10]. Yet, to date, there appear to be no global analyses relevant to applications such as energy  
72 harvesting, for which the VI pair dynamics of interest include sustained sequences of regular impacts on both  
73 barriers at the capsule ends, observed over a large range of parameters. Then, we are faced with the challenge  
74 of global analyses of behavior with at least two (alternating) impacts per forcing cycle. This feature is in  
75 contrast with other studies of impacting systems that may consider the transition between no impacts and  
76 a single impact [40], repeated impacts on a single barrier [53], or the global attraction of a solution without  
77 impacts [31].

78 In this paper, we present a novel computer-assisted approach for studying the global dynamics of the  
79 VI pair, that is, a ball moving in a harmonically forced capsule. Motivated to develop an analytical global  
80 analysis for this system, we prioritize approaches that include explicit expressions wherever possible. We  
81 exploit the seeming complications of the sustained impacts of the ball with the capsule as useful non-  
82 smooth features in constructing two-dimensional (2D) return maps that can characterize global dynamics  
83 and bifurcations of the VI pair. Computationally efficient short-time realizations of these return maps  
84 divide the state space according to different dynamics. Our definition of return maps does not fall into  
85 standard choices for maps, such as Poincaré, stroboscopic, all impacts, or all returns to a particular state  
86 [37, 40, 42, 51]. Instead, it divides the return maps based on the sequence of impacts that do or do not  
87 occur before the system returns to a particular impacting state. This innovative perspective is valuable for  
88 efficiently partitioning the state space into a small number of regions from which it is straightforward to  
89 identify attracting and transient behavior. Based on the behavior in each region, we then define reduced  
90 polynomial approximations for the maps in each region.

91 Combining these polynomials into a piecewise smooth composite map, we demonstrate that it captures  
92 transient behaviors throughout the state space while reproducing the attracting behaviors. Furthermore, it  
93 reproduces an important sequence of period-doubling bifurcations and (apparently) chaotic behavior com-  
94 pared with the bifurcation sequences of the exact systems. In constructing the composite map, we find that  
95 in some regions with strongly transient dynamics, we can reduce the 2D return maps to a pair of 1D return  
96 maps without sacrificing the integrity of the attracting dynamics. While not a necessary step, these types of  
97 “separable” components of the composite map provide transparency for the overall dynamics. Furthermore,

98 this composite map derived from the non-smooth VI dynamics is remarkably valuable for cobweb analysis,  
99 as it is based on simple return maps corresponding to impacts on one end of the capsule rather than on  
100 compositions of map sequences. Specifically, the separable representations of the 2D map are convenient for  
101 visualizations within this cobweb phase analysis that captures the different attracting behaviors for different  
102 parameter regimes.

103 Notably, this cobweb analysis motivates a valuable definition of auxiliary maps on the regions identified  
104 within the construction of the composite map once the transient and attracting characteristics have been  
105 identified. For regions with attracting dynamics, the auxiliary map is conservatively based on the extreme  
106 bounds on the map for each region and thus can be used to bound the attracting domain. A key feature of the  
107 auxiliary maps is that they simplify the 2D return maps into a set of 1D equations using the bounds for each  
108 region. Then, a cobweb phase space analysis is used to explore the system’s long-term dynamics. Repeated  
109 application of the auxiliary maps, each with updated bounds obtained from the previous application, yields  
110 a limiting multi-period cycle that bounds the attracting domain. With the auxiliary maps based on the  
111 polynomial approximations, we can obtain analytical expressions for the impact velocity map and, thus, for  
112 the attracting domain.

113 We outline the process of generating the approximate composite map in terms of a general algorithm  
114 adaptable for other non-smooth dynamical systems. A key step in the algorithm includes identifying short  
115 sequences of impacts that give the building blocks for the return maps. The resulting division of the state  
116 space is relatively simple and computationally efficient compared to, e.g., the identification of basins of  
117 attraction, which require long time computations to find complex regions for dynamics sensitive to initial  
118 conditions. Likewise, flow-defined Poincaré maps for the global dynamics of periodic and chaotic systems,  
119 derived from long-time simulations over the entire state space, are often piecewise smooth even though  
120 they originate from a smooth dynamical system. Geometrical piecewise smooth Lorenz maps [2, 44, 23]  
121 representing the smooth chaotic dynamics of the Lorenz system are notable examples. Our approximate  
122 composite map constructed for only short-time realizations of the VI pair is conceptually different from  
123 classical piecewise smooth maps with regular and chaotic dynamics appearing in various biological, social  
124 science, and engineering applications [41, 4, 59, 8, 11, 22, 14]. However, it can still be interpreted as a  
125 geometrical model of the VI pair as it depicts the dynamics and bifurcations remarkably well and derives from  
126 a polynomial approximation of the state space partitions. The combination of the geometric interpretation  
127 and the polynomial approximation facilitates our goal of obtaining analytical results for the global dynamics  
128 directly related to the physical model. These results are in contrast to local analyses and computational  
129 studies of higher dimensional maps [42, 45].

130 In this first development of the approach, we focus on parameter regimes for behaviors that drive  
131 favorable energy output in a VI pair-based energy harvesting device, behaviors with alternating impacts on  
132 either end of the capsule. The impact velocity and phase may repeat periodically with period  $n\mathcal{T}$ , where  
133  $\mathcal{T}$  is the period of the forcing, or the states may have apparently chaotic behavior within the alternating  
134 behavior. Besides its physical relevance, this choice of parameters facilitates a relatively straightforward  
135 presentation of the approach while exploring several types of non-trivial dynamics. Nevertheless, we expect  
136 that foundational concepts in this analysis are adaptable to other (more complex) sequences of impacts, as  
137 discussed further in the conclusions.

138 The remainder of the paper is organized as follows. Section 2 gives details of the VI pair model, including  
139 the transcendental form of the maps [47, 48] that motivates the computer-assisted analysis of global dynam-  
140 ics. Section 3 provides the return maps that form the building blocks of the computer-assisted approach,  
141 illustrating their key properties. Section 4 provides the general algorithm for constructing a composite map  
142 realized for the VI pair by approximating the return maps with explicit piecewise polynomial maps over  
143 relevant regions that comprise the state space. Section 5 compares the trajectories generated using the exact  
144 and composite maps in the state space and the phase plane. Section 6 develops an auxiliary map based  
145 on the composite map to identify the globally attracting dynamics and the corresponding domain for three  
146 qualitatively different types of the VI pair system behavior. Section 7 contains conclusions and a brief illus-  
147 tration of the relevance of the approach for a VI pair-based energy harvesting device with stochastic forcing.  
148 Finally, Appendix A provides additional details on the construction of the return map. The supplementary  
149 material contains the exact map derivation and demonstrates its analytical intractability. It also contains  
150 the coefficients of the polynomials used in the composite map.

151 **2. The Model.** The model takes the form of the canonical impact pair, comprised of an externally  
 152 forced capsule with a freely moving ball inside. The friction between the ball and the capsule is neglected,  
 153 so the ball's motion is driven purely by gravity and impacts one of the membranes on the capsule's ends.

154 One application based on the impact pair is a nonlinear vibro-impact energy harvesting device. Each  
 155 end of the capsule is closed by a membrane of dielectric (DE) polymer material with compliant electrodes  
 156 [57]. The deformation of such a DE membrane is the vibro-impact energy harvesting device's primary means  
 157 of energy generation. When the ball collides with the membrane, this action changes the ball's trajectory  
 158 and deforms the membrane. The DE membrane's physical property, being a variable capacitance capacitor,  
 159 allows the change of its capacitance when it is deformed; meanwhile, a bias voltage is applied when the  
 160 deformation reaches its maximum state. After the collision, an extra voltage charge is harvested, and the  
 161 membrane returns to its undeformed state.

162 The schematic for the VI pair is given in Fig. 1(a). Neglecting the friction, the system is driven by  
 163 forces generated at impact, gravity, and external harmonic excitation  $\hat{F}(\omega\tau + \psi)$  with period  $2\pi/\omega$ . Using  
 164 Newton's Second Law of Motion, the model is described by the following differential equations:

$$165 \quad (2.1) \quad \frac{d^2 X}{d\tau^2} = \frac{\hat{F}(\omega\tau + \psi)}{M},$$

$$166 \quad (2.2) \quad \frac{d^2 x}{d\tau^2} = -g \sin \beta,$$

168 where  $X(\tau)$  and  $x(\tau)$  are the dependent variables for the absolute displacement for the capsule and the ball,  
 169 respectively. In addition,  $M$  and  $m$  are the mass of the capsule and the ball, respectively.

170 Treating the impact time as negligible compared to other time scales in the model, we use an instanta-  
 171 neous impact model given by

$$172 \quad (2.3) \quad \left(\frac{dx}{d\tau}\right)^+ = -r \left(\frac{dx}{d\tau}\right)^- + (1+r) \left(\frac{dX}{d\tau}\right).$$

173 Note that this is a reduced model based on the condition  $M \gg m$ , as discussed in detail in [47]. The  
 174 superscripts  $+$  and  $-$  signify the state of the ball after and before the impact, respectively. The parameter  
 175  $r$  is the restitution coefficient, which is a quantitative measure of the membrane's elasticity. The range of  
 176  $r$  is  $[0, 1]$  with  $r = 1$  being perfectly elastic and  $r = 0$  being inelastic. In this paper, we consider moderate  
 177 elasticity  $r = 0.5$ . Additionally, in (2.3), we do not distinguish the states before and after the impact for  
 178 the capsule  $dX/d\tau$  because the mass of the ball ( $M \gg m$ ) is negligible and does not change the state of the  
 179 capsule at impact.

180 To focus on the system's dependence on key parameters, we first non-dimensionalize the system. Fol-  
 181 lowing [47], the dimensionless variables  $X^*(t), \dot{X}^*(t), t$  are the following:

$$182 \quad (2.4) \quad X(\tau) = \frac{\|\hat{F}\| \pi^2}{M\omega^2} \cdot X^*(t), \quad \frac{dX}{d\tau} = \frac{\|\hat{F}\| \pi}{M\omega} \cdot \dot{X}^*(t), \quad \tau = \frac{\pi}{\omega} \cdot t,$$

183 where  $\|\hat{F}\|$  is an appropriately defined norm of the strength of the forcing  $\hat{F}$ . Here, we also use Newton's  
 184 dot notation for differentiation when the derivative is calculated with respect to dimensionless time  $t$ .

185 In addition to non-dimensionalization, relative variables are used to focus on the system dynamics as  
 186 a whole, rather than the separate motion of the ball and capsule. Using the variables  $X^*$ , the relative  
 187 displacement  $Z(t)$  and relative velocity  $\dot{Z}(t)$  are given in the dimensionless form:

$$188 \quad Z = X^* - x^*, \quad \dot{Z} = \dot{X}^* - \dot{x}^*,$$

$$189 \quad (2.5) \quad \ddot{Z} = \ddot{X}^* - \ddot{x}^* = F(\pi t + \psi) + \frac{Mg \sin \beta}{\|\hat{F}\|} = f(t) + \bar{g},$$

190 where the non-dimensional forcing  $F(\pi t + \psi) = \frac{\hat{F}(\omega\tau + \psi)}{\|\hat{F}\|}$  has the unit norm, i.e.  $\|F\| = 1$ .

191 Since we want to evaluate the system from one impact to the next, the system's state at each impact is  
 192 particularly important. Combining conditions (2.4), (2.5), the impact condition (2.3) can be rewritten using

193  $Z$  and  $\dot{Z}$ . For the  $j^{\text{th}}$  impact occurring at time  $t = t_j$ ,

194 
$$Z_j = X^*(t_j) - x^*(t_j) = \pm \frac{d}{2}, \quad \text{for } x \in \partial B \ (\partial T) \text{ the sign is } + \ (-),$$

195 (2.6) 
$$\dot{Z}_j^+ = -r\dot{Z}_j^-, \quad d = \frac{sM\omega^2}{\|\hat{F}\| \pi^2}.$$

196

197 The notations  $\partial B$  and  $\partial T$  denote the bottom and top membranes, respectively. The parameter  $d$  is the  
 198 dimensionless length of the system, used throughout this paper as the bifurcation parameter. In contrast to  
 199 the actual length of the capsule  $s$ ,  $d$  varies with multiple factors, including the device length ( $s$ ), mass ( $M$ ),  
 200 angular velocity of the external force ( $\omega$ ), and forcing strength ( $\|\hat{F}\|$ ). As illustrated in Fig. 1(b),(c), the  
 201 relative position of the system is bounded,  $Z(t) \in [-d/2, d/2]$ . At the impacts, which is when  $Z_j = \pm d/2$ ,  
 202 the relative velocity  $\dot{Z}_j$  changes sign: when the impact is on  $\partial B$  ( $Z_j = d/2$ ),  $\dot{Z}$  changes from positive to  
 203 negative; when the impact is on  $\partial T$  ( $Z_j = -d/2$ ),  $\dot{Z}$  switches from negative to positive. To complete the  
 204 definition of the state of the system at impact, we then need to determine  $(\dot{Z}_j, t_j)$ .

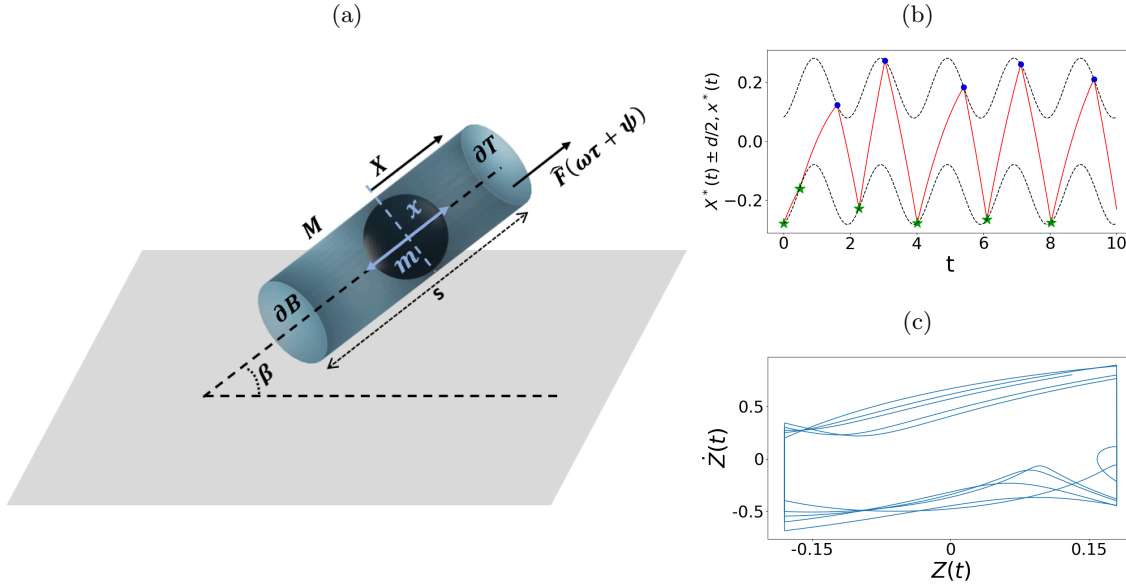


Fig. 1: (a): Illustration of the VI pair: A ball moves freely within a harmonically forced capsule enclosed by deformable membranes on both ends. The capsule is positioned with an angle  $\beta$  relative to the horizontal plane and is excited by an external harmonic excitation  $\hat{F}(\omega\tau + \psi)$ . The mass, length of the capsule, and mass of the ball are  $M$ ,  $s$ , and  $m$ , respectively. (b): The two dashed black lines represent the displacement of the top and bottom membranes,  $X(t)^* \pm d/2$ . The green stars and blue dots indicate the impacts at  $\partial B$  and  $\partial T$ , respectively. The red solid lines connect each impact at  $\partial T$  and  $\partial B$ , representing the estimated ball movement between each impact. (c): Phase plane in terms of relative variables. The relative displacement  $Z(t)$  oscillates between  $-d/2$  and  $d/2$ , and the relative velocity  $\dot{Z}(t)$  has a sign change at each impact. Parameters:  $d = 0.35$ ,  $\dot{Z}_0 = 0.43$  and  $\psi_0 = 0.26$ .

205 We summarize results from [47] for calculating the exact maps for  $(\dot{Z}_j, t_j)$  between two consecutive  
 206 impacts. Between the impact at  $t_j$  and the next impact at  $t_{j+1}$ , the relative velocity and displacement can  
 207 be derived by integrating (2.5) for  $t \in (t_j, t_{j+1})$  and applying (2.6):

208 
$$\dot{Z}(t) = -r\dot{Z}_j^- + \bar{g} \cdot (t - t_j) + F_1(t) - F_1(t_j),$$

209 (2.7) 
$$Z(t) = Z_j^+ - r\dot{Z}_j^- \cdot (t - t_j) + \frac{\bar{g}}{2} \cdot (t - t_j)^2 + F_2(t) - F_2(t_j) - F_1(t_j) \cdot (t - t_j),$$

210

211 where  $F_1(t) = \int F(\pi t + \psi) dt$  and  $F_2(t) = \int F_1(t) dt$ . At the  $j^{\text{th}}$  impact,  $Z_j^+ = Z_j^-$ . Therefore, the  
 212 superscripts in  $\dot{Z}^\pm$  are omitted, since (2.7) are in terms  $Z^-$  and  $\dot{Z}^-$  only. Using the equations (2.7), there  
 213 are four basic nonlinear maps  $P_{BB}, P_{BT}, P_{TB}, P_{TT}$  corresponding to motion between consecutive impacts,  
 214 in terms of the four combinations of impact locations:  $\partial B \rightarrow \partial B$ ,  $\partial B \rightarrow \partial T$ ,  $\partial T \rightarrow \partial B$ ,  $\partial T \rightarrow \partial T$ . All  
 215 four maps take the form

$$216 \quad \dot{Z}_{j+1} = -r\dot{Z}_j + \bar{g} \cdot (t_{j+1} - t_j) + F_1(t_{j+1}) - F_1(t_j),$$

$$217 \quad (2.8) \quad \pm \frac{d}{2} = \pm \frac{d}{2} - r\dot{Z}_j \cdot (t_{j+1} - t_j) + \frac{\bar{g}}{2} \cdot (t_{j+1} - t_j)^2 + F_2(t_{j+1}) - F_2(t_j) - F_1(t_j) \cdot (t_{j+1} - t_j).$$

219 Notice, the sign for  $\pm d/2$  is chosen depending on the impact locations of  $Z_j, Z_{j+1}$ , + (-) for  $\partial B$  ( $\partial T$ ).

220 Ideally, we would like to transform (2.8) into closed-form expressions for  $(\dot{Z}_{j+1}, t_{j+1})$  in terms of  $(\dot{Z}_j, t_j)$ ,  
 221 which can be used to analyze stability and other (global) dynamic properties of these maps and their  
 222 compositions. Furthermore, if we wish to determine the map for the first return to  $\partial B$  for sequences as  
 223 shown in Fig. 1(b),(c), we would seek the exact map for the impact sequence  $\partial B \rightarrow \partial T \rightarrow \partial B$ , or for two  
 224 consecutive impacts on  $\partial B$ , which we refer to as BTB or BB motion, respectively. Here, we use the simpler  
 225 case of BB motion to demonstrate the difficulties in deriving closed-form expressions for such sequences. The  
 226 map  $P_{BB}$  is given by (2.8), using  $Z_{j+1} = Z_j = d/2$ , we have

$$227 \quad \dot{Z}_{j+1} = -r\dot{Z}_j + \bar{g} \cdot (t_{j+1} - t_j) + F_1(t_{j+1}) - F_1(t_j),$$

$$228 \quad (2.9) \quad \frac{d}{2} = \frac{d}{2} - r\dot{Z}_j \cdot (t_{j+1} - t_j) + \frac{\bar{g}}{2} \cdot (t_{j+1} - t_j)^2 + F_2(t_{j+1}) - F_2(t_j) - F_1(t_j) \cdot (t_{j+1} - t_j).$$

230 For concreteness, we take  $F(\pi t + \psi) = \cos(\pi t + \psi)$ . Then  $F_1(t) = \frac{1}{\pi} \sin(\pi t + \psi)$  and  $F_2(t) = -\frac{1}{\pi^2} \cos(\pi t + \psi)$ .  
 231 Substituting these into (2.9) and solving for  $(\dot{Z}_{j+1}, t_{j+1})$ , we have

$$232 \quad (2.10) \quad \dot{Z}_{j+1} = -r\dot{Z}_j + \bar{g}t_{j+1} - \bar{g}t_j + \frac{1}{\pi} \sin(\pi t_{j+1} + \psi) - \frac{1}{\pi} \sin(\pi t_j + \psi),$$

$$233 \quad (2.11) \quad 0 = -r\dot{Z}_j t_{j+1} + r\dot{Z}_j t_j + \frac{\bar{g}}{2} t_{j+1}^2 - \bar{g} t_{j+1} t_j + \frac{\bar{g}}{2} t_j^2 - \frac{1}{\pi^2} \cos(\pi t_{j+1} + \psi) + \frac{1}{\pi^2} \cos(\pi t_j + \psi)$$

$$234 \quad - \frac{1}{\pi} \sin(\pi t_j + \psi) t_{j+1} + \frac{1}{\pi} \sin(\pi t_j + \psi) t_j.$$

236 In (2.10),  $\dot{Z}_{j+1}$  is a function of  $\dot{Z}_j, t_j$ , as well as  $t_{j+1}$ , determined from (2.11). Sorting terms containing  $t_{j+1}$   
 237 to simplify (2.11) yields

$$238 \quad \frac{\bar{g}}{2} t_{j+1}^2 - \left( r\dot{Z}_j + \bar{g}t_j + \frac{1}{\pi} \sin(\pi t_j + \psi) \right) t_{j+1} + \left( r\dot{Z}_j t_j + \frac{\bar{g}}{2} t_j^2 + \frac{1}{\pi^2} \cos(\pi t_j + \psi) + \frac{t_j}{\pi} \sin(\pi t_j + \psi) \right)$$

$$239 \quad (2.12) \quad = \frac{1}{\pi^2} \cos(\pi t_{j+1} + \psi).$$

241 Equation (2.12) has a solution if the quadratic function on the left-hand side (LHS) and the cosine function  
 242 on the right-hand side (RHS) intersect. However, it is impossible to get a closed form expression for  $t_{j+1}$   
 243 and consequently not possible to get a closed form expression for  $\dot{Z}_{j+1}$ . Further details of the derivation of  
 244 the equations for the maps can be found in Supplementary Section I.

245 For the BTB case, the same hurdle arises. In that case, the BTB motion is composed of maps  $P_{TB} \circ$   
 246  $P_{BT}$ , and therefore a closed form first return map for  $\partial B$  would require the composition of expressions for  
 247  $(\dot{Z}_{j+1}, t_{j+1})$  and  $(\dot{Z}_{j+2}, t_{j+2})$ . The only difference in the equations for these quantities is the sign of  $\pm d/2$   
 248 in (2.9), so the lack of closed-form expressions follows as in (2.12). Therefore, we propose a computational  
 249 method to reduce this non-smooth map to a composition of smooth maps using explicit polynomials.

250 **3. Identification and visualization of the return maps.** The non-smooth maps derived above are  
 251 based on the system (2.7), which gives the exact map when evaluated at impact times  $t = t_j$ ; specifically,  
 252  $P_\ell : (\dot{Z}_j, t_j) \rightarrow (\dot{Z}_{j+1}, t_{j+1})$  for  $\dot{Z}_j = \dot{Z}(t_j)$ . This formulation is useful when determining conditions for  
 253 periodic solutions with a fixed number of impacts, and their local stability. For example, as in [47], a  
 254 composition of a fixed number of maps provides the basis for previous analyses of periodic solutions, and the

255 corresponding linear stability analysis provides information about whether the periodic solutions are stable  
 256 under small perturbations. In this previous work, different types of motion were generally categorized as  
 257  $n:m/p\mathcal{T}$ , where  $n$  and  $m$  are the numbers of impacts on  $\partial B$  and  $\partial T$ , respectively,  $\mathcal{T}$  is the excitation period,  
 258 and  $p$  is an integer number. Furthermore, the impact pair has been demonstrated to yield  $n:m/p\mathcal{T}$  and  
 259  $n:m/C$  behaviors, with  $C$  indicating complex, aperiodic, or chaotic behavior.

260 Figure 2 shows the relative impact velocity  $\dot{Z}_k$  on  $\partial B$ , corresponding to a sequence of bifurcations with  
 261  $1:1/\mathcal{T}$ ,  $1:1/p\mathcal{T}$  for  $p$  an even integer, and  $1:1/C$  behavior over a range of the dimensionless length  $d$ . (Note:  
 262 relative impact velocity on  $\partial T$  not shown.) We focus here on the parameters and the range of  $d$  yielding  
 263  $1:1$ -type behavior, with impacts alternating between  $\partial B$  and  $\partial T$  that is typically favorable for energy output,  
 264 and observed for the system (2.1)-(2.3) over a large range of parameters [47, 48].

265 **Remark 3.1.** *The numerical results in the bifurcation diagram (Fig. 2) are generated by solving (2.1)-(2.3)*  
 266 *over a long time, recording the limiting values for  $\dot{Z}_k$  and  $\psi_k$  on  $\partial B$  for each value of  $d$ . The attracting state*  
 267 *then serves as the initial condition for the next value of  $d$ , using a continuation-type method with decreasing  $d$ .*  
 268 *Throughout this paper, the parameters used to generate the simulations are the following:  $r = 0.5$ ,  $\|\hat{F}\| = 5$ ,*  
 269  *$M = 124.5$  g,  $\omega = 5\pi$ ,  $\beta = \pi/3$ ,  $g = 9.8$  m/s<sup>2</sup>. Here, the non-dimensional parameter  $d$  varies with the length*  
 270 *of the capsule  $s$ , as given in (2.6).*

271 While the previous analyses capture the local stability of branches corresponding to periodic solutions,  
 272 they do not provide information about the global attraction of this behavior or the potential for other  
 273 attracting behavior. In contrast, here, we seek to provide global stability results for the attraction of  
 274 different types of solutions, including periodic, nearly periodic, and chaotic behavior. As shown in Fig. 2,  
 275 we proceed with the variables  $(\dot{Z}_k, \psi_k)$ , where  $\psi_k$  is the relative phase of the exact map at impact and  $\psi_k =$   
 276  $\text{mod}(\pi t_k + \psi, 2\pi)$ , as  $\psi_k$  is more amenable than  $t_k$  for considering transients as well as (quasi)-periodic  
 277 behavior.

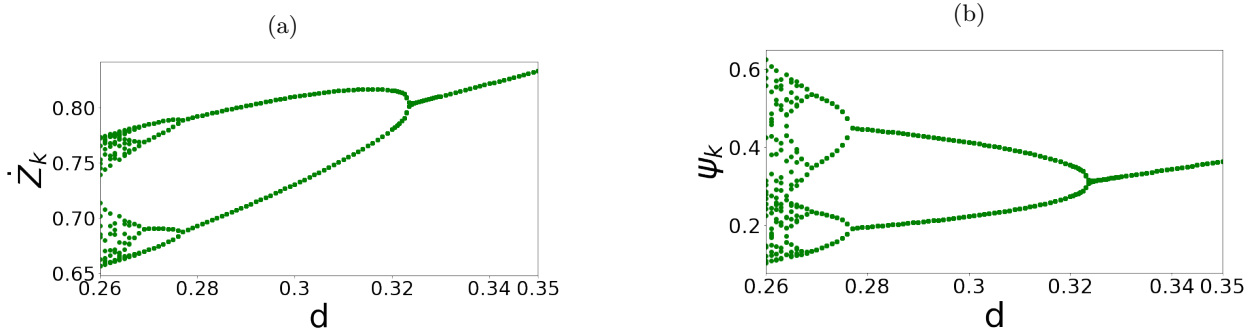


Fig. 2: Bifurcation diagrams for  $\dot{Z}_k$  and  $\psi_k$  generated using the exact map from system (2.7).

278 There are three key elements to our generalizable approach to the maps:

- 279 1. We exploit the non-smooth impact events in the dynamics, leading to the observation that any  
 280 transient behavior can be broken down into a sequence of a small number of types of return maps  
 281 to  $\partial B$ , as shown in Fig. 1(b): those that impact  $\partial T$  between sequential impacts on  $\partial B$ , and those  
 282 that do not.
- 283 2. The second key element is the ability to approximate these return maps with polynomial functions.
- 284 3. We focus on return maps, in contrast to those in (2.7)-(2.8), for which a valuable phase plane analysis  
 285 follows naturally.

286 With sequential impacts on  $\partial B$  as a natural framework for defining the maps, we focus on the first  
 287 return maps to  $\partial B$  captured by  $P_{BTB}$  and  $P_{BB}$ . While above, we have used the subscripts  $j$  and  $k$  somewhat  
 288 generically for impacts, for clarity with respect to the maps in (2.7)-(2.8), we reserve the subscripts  $j, j+1, \dots$   
 289 for sequential impacts on either  $\partial B$  or  $\partial T$ . Then, for the sequential impacts on  $\partial B$  only, in the following we  
 290 use the subscripts  $k, k+1, \dots$ , so that for  $k = j$  and  $P_{BTB}$  ( $P_{BB}$ ), the  $(k+1)^{\text{st}}$  impact on  $\partial B$  corresponds  
 291 to the  $j+2^{\text{nd}}$  ( $j+1^{\text{st}}$ ) impact. That is, for  $Z_j \in \partial B$ ,

292

$$P_{\text{BTB}} : (\dot{Z}_j, \psi_j) \rightarrow \{(\dot{Z}_{j+2}, \psi_{j+2}) \mid Z_{j+1} \in \partial T, Z_{j+2} \in \partial B\},$$

293 (3.1)

$$P_{\text{BB}} : (\dot{Z}_j, \psi_j) \rightarrow \{(\dot{Z}_{j+1}, \psi_{j+1}) \mid Z_{j+1} \in \partial B\}.$$

294 Note, for physical clarity, we have slightly abused notation in (3.1), using  $Z_j \in \partial B$  and  $Z_j \in \partial T$  for impacts  
 295 on either end of the capsule, in place of  $Z_j = \pm d/2$  as discussed following (2.6).

296 As illustrated in Fig. 1(b), the sequence length, for example, to (nearly) periodic behavior is not uniform  
 297 over the space of initial conditions and cannot be anticipated *a priori*. The return map to  $\partial B$  gives a flexible  
 298 construction that can be applied over any length of the transient. This framework is also amenable to  
 299 analysis that captures global dynamics via phase plane analysis, and can be used in stochastic settings for  
 300 the VI pair [29]. In identifying potentially attracting dynamics, we use projections of the return maps in the  
 301  $\dot{Z}_k - \dot{Z}_{k+1}$  and  $\psi_k - \psi_{k+1}$  phase planes, relative to the corresponding diagonals (see Section 3.1). The maps  
 302 in (2.7)-(2.8) do not lend themselves to these goals, as these are not (necessarily) return maps.

303 For the remainder of the paper, we track the first return maps for impact velocity and impact phase  
 304  $(\dot{Z}_k, \psi_k)$  on  $\partial B$ , using the subscripts  $k, k+1, \dots$  to indicate sequential impacts on  $\partial B$ , composed of the  
 305 building blocks in (3.1). Figure 3 shows how the choice of these building blocks divides the state space  
 306 for  $(\dot{Z}_k, \psi_k)$  by viewing this pair as the initial condition, which then yields one of these two return maps.  
 307 Figure 3(a) shows how the  $(\dot{Z}_k, \psi_k)$  plane is divided by tracking the return maps. Figure 3(b) illustrates a  
 308 further division of the state space, necessary for applying straightforward polynomial approximations of the  
 309 return maps, as discussed in the context of the full algorithm described in Section 4. Note that the building  
 310 blocks (3.1) are analogous to short words in the symbolic representations used for piecewise linear maps in  
 311 [52], which form the basis for invariant cones and trapping regions.

312 **Remark 3.2.** *For the algorithm developed in this paper, we restrict our attention to the range of  $0 \leq \psi_k \leq \pi$ ,*  
 313 *discussed further in the context of Fig. 7 below. As can be shown for the model (2.1)-(2.3) and the parameters*  
 314 *considered in this paper, impacts with  $\psi_k > \pi$  correspond to those where the ball and capsule are moving in*  
 315 *the same direction, yielding smaller impact velocities and thus transient behavior in both  $\psi_k$  and  $\dot{Z}_k$  [46].*  
 316 *This point is discussed in Section 3.1 below, in the context of projections of the 2D maps for  $\dot{Z}_k, \psi_k$  into*  
 317 *their corresponding phase planes. Likewise, for the parameter regimes considered in this paper, focusing on*  
 318 *a range of  $d$  with energetically favorable 1:1-type sequences of alternating impacts, the impact velocities in*  
 319 *the range  $\dot{Z} > 1.25$  are transient. Figure 23 in Appendix A.1 illustrates the additional regions with transient*  
 320 *BTTB behavior, which can appear for  $\dot{Z} > 1.25$ . While the approach proposed here can handle these values*  
 321 *by including additional transient regions, for simplicity of exposition, we restrict our attention to  $0 \leq \psi_k \leq \pi$*   
 322 *and  $0 < \dot{Z} \leq 1.25$ .*



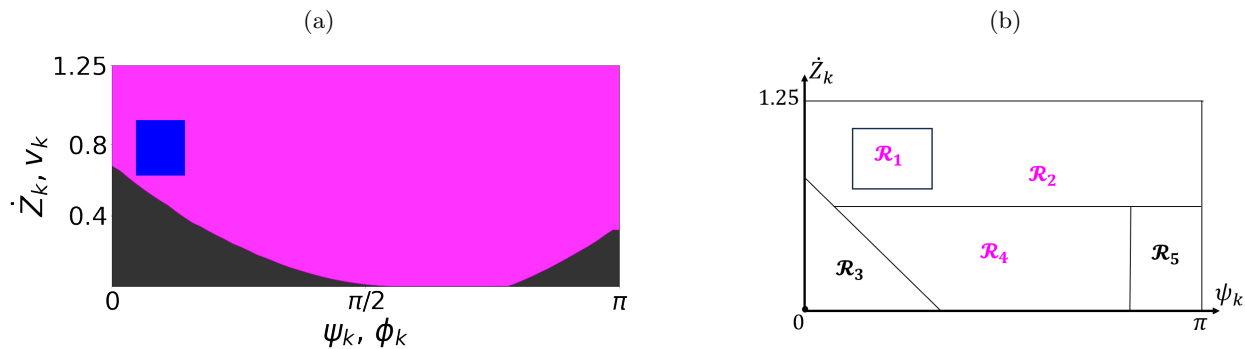


Fig. 3: (a): Using the building blocks in (3.1), the state space  $\dot{Z}_k - \psi_k$  can be partitioned based on two types of first return maps:  $P_{BB}$  (black regions) and  $P_{BTB}$  (magenta region). The blue square indicates the location of  $\mathcal{R}_1$ , a region within the  $P_{BTB}$  region that has special properties as studied in detail in Section 4. (b): Further partition of the state space into five regions: Regions  $\mathcal{R}_1, \mathcal{R}_2, \mathcal{R}_4$  divide the state space for the BTB motion, and Regions  $\mathcal{R}_3, \mathcal{R}_5$  divide the state space for the BB motion. The partition in panel (b) shows an approximation to the exact solution in panel (a), so the dividing boundaries between regions do not match exactly those based on the exact map. Parameter  $d = 0.26$ .

323 Figure 4 illustrates the reduction of our representation within the dynamics, focused on the impact  
 324 velocity  $\dot{Z}_j$  and phase  $\phi_j$  on  $\partial B$  (green stars), in contrast to Fig. 1(b), which shows the exact behavior  
 325 solution at and between the impact time. The first return maps in (3.1) are implicit in form and thus awkward  
 326 to use directly in a global stability analysis. Then, as a first step towards a more explicit approximation, we  
 327 visualize the return maps in (3.1).

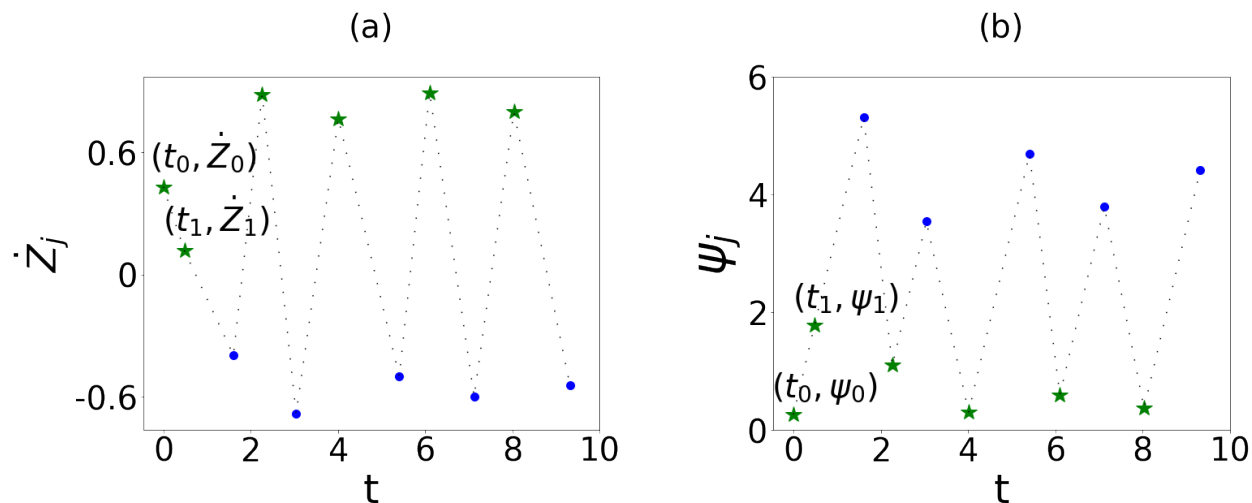


Fig. 4: The values  $(\dot{Z}_j, \psi_j)$  at impacts (both  $\partial B$  (green stars) and  $\partial T$  (blue circles)), starting with initial conditions  $\dot{Z}_0 = 0.43$  and  $\psi_0 = 0.26$  with  $d = 0.35$ . Note that the location of the impact determines the sign of the relative velocity:  $\dot{Z}_j > 0$  for the impact on  $\partial B$ , and  $\dot{Z}_j < 0$  for  $\partial T$ , and the dotted lines trace the order in which the impacts happen. In this paper, we focus on the return map for  $\partial B$ , denoted  $(\dot{Z}_k, \psi_k)$ .

328 **3.1. Visualization.** Given that the return maps  $P_{BTB}, P_{BB}$  are in terms of the 2D vector  $(\dot{Z}_k, \psi_k)$  we  
 329 show two separate surfaces for  $\dot{Z}_{k+1}$  and  $\psi_{k+1}$  generated by them. To build these up, we first show the maps  
 330 projected in the phase planes  $\dot{Z}_k - \dot{Z}_{k+1}$  and  $\psi_k - \psi_{k+1}$ , for a fixed value of  $0 < \psi_k < \pi$ , and sweeping  
 331 through  $\dot{Z}_k \in (0, 1.25)$ . In Fig. 5(a), the resulting first return values  $(\dot{Z}_{k+1}, \psi_{k+1})$  are sorted according to

332 BTB and BB motion, as indicated by different colors. In Fig. 5(b), in this projection, these two types of  
 333 behavior can interweave for a single value of  $\psi_k$ , as different values of  $\dot{Z}_k$  yield a variety of  $\psi_{k+1}$  that appear  
 334 in both the  $P_{\text{BTB}}$  and  $P_{\text{BB}}$  return maps.

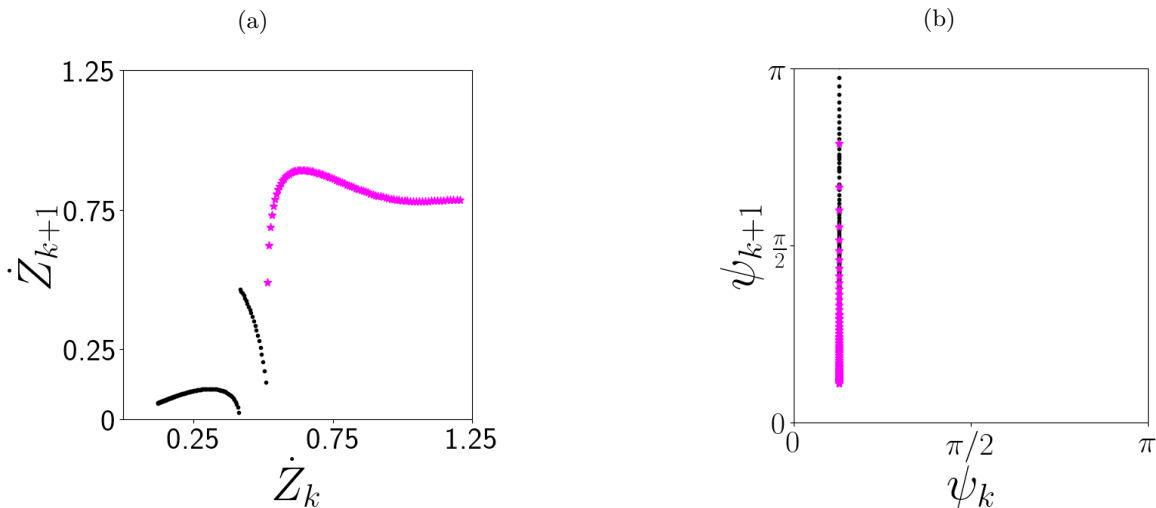


Fig. 5: Illustration of  $\dot{Z}_{k+1}$  and  $\psi_{k+1}$ , the first return maps on  $\partial B$  using (3.1) for fixed  $\psi_k = 0.4$  and sweeping through initial values  $\dot{Z}_k \in (0, 1.25)$  with  $d = 0.35$ . The magenta points correspond to the first returns via BTB type, and the black points represent the first returns of BB type.

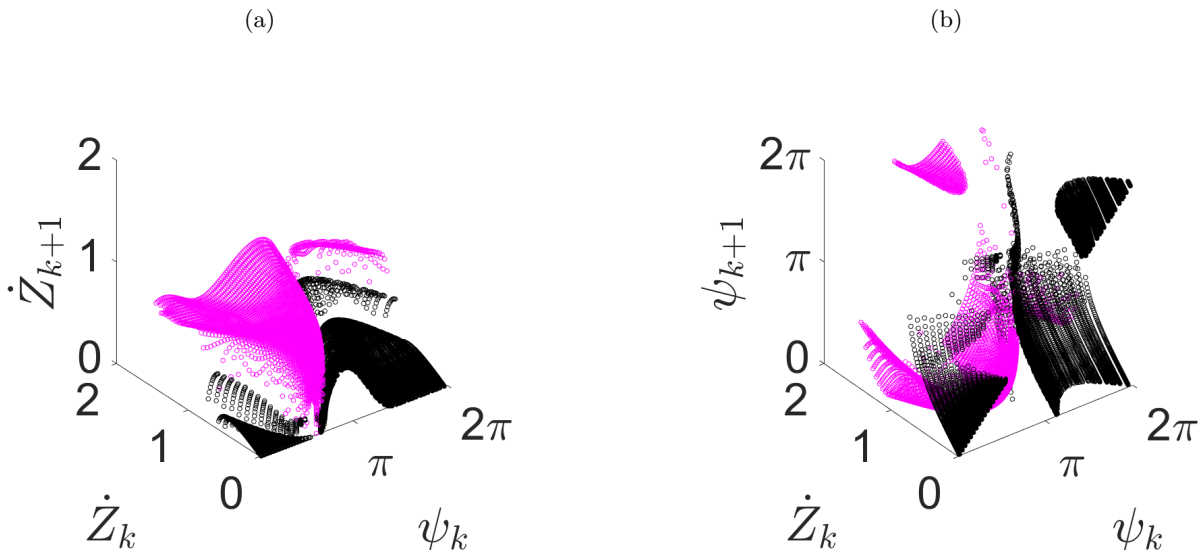


Fig. 6: Illustration of the 3D surfaces generated using the first return maps  $P_{\text{BTB}}$  (magenta) and  $P_{\text{BB}}$  (black) in (3.1), with  $d = 0.35$ . Each initial condition pair  $(\dot{Z}_k, \psi_k)$  has output  $(\dot{Z}_{k+1}, \psi_{k+1})$ , graphed on the vertical axes in panels (a) and (b), respectively.

335 Repeating the application of the first return map (3.1) over the range of initial phase values  $\psi_k$  yields the  
 336 surface visualized in Fig. 6, over a range of initial values in the horizontal  $\dot{Z}_k - \psi_k$  plane. For  $P_{\text{BB}}$ , shown by  
 337 the black points, in general small values of  $\dot{Z}_k$  (approximately  $\dot{Z}_k < 0.55$ ) map into small values of  $\dot{Z}_{k+1}$ , while

338  $\psi_{k+1}$  tends towards values either near 0 or above  $2\pi$ . In the case of  $P_{\text{BTB}}$ , shown by magenta points, larger  $\dot{Z}_k$   
339 map into larger values of  $\dot{Z}_{k+1}$ , with the corresponding  $\psi_{k+1}$  spread out between 0 and  $\pi$ . The visualization  
340 of the return maps  $P_{\text{BB}}$  and  $P_{\text{BTB}}$  indicates a few features that are important in approximating these surfaces  
341 with polynomial maps. Not only are the surfaces disconnected, but the surfaces have dramatically different  
342 gradients corresponding to different regions in the  $Z_k - \psi_k$  state space, which leads to the partitioning as  
343 shown in Fig. 3(b). These regions are identified as part of the algorithm for approximating the surfaces, as  
344 discussed in detail in Section 4.

345 Comparison of the return maps with the diagonals in the  $\dot{Z}_k - \dot{Z}_{k+1}$  and  $\psi_k - \psi_{k+1}$  phase planes is  
346 achieved via projections of the return map surfaces on the phase planes, as shown in Appendix A.2, Fig. 24.  
347 This projection is valuable as we identify potential regions for attracting and transient behaviors, following  
348 from comparisons of the map surfaces with the diagonals in the phase planes. For example, as discussed  
349 in Section 4, intersections of the projections and the diagonals in both phase planes suggest a potential  
350 attracting region for  $(\dot{Z}_k, \psi_k)$  near  $\mathcal{R}_1$  in Fig. 3(b), depending on the slopes of the maps for these values. In  
351 contrast, the projection shown in Fig. 7, particularly for the  $(\psi_k, \psi_{k+1})$  phase plane, illustrates the highly  
352 transient nature of any step with a value  $\pi < \psi < 2\pi$ , as discussed above in Remark 3.2. Section 4 includes  
353 this information in the application of the algorithm, combining visualizations of Figs. 6, 7, 24, and 23 to  
354 give further insight into behavior on subdivisions of the return map surfaces together with approximating  
355 these surfaces with polynomials.

356 **4. Composition of the Approximate Map.** We provide an algorithm for deriving a set of explicit  
357 piecewise polynomial maps  $f_n$  and  $g_n$  for each region  $\mathcal{R}_n$  in the state space  $\dot{Z}_k - \psi_k$ , approximating the  
358 surfaces  $\dot{Z}_{k+1}$  and  $\psi_{k+1}$  as shown in Fig. 6. The approximate return maps are given in terms of the variables  
359  $(v_k, \phi_k)$  that denote the approximate relative impact velocity on  $\partial B$  and the corresponding impact phase,  
360 respectively, at the  $k^{\text{th}}$  return to  $\partial B$ . We define the composite approximate map  $\mathcal{M}$  that combines the  
361 continuous maps  $f_n, g_n$  for the regions  $\mathcal{R}_n$  in Fig. 3(b), taking the form

$$362 \quad (4.1) \quad (v_{k+1}, \phi_{k+1}) = \mathcal{M}(v_k, \phi_k) \equiv (f_n(v_k, \phi_k), g_n(v_k, \phi_k)), \text{ where } (v_k, \phi_k) \in \mathcal{R}_n.$$

363 Given the complex nature of the surfaces for  $\dot{Z}_{k+1}$  and  $\psi_{k+1}$ , the algorithm for constructing the maps  
364  $(f_n, g_n)$ , leads to refining the regions shown in Fig. 3(a), resulting in the regions  $\mathcal{R}_n$  for  $n = 1, 2, 3, 4, 5$  in  
365 Fig. 3(b).

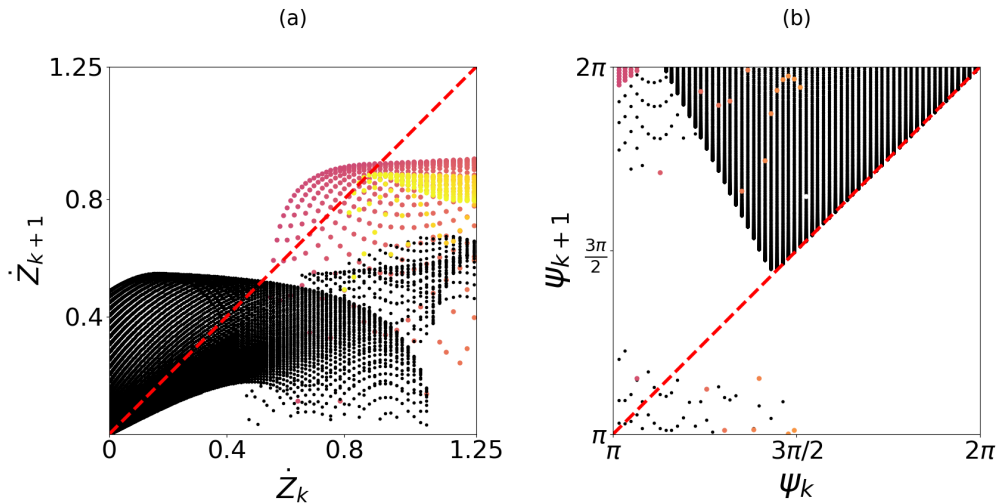


Fig. 7: The 2D projection of Fig. 6 on the phase plane  $\dot{Z}_k - \dot{Z}_{k+1}$  and  $\psi_k - \psi_{k+1}$  for initial condition  $\psi_k \in [\pi, 2\pi]$  and  $d = 0.35$ . Since there is no common point of intersection on both diagonals in (a) and (b), we conclude that the states generated from the initial states  $(\dot{Z}_k, \psi_k)$  with  $\psi_k \in [\pi, 2\pi]$ , always leave this range. The colored points represent the BTB motion, and the black points represent the BB motion.

366 As a first illustration that  $\mathcal{M}$  in (4.1) (derived below, with specifics given in Appendix A.8) captures the

367 critical features of (2.7)-(2.8) in the parameter range of interest, we use it to obtain the bifurcation diagram  
 368 analogous to Fig. 2. Figure 8 shows the results for  $v_k, \phi_k$  vs.  $d$ , generated using  $\mathcal{M}$  via the continuation-type  
 369 method described in Remark 3.1. Comparing with the corresponding bifurcation diagram for the exact map  
 370 in Fig. 2, we see that the results from  $\mathcal{M}$  capture a number of features of the original system, including  $d$   
 371 values for the period-doubling bifurcations, the attracting values of  $v_k$  and  $\phi_k$  for the different branches, and  
 372 the approximate range of values of  $v_k$  and  $\phi_k$  for the chaotic behavior obtained for smaller  $d$  in the range  
 373 shown in Figs. 2, 8.

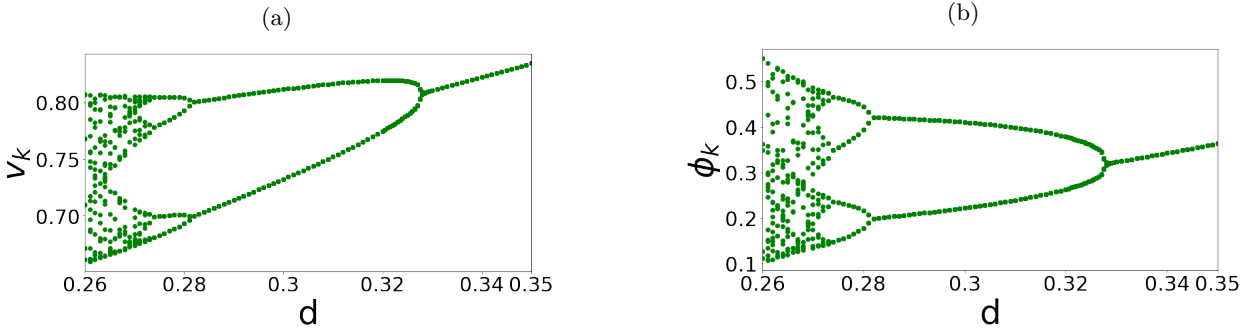


Fig. 8: Bifurcation diagrams generated using the composite approximate map  $\mathcal{M}$ , defined in (4.1) and Appendix A.8, with coefficients given in Supplementary Section II. The bifurcation structure obtained using  $\mathcal{M}$  reproduces remarkably well that obtained for the exact map (2.7)-(2.8) presented in Fig. 2.

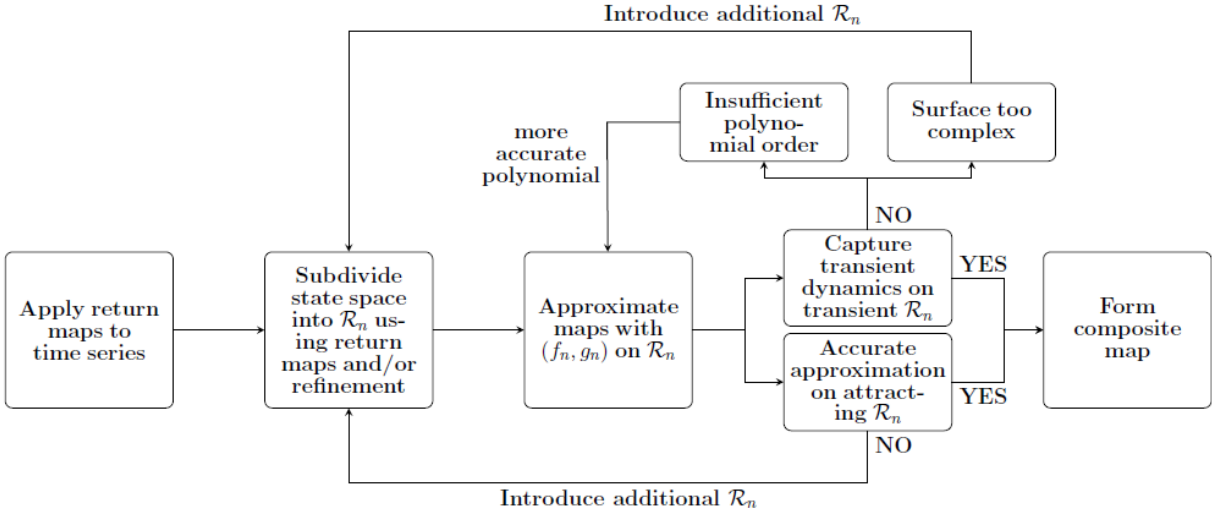


Fig. 9: Illustration of the general algorithm for constructing the composite map.

374 **4.1. General Algorithm: Construction of the composite map  $\mathcal{M}$ .** Illustrated in Fig. 9, the  
 375 general algorithm consists of three main activities: identifying an initial partition of the state space based  
 376 on the return map building blocks, iterating on approximations of the return maps on these regions, and  
 377 including updates of the regions as necessary to improve the approximation.

378  
 379 **Initialize: steps 0)-ii):** Partition state space for the definition of the composite map.  
 380 0). Choose a state as the basis for return behavior.

- 381 i). Generate surfaces  $(\dot{Z}_{k+1}, \psi_{k+1})$  corresponding to the first return maps for this state;  
 382 ii). Partition regions in the state space based on different types of first returns. Label these regions as  $\mathcal{R}_{n,1}$ ,  
 383 denoting Region  $n$  defined on iteration 1.

384  
 385 **Iterate on steps iii)-vi)** until appropriate fit for surfaces corresponding to first return map for all re-  
 386 gions  $\mathcal{R}_{n,m}$ , Region  $n$  on  $m^{\text{th}}$  iteration.

- 387 iii). Identify potential regions of attraction or transient behavior.  
 388 iv). Choose an appropriate order of polynomial fit for each, via testing different orders of polynomials and,  
 389 depending on the resolution needed, to identify  $f_n$  and  $g_n$  for each  $\mathcal{R}_{n,m}$   
 390 v). If the fit of the polynomial is unsatisfactory, adjust the size of the regions and/or locate new regions for  
 391 additional partitions.  
 392 vi). Optimal reduction: for regions that yield immediate transitions to other regions, replace with appro-  
 393 priate resetting conditions.

394  
 395 **Finalize**

- 396 vii). Once the polynomial approximations are defined for maps for all regions, finalize definitions of regions,  
 397 labeled as  $\mathcal{R}_n$ , dropping the  $.m$  label, together with their corresponding maps  $(f_n, g_n)$ . This final step in-  
 398 cludes a definition of the range for each map, as discussed further in the demonstration in Section 5.

399  
 400 Steps iii)-vi) depend on the analysis of several different features of the first return map surfaces found  
 401 in ii), both dynamics and geometric characteristics and combinations of these. We illustrate these next in  
 402 the concrete context of (2.1)-(2.3) and the corresponding non-dimensional form (2.6).

403 **Remark 4.1.** *As demonstrated below, in certain regions  $\mathcal{R}_n$  where the shape of the map clearly indicates*  
 404 *transient dynamics, we look for a simple approximation that takes the form of a single variable polynomial*  
 405 *for each of the variables of interest, e.g.,  $v_{k+1} = f_n(v_k)$  and  $\phi_{k+1} = g_n(\phi_k)$ . We refer to these as separable*  
 406 *maps since we approximate the 2D map for  $(v_k, \phi_k)$  with two 1D maps that each depend on a single variable.*  
 407 *Such an approximation supports a cleaner visualization in the phase plane by simplifying the details of the*  
 408 *transient behavior while approximating it as dictated by the shape of the exact map.*

409 **4.2. Algorithm implementation: a composite map for the VI pair model.** We apply the gen-  
 410 eral algorithm outlined above - Initialize, Iterate, and Finalize - to identify appropriate partitions of the  
 411 state space and the approximations for the return maps on these regions for the non-dimensionalized VI pair  
 412 model as in (2.7). Here, we present this application step-by-step, with the specific details of the composite  
 413 map  $\mathcal{M}$  given in Appendix A.8.

414  
 415  
 416 **Initialize** the partition of the state space.

- 417 0). Choose  $Z \in \partial B$  as the state for the basis of the first return maps.  
 418 i). Generate surfaces  $\dot{Z}_{k+1}$  and  $\psi_{k+1}$  for BTB and BB behavior as first return maps (2.8) over the range of  
 419 possible initial conditions in the state space  $(\dot{Z}_k, \psi_k)$  (see, e.g., Fig. 3(a)).  
 420 ii). Partition the state space into regions  $\mathcal{R}_{n,1}$  according to these building blocks: BTB and BB:  $\mathcal{R}_{1,1}$  cor-  
 421 responds to BTB,  $\mathcal{R}_{3,1}$  corresponds to BB behavior for smaller  $\psi_k$ , and  $\mathcal{R}_{5,1}$  corresponds to BB behavior  
 422 with larger  $\psi_k$ .

423  
 424 **Iteration 1:** steps iii)-vi)

- 425 iii). Identify regions of potential attraction and transients as follows.  
 426 •  $\mathcal{R}_{1,1}$ : entire region of BTB behavior, including both transient regions and potential attracting  
 427 dynamics near the diagonals in the  $\dot{Z}_k - \dot{Z}_{k+1}$  and  $\psi_k - \psi_{k+1}$  planes.  
 428 •  $\mathcal{R}_{3,1}$ : The surfaces for BB behavior with sharp gradients in the map near the diagonals. Thus,  
 429 transient BB behavior is expected.  
 430 •  $\mathcal{R}_{5,1}$ : The surfaces for BB behavior are away from the diagonal in the  $\psi_k - \psi_{k+1}$  plane, thus  
 431 transient BB behavior is expected.  
 432 iv). Polynomial approximation of surfaces for  $\dot{Z}_{k+1}$  and  $\psi_{k+1}$  in  $\mathcal{R}_{1,1}$ ,  $\mathcal{R}_{3,1}$ , and  $\mathcal{R}_{5,1}$  (see Fig. 6):  
 433 •  $\mathcal{R}_{1,1}$ , BTB behavior: There is a combination of subregions where the surfaces for  $\dot{Z}_{k+1}$  and

434  
435  
436  
437  
438  
439  
440  
441  
442  
443  
444  
445  
446  
447  
448  
449  
450  
451  
452  
453  
454  
455  
456  
457  
458  
459  
460  
461  
462

$\psi_{k+1}$  have more gradual variation, contrasted with others with sharp gradients. Thus, an accurate polynomial fit is challenging, which also limits an accurate approximation of potentially attracting dynamics near the diagonals in the  $\dot{Z}_k - \dot{Z}_{k+1}$  and  $\psi_k - \psi_{k+1}$  phase planes. This motivates a further partitioning the BTB region, as described in step v).

- $\mathcal{R}_{3.1}$ , BB behavior: As can be observed in Fig. 6, there are two disjoint surfaces for  $\dot{Z}_{k+1}$ . One is a curved surface with sharp gradients for which we use fifth/fourth order polynomials in  $v_k/\phi_k$  for the approximate map  $(f_3, g_3)$  (see Appendix A.6). There is a second segment, nearly vertical in  $\dot{Z}_{k+1}$ , discussed in (vi) below.
  - $\mathcal{R}_{5.1}$ : As the surfaces for  $\dot{Z}_{k+1}$  and  $\psi_{k+1}$  in  $\mathcal{R}_{5.1}$  are away from the diagonal, we use a “separable” approximation, as discussed in Remark 4.1. See Appendix A.7 for a discussion of the resulting approximate map  $(f_5, g_5)$ .
- v). Update regions in terms of additional partitions for  $\mathcal{R}_{1.1}$ . The different features of the  $\dot{Z}_{k+1}$  and  $\psi_{k+1}$  surfaces in  $\mathcal{R}_{1.1}$  motivates sub-dividing into two regions:
- $\mathcal{R}_{1.2}$ : identify potentially attracting states, e.g. states for which the repeated images of the return map  $P_{BTB}$  are near the diagonals in the  $\dot{Z}_k - \dot{Z}_{k+1}$  and  $\psi_k - \psi_{k+1}$  phase planes. This choice of  $\mathcal{R}_{1.2}$  limits to cases where the slopes of the surfaces near the diagonals are primarily small, e.g., less than unity for some values of  $d$ .
  - $\mathcal{R}_{2.2}$ : the remaining states that produce clearly transient BTB behavior. This region includes sections of the  $P_{BTB}$  map located away from the phase plane diagonals and sections near the diagonals with sharp gradients.
- vi). From physical considerations, some maps are replaced with resetting functions and/or approximate maps in nearby regions.
- $\pi < \phi < 2\pi$ : The transient behavior for this range of  $\phi_k$  is discussed in Remark 3.2 above. Then, we employ the reset:  $\phi_{k+1} = 1.2$  and  $v_{k+1} = v_k$  if  $\phi_k > \pi$  or  $\phi_k < 0$  (see Appendix A.8).
  - The nearly vertical surface in  $\mathcal{R}_{3.1}$  mentioned above represents strongly transient behavior, consisting of transitions to BTB behavior or other states in  $\mathcal{R}_3$ . This transient behavior is captured by using equations (A.2) throughout  $\mathcal{R}_{3.1}$ , without approximating the vertical surface. Likewise, there is a small vertical section of the surface  $\psi_{k+1}$  in  $\mathcal{R}_{5.1}$ , also discussed in Appendix A.7.

463 **Iteration 2:** steps iii)-vi)

464 Iteration 2 is focused on the newly defined  $\mathcal{R}_{1.2}$  and  $\mathcal{R}_{2.2}$ .

465 iii). Considering attracting and transient BTB behavior:

- To identify  $\mathcal{R}_{1.2}$  as described in Iteration 1 step v), we introduce a filter  $\mathcal{R}_{1.2}(d)$  for a given  $d$  that selects states  $(\dot{Z}_k, \psi_k)$  near the diagonals  $(\dot{Z}_k, \psi_k)$  in the  $\dot{Z}_k - \dot{Z}_{k+1}$  and  $\psi_k - \psi_{k+1}$  phase planes with images  $(\dot{Z}_{k+1}, \psi_{k+1})$  from  $P_{BTB}$  near the same diagonals. We then take the union of these regions to obtain a region valid for the full range of  $d$  of interest. Then,  $\mathcal{R}_{1.2}$  is given by

$$\begin{aligned}
 \mathcal{R}_{1.2}(d) &= \left\{ (\dot{Z}_k, \psi_k) : \frac{1}{\delta} < \left| \frac{\psi_{k+1}}{\psi_k} \right| < \delta \text{ and } \frac{1}{\delta} < \left| \frac{\dot{Z}_{k+1}}{\dot{Z}_k} \right| < \delta \right\}, \\
 \mathcal{R}_{1.2} &= \cup_{d \in [0.26, 0.35]} \mathcal{R}_{1.2}(d).
 \end{aligned}
 \tag{4.2}$$

474 Of course, the size of  $\mathcal{R}_{1.2}$  depends on the choice of  $\delta$ , which characterizes proximity to the  
475 diagonals, as discussed further in Appendix A.3. Figure 10 shows an example of the definition  
476 of  $\mathcal{R}_{1.2}$ .

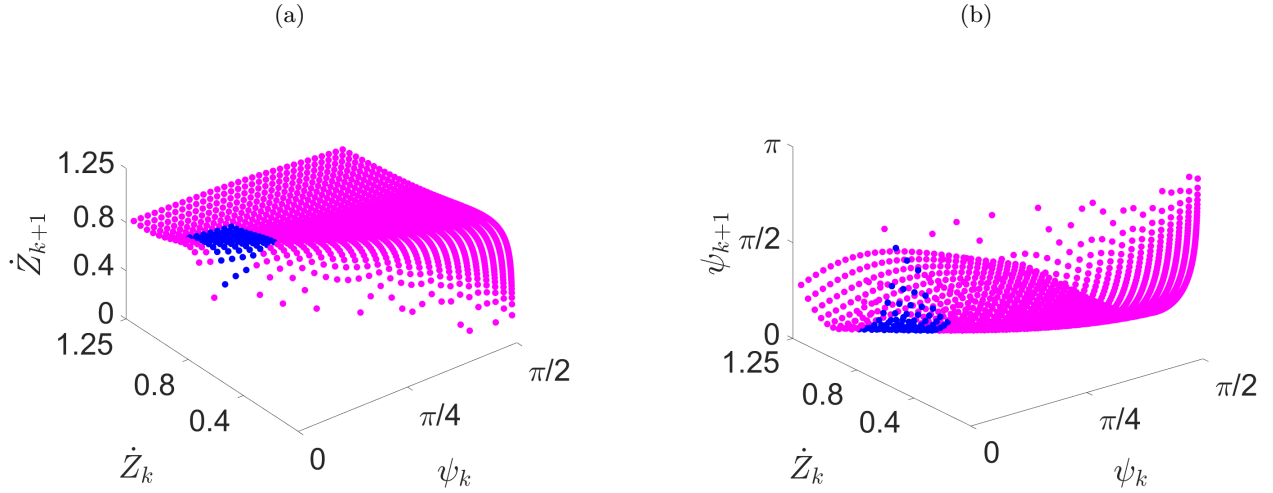


Fig. 10: The surface corresponding to  $P_{\text{BTB}}$  (magenta and blue combined), where  $\mathcal{R}_{1.2}$  (blue region), is obtained by using the filter (4.2) ( $\delta = 1.2$ ) to identify return maps located near diagonals in both the  $\dot{Z}_{k+1} - \dot{Z}_k$  and  $\psi_{k+1} - \psi_k$  phase planes.

477  
478  
479  
480

- $\mathcal{R}_{2.2}$  is defined as the remainder of the BTB region, with transient behavior.
- iv). Polynomial approximation of surfaces  $\dot{Z}_{k+1}$  and  $\psi_{k+1}$ .
- $\mathcal{R}_{1.2}$ : To capture subtle changes in the attracting behavior near the diagonals, the surfaces for  $\dot{Z}_{k+1}$  and  $\psi_{k+1}$  are approximated with polynomials of degree 3 in  $v_k$  and degree 2 in  $\phi_k$

481  
482  
483  
484  
485

$$\begin{aligned}
 v_{k+1}(v_k, \phi_k) &= f_1(v_k, \phi_k) \\
 (4.3) \quad &= b_0 + b_1 \phi_k + b_2 v_k + b_3 \phi_k^2 + b_4 \phi_k v_k + b_5 v_k^2 + b_6 \phi_k^2 v_k + b_7 \phi_k v_k^2 + b_8 v_k^3,
 \end{aligned}$$

$$\begin{aligned}
 \phi_{k+1}(v_k, \phi_k) &= g_1(v_k, \phi_k) \\
 (4.4) \quad &= a_0 + a_1 \phi_k + a_2 v_k + a_3 \phi_k^2 + a_4 \phi_k v_k + a_5 v_k^2 + a_6 \phi_k^2 v_k + a_7 \phi_k v_k^2 + a_8 v_k^3.
 \end{aligned}$$

486

- $\mathcal{R}_{2.2}$ : We use a “separable” approximation (see Remark 4.1) that takes the form

487  
488

$$\begin{aligned}
 v_{k+1}(v_k) &= f_2(v_k) = b_{20} v_k^5 + b_{21} v_k^4 + b_{22} v_k^3 + b_{23} v_k^2 + b_{24} v_k + b_{25}, \\
 (4.5) \quad \phi_{k+1}(\phi_k) &= g_2(\phi_k) = a_{20} \phi_k^5 + a_{21} \phi_k^4 + a_{22} \phi_k^3 + a_{23} \phi_k^2 + a_{24} \phi_k + a_{25}.
 \end{aligned}$$

490  
491  
492  
493

Figure 11(a)-(c) shows (green) curves representative of the transient behavior for this region, following from the shape of the surfaces for  $\dot{Z}_{k+1}$  and  $\psi_{k+1}$  shown in panel c) for  $\mathcal{R}_{2.2}$ . The orange curves, showing the separable map in (4.5), approximates this green curve. See further discussion in Appendix A.4.

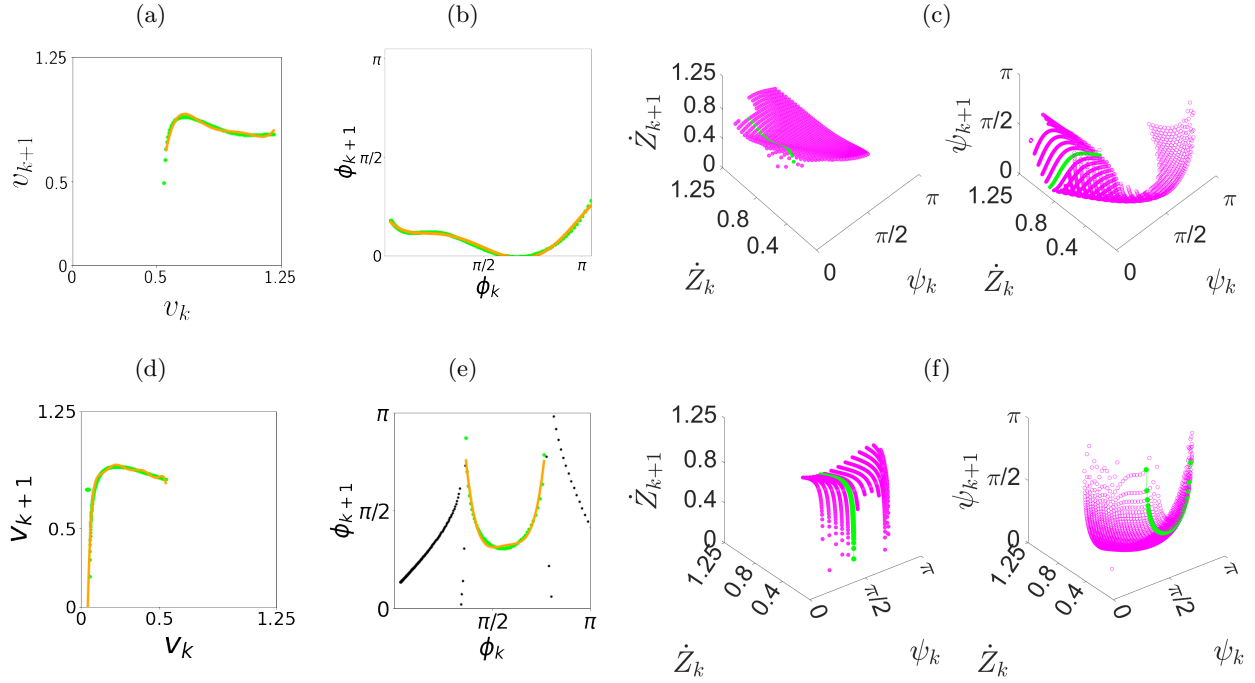


Fig. 11: Illustration of the  $P_{\text{BTB}}$  surface (magenta surfaces in panels c,f) and its corresponding separable approximation (green and orange curves) for  $\mathcal{R}_2$  (panels a, b, c) and  $\mathcal{R}_4$  (panels d, e, f), with  $d = 0.35$ . Generated using the exact map (3.1), the green curves are chosen to represent the variation of the surface for fixed  $\psi_k$  or  $\dot{Z}_k$ . Specifically, for (c):  $\psi_k = 0.35$  (left) and  $\dot{Z}_k = 0.85$  (right); for (f):  $\psi_k = 1.35$  (left)  $\dot{Z}_k = 0.12$  (right). Panels (a)-(b) and (d)-(e) compare the green curves and the orange curves for the approximate separable map (4.5) in the phase planes. See Appendices A.4 and A.5 for details.

- 494 v). Update regions/additional partitions for  $\mathcal{R}_{2.2}$ : As seen from the curve shown in Fig. 11, which  
 495 forms the basis of the separable map, the map is not defined on smaller values of  $\dot{Z}_k$  in  $\mathcal{R}_{2.2}$ . This  
 496 suggests a further partition of  $\mathcal{R}_{2.2}$  into  $\mathcal{R}_{2.3}$  and  $\mathcal{R}_{4.3}$ , to capture all values of  $\dot{Z}_{k+1}$ , as described  
 497 in Appendices A.4 and A.5.  
 498 vi). No further updates on this optional step.  
 499

500 **Remark 4.2.** Here, we note that the individual curves  $v_{k+1} = f_2(v_k)$  and  $\phi_{k+1} = g_2(\phi_k)$  shown for  $\mathcal{R}_{2.2}$   
 501 each overlap with the intervals for  $v_k$  and  $\phi_k$  in  $\mathcal{R}_{1.2}$ . At first glance, this may seem to cause indeterminacy  
 502 in the application of the map. However, since  $\mathcal{R}_2$  surrounds  $\mathcal{R}_1$ , it is possible that one of  $v_k$  or  $\phi_k$  in  $\mathcal{R}_{2.2}$   
 503 can take a value that also appears in the range for  $\mathcal{R}_{1.2}$ . However, for  $(v_k, \phi_k)$  in  $\mathcal{R}_{1.2}$ , i.e. both  $v_k$  and  $\phi_k$   
 504 in the intervals corresponding to  $\mathcal{R}_{1.2}$ , then  $(v_{k+1}, \phi_{k+1}) = (f_1, g_1)$  as in (4.3)-(4.4), and not the separable  
 505 approximation  $(f_2(v_k), g_2(\phi_k))$ .

506 **Iteration 3:** steps iii)-vi)

507 This iteration focuses on  $\mathcal{R}_{2.3}$  and  $\mathcal{R}_{4.3}$ .

508

509 iii). Considering transient dynamics for  $\mathcal{R}_{4.3}$ : For values of small  $v_k$  not covered by the map (4.5) in  
 510  $\mathcal{R}_{2.2}$ , we consider surfaces as shown in Fig. 11(f).

511 iv). Polynomial approximation of  $\mathcal{R}_{4.3}$ : Similar to the separable maps defined for  $\mathcal{R}_{2.2}$ , we use separable  
 512 single variable approximations  $(f_4, g_4)$  for the transient dynamics, given in equation (A.1) and shown  
 513 in Fig. 11(d) and 11(e).

514 v). No additional partitions are needed.

515 vi). No further updates needed.

516 **Finalize**



517  
518  
519

vii) We finalize definitions of the regions  $\mathcal{R}_n$ ,  $n = 1, 2, \dots, 5$  dropping the  $.m$  label. The corresponding maps  $(f_n, g_n)$  that define the composite map  $\mathcal{M}$  are given in the detailed algorithm in Appendix A.8.

520  
521  
522  
523  
524  
525  
526

**5. Validation of the Composite Map.** In this section, the composite map  $\mathcal{M}$  is validated using three distinct types of solutions, showing that it can reproduce the dynamics of different types of solutions. The first type of solution is the fixed point of  $\mathcal{M}$ , which we call Case FP, corresponding to the 1:1/ $\mathcal{T}$  solution of the full system (2.1)-(2.3). The second type is the period doubled case, i.e., the period-2 orbit of  $\mathcal{M}$ , called Case PD, corresponding to the 1:1/ $2\mathcal{T}$  behavior in the full system. Lastly, the chaotic dynamics of  $\mathcal{M}$ , called Case CD, corresponds to the chaotic 1:1/ $C$  behavior in the full system. These different dynamics can be observed from the bifurcation diagrams in Figs. 2, 8 for  $d = 0.35$ ,  $d = 0.30$ , and  $d = 0.26$ , respectively.

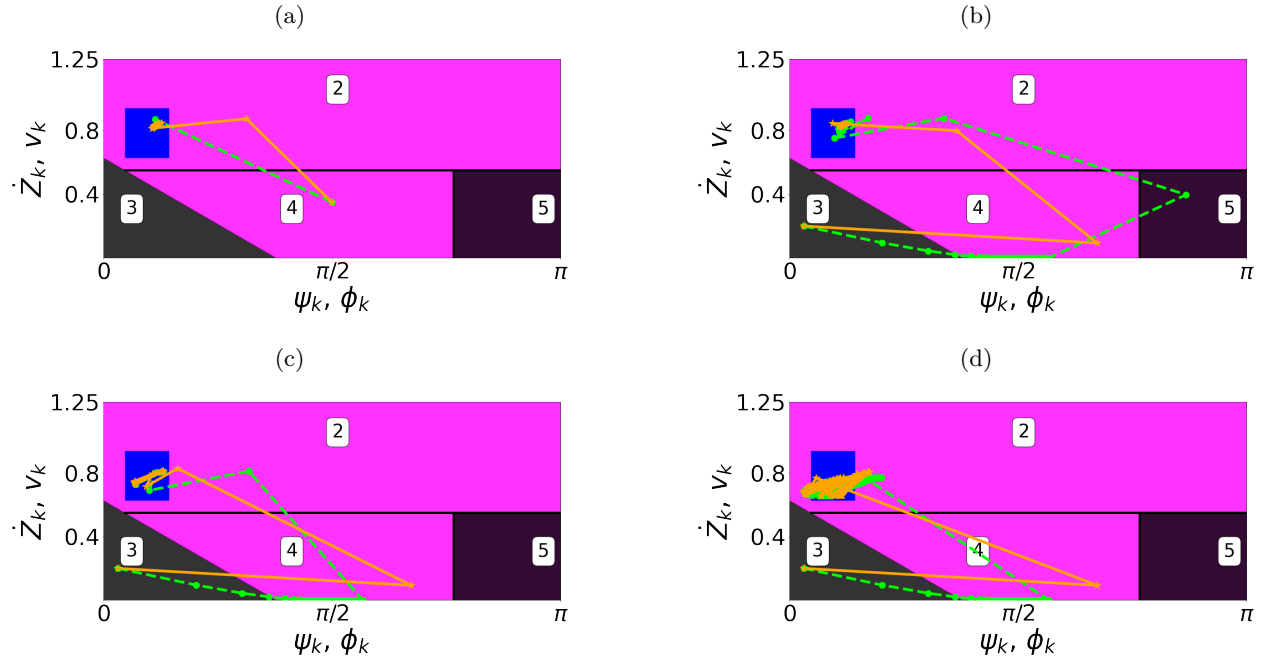


Fig. 12: Comparison of trajectories in state space from the exact map (3.1) (orange) and the composite map  $\mathcal{M}$  (4.1) (green), superimposed on regions  $\mathcal{R}_n$  used in the definition of  $\mathcal{M}$  as specified in Appendix A.8. (a) and (b) correspond to Case FP, also shown in cobweb phase portraits in Fig. 13(a),(b); (c) corresponds to Case PD, also shown in Fig. 13(c),(d); (d) corresponds to Case CD, also shown in Fig. 13(e),(f). Parameter and initial conditions: (a)  $d = 0.35$ ,  $\phi_0 = \pi/2$ ,  $v_0 = 0.35$ ; (b)  $d = 0.35$ ,  $\phi_0 = 0.1$ ,  $v_0 = 0.2$ ; (c)  $d = 0.30$ ,  $\phi_0 = 0.1$ ,  $v_0 = 0.2$ ; (d)  $d = 0.26$ ,  $\phi_0 = 0.1$ ,  $v_0 = 0.2$ . Here, we show representative results for initial conditions in the transient regions  $\mathcal{R}_3$  and  $\mathcal{R}_4$ .

527  
528  
529  
530  
531  
532  
533  
534  
535  
536  
537  
538

Figure 12 shows the implementation of the composite map  $\mathcal{M}$  (dashed green line), with corresponding pseudocode given in Appendix A.8. Initial condition pairs  $(v_k, \phi_k)$  are selected from transient regions  $\mathcal{R}_3$  and  $\mathcal{R}_4$  to demonstrate that  $\mathcal{M}$  can reliably predict the long-term system behavior, reaching an attracting region after traveling through other transient regions  $\mathcal{R}_n$ . Similar results were obtained for other randomly selected initial pairs (not shown here). Trajectories for  $\mathcal{M}$  are plotted together with the trajectories generated with the exact map (3.1) (solid orange line). Panels (a) and (b) correspond to Case FP. Panels (c) and (d) correspond to Case PD and Case CD, respectively. In all cases, both  $\mathcal{M}$  and the exact map (3.1) trajectories follow each other to reach the same attracting dynamics. Of course, the transient dynamics are not reproduced exactly, e.g., given the separable approximations used in  $\mathcal{M}$  to facilitate visualization of the maps.

Complementary to the validation of  $\mathcal{M}$  in Fig. 12, Fig. 13 demonstrates the attracting behavior in the projected  $v_k - v_{k+1}$  and  $\phi_k - \phi_{k+1}$  phase planes with initial conditions for small  $v_k$  and  $\phi_k$  ( $v_0 = 0.2$ ,  $\phi_0 = 0.1$ ). Repeated application of the composite map is demonstrated via cobweb phase portraits, indicating the steps

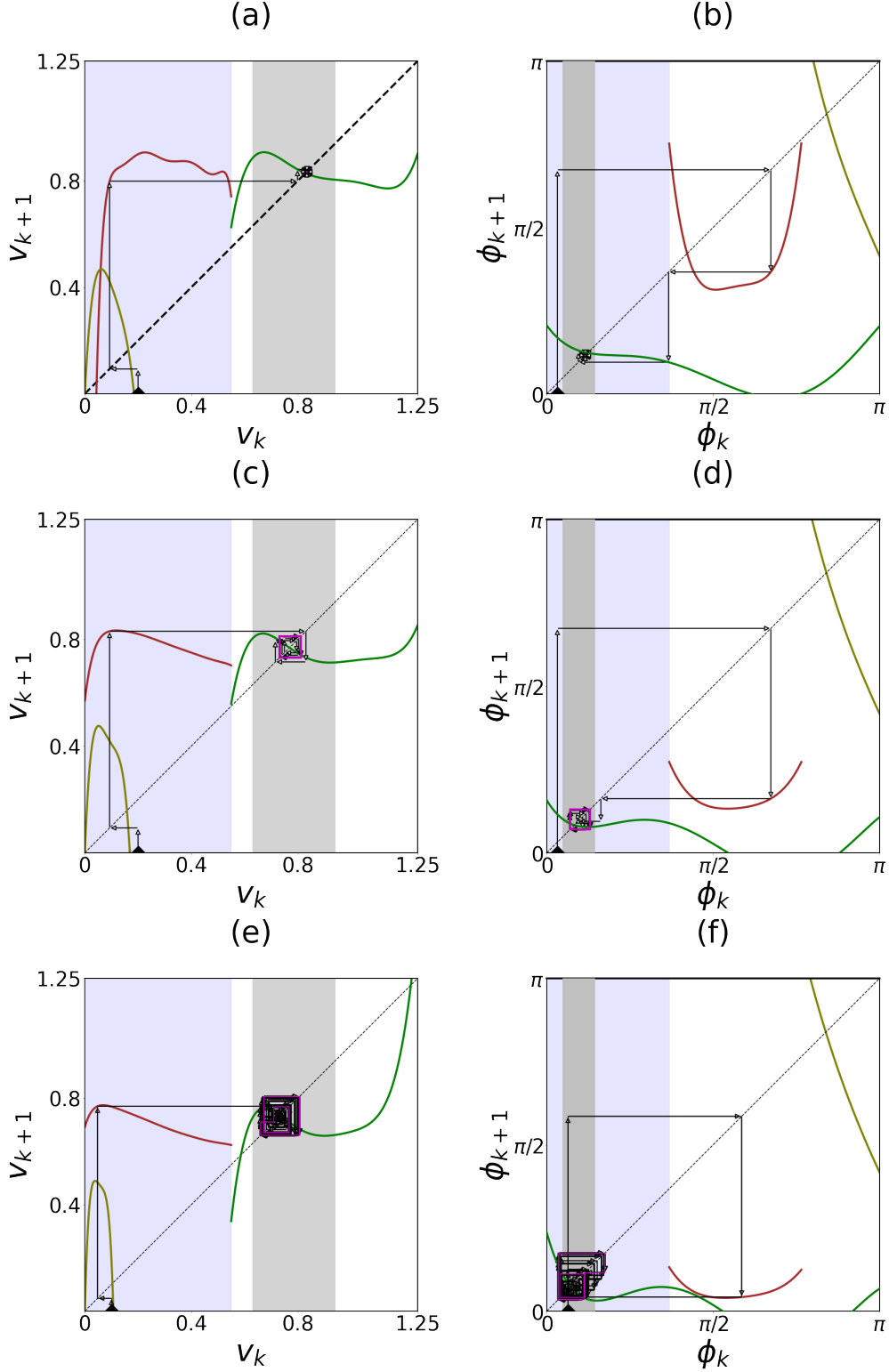


Fig. 13: Application of  $\mathcal{M}$  (4.1) projected on the  $v_k$  and  $\phi_k$  phase planes, with step navigation for  $(f_n, g_n)$  discussed in the text. Curves show (separable) maps for Regions  $\mathcal{R}_2$  (green),  $\mathcal{R}_4$  (red), and  $\mathcal{R}_5$  (olive). Shaded regions are for approximate 2D maps for  $\mathcal{R}_1$  (gray) and  $\mathcal{R}_3$  (light blue), which can not be drawn in these projections. Black dashed lines show the respective diagonals. Parameters: Case FP (a),(b):  $d = 0.35, v_0 = 0.2, \phi_0 = 0.1$ ; Case PD (c),(d):  $d = 0.30, v_0 = 0.2, \phi_0 = 0.1$ ; Case CD (e),(f):  $d = 0.26, v_0 = 0.1, \phi_0 = 0.2$ .

539 toward the attracting behavior. The dynamic behavior is shown for the three types of solutions listed  
540 above. In both Case FP and PD, the trajectories limit to values within  $\mathcal{R}_1$  while in Case CD, the long-term  
541 trajectory takes values in  $\mathcal{R}_1$  and  $\mathcal{R}_2$ . All of these are consistent with the bifurcation structure shown in  
542 Fig. 8.

543 For the projection of the maps  $(f_n, g_n)$  into the  $v_k - v_{k+1}$  and  $\phi_k - \phi_{k+1}$  phase planes shown in Fig. 13, it  
544 is possible to visualize the curves for the maps in  $\mathcal{R}_2$ ,  $\mathcal{R}_4$ , and  $\mathcal{R}_5$ , as we use separable (1D) approximations  
545 in those regions. In  $\mathcal{R}_1$  and  $\mathcal{R}_3$  we can not show a single curve in this projection, given the 2D polynomial  
546 map used in (4.3)-(4.4) and (A.2). Instead, shaded regions show the range of  $v_k$  and  $\phi_k$  in  $\mathcal{R}_1$  (gray) and  
547  $\mathcal{R}_3$  (purple). Then, the cobweb steps in these regions follow the (surface) maps (4.3)-(4.4) and (A.2) for  
548  $\mathcal{R}_1$  and  $\mathcal{R}_3$ , respectively, for  $(v_k, \phi_k)$  in these regions, even though specific curves are not shown. Given the  
549 width of these shaded regions, it is possible to give a maximum and minimum for  $v_{k+1}$  and  $\phi_{k+1}$ , which also  
550 motivates the auxiliary map defined and applied in Section 6 for  $\mathcal{R}_1$ .

551 We provide some navigation in order to trace the cobweb behavior for  $\mathcal{M}$  as shown in Fig. 13. Since the  
552 panels show projections of the higher dimensional maps  $(f_j, g_j)$  in the phase planes, there is an overlap in  
553 these projections, and thus, it is not necessarily obvious how to trace the dynamics. For each cobweb step,  
554  $v_{k+1}, \phi_{k+1}$  takes a value according to the map for the region that is common for both  $(v_k, \phi_k)$ . In all cases  
555 shown, the initial condition  $(v_k, \phi_k)$  for  $k = 0$  takes small values in  $\mathcal{R}_3$ . We observe that  $\mathcal{R}_3$ ,  $\mathcal{R}_4$ , and  $\mathcal{R}_5$   
556 overlap in the  $v_k - v_{k+1}$  phase plane for these smaller values of  $v_k$ , while in the  $\phi_k - \phi_{k+1}$  phase plane the  
557 curve for  $\mathcal{R}_2$  and region  $\mathcal{R}_3$  overlap for smaller  $\phi_k$ . Since  $\mathcal{R}_3$  is the only region in common for  $v_k$  and  $\phi_k$   
558 for these small values, we conclude that  $(v_k, \phi_k) \in \mathcal{R}_3$ , and the first step follows  $(f_3, g_3)$  in (A.2), as shown  
559 in Fig. 13. In the next step,  $v_k$  remains small while  $\phi_k$  increases (before reaching the attracting dynamics).  
560 Again  $\mathcal{R}_3$ ,  $\mathcal{R}_4$ , and  $\mathcal{R}_5$  overlap in the  $v_k - v_{k+1}$  phase plane for these smaller values of  $v_k$ , while in the  
561  $\phi_k - \phi_{k+1}$  plane,  $\phi_k$  takes a value corresponding to the range for  $\mathcal{R}_4$  only, so that  $v_{k+1}, \phi_{k+1}$  follow the map  
562  $(f_4, g_4)$  for  $\mathcal{R}_4$ . Note that the curve for  $\mathcal{R}_5$  is not applied for  $v_k$ , even though  $v_k$  takes values in its range,  
563 since  $\phi_k$  has not reached  $\mathcal{R}_5$ . Eventually  $v_k$  has increased to a range with an overlap between  $\mathcal{R}_2$  and  $\mathcal{R}_1$ ,  
564 while  $\phi_k$  decreases back to the region with overlap between  $\mathcal{R}_2$ ,  $\mathcal{R}_1$  and  $\mathcal{R}_3$ . Then, the cobweb steps are  
565 governed by  $(f_2, g_2)$  for  $(v_k, \phi_k) \in \mathcal{R}_2$ , and by  $(f_1, g_1)$  in (4.3)-(4.4) for  $(v_k, \phi_k) \in \mathcal{R}_1$ , as already discussed  
566 in Remark 4.2 about the overlap between the green curves and the grey shaded  $\mathcal{R}_1$  region. From there,  
567 the dynamics are dictated by the attracting dynamics of  $\mathcal{R}_1$  for panels (a),(b) and (c),(d) corresponding to  
568 Cases FP and PD, respectively. In panels (e) and (f), the attracting chaotic dynamics for Case CD alternate  
569 between  $\mathcal{R}_1$  and  $\mathcal{R}_2$ .

570 **6. Global Stability and the Auxiliary Maps.** The trajectories above indicate visually that Regions  
571  $\mathcal{R}_1$  and  $\mathcal{R}_2$  contain an absorbing domain that attracts all non-trivial trajectories in  $\mathcal{R}_1$  and  $\mathcal{R}_2$  for the  
572 considered range of parameter  $d$ . In Fig. 13, iterations of the closed-form composite map visualize the  
573 system's long-term behavior, with explicit curves shown only for regions  $\mathcal{R}_2$ ,  $\mathcal{R}_4$ , and  $\mathcal{R}_5$  when projected  
574 onto the  $\dot{Z}_{k+1} - \dot{Z}_k$  and  $\phi_{k+1} - \phi_k$  planes. In contrast, for  $\mathcal{R}_1$  and  $\mathcal{R}_3$  the maps cannot be visualized under  
575 this projection, suggesting that an alternate approach is needed to capture global attraction using these  
576 cobweb phase portraits. The difference between the regions follows from the separable form of the maps  
577 in  $\mathcal{R}_2$ ,  $\mathcal{R}_4$ , and  $\mathcal{R}_5$ , in contrast to the 2D maps of  $\mathcal{R}_1$  and  $\mathcal{R}_3$ . This observation inspires the design of an  
578 auxiliary map, in which we dissect each 2D map into a pair of 1D maps based on the lower and upper bounds  
579 of the 2D map domain. This definition can then take advantage of the separable form and lead to bounds  
580 on the composite map's absorbing domain.

581 **6.1. Constructing the Auxiliary Maps.** The auxiliary map is constructed using the bounds on the  
582 approximate maps  $(f_n, g_n)$  for each Region  $\mathcal{R}_n$ , where  $(f_n, g_n)$  depends on both variables  $v_k$  and  $\phi_k$ . In our  
583 case, these regions are  $\mathcal{R}_1$  and  $\mathcal{R}_3$ . We define the auxiliary maps in terms of the maxima and minima of  
584  $(f_n, g_n)$ , yielding the form:  $\xi_{\max}(v_k) : v_k \rightarrow v_{k+1}$  and  $\eta_{\max}(\phi_k) : \phi_k \rightarrow \phi_{k+1}$ , and similarly for the minima.  
585 This decouples the two 2-D equations into two separable 1-D equations for each  $\mathcal{R}_n$ . The advantage of this  
586 formulation is its ability to track the dynamics of velocity  $v_k$  and the phase  $\phi_k$  separately, thus facilitating  
587 a 1D cobweb phase portrait for each. At the same time, it captures the worst-case scenario and provides  
588 conservative bounds on the maximum and minimum range of  $(f_n, g_n)$  at each iterate. Furthermore, we show  
589 that a repeated application of this auxiliary definition hones in on the attracting solutions or regions of the  
590 full map. While here we give the construction in terms of general  $n$ , we emphasize that below it is applied  
591 for  $\mathcal{R}_1$  only, as we focus on the attracting behavior.

592 The construction of the auxiliary map begins with the bounds for  $v_k$  and  $\phi_k$  for a given  $\mathcal{R}_n$ :  $v_k \in$   
593  $[v_{\min}, v_{\max}]$  and  $\phi_k \in [\phi_{\min}, \phi_{\max}]$ . Then two curves  $\xi_{\max}(v_k)$  and  $\xi_{\min}(v_k)$  are determined for  $v_{k+1}$  in terms  
594 of the max and min of  $f_n$  over the range of possible  $\phi_k$  values, and the auxiliary map  $\xi_n^{(N)}$  alternates between  
595 these two curves:

$$596 \quad (6.1) \quad \xi_n^{(N)} = \begin{cases} v_{k+1} = \xi_{\max}^{(N)}(v_k), & \text{where } \xi_{\max}^{(N)} := \max_{\phi_k \in \mathcal{A}_n^{(N)}} \{f_n(v_k, \phi_k)\}, \\ v_{k+1} = \xi_{\min}^{(N)}(v_k), & \text{where } \xi_{\min}^{(N)} := \min_{\phi_k \in \mathcal{A}_n^{(N)}} \{f_n(v_k, \phi_k)\}. \end{cases}$$

597 The superscript  $N$  gives the index of updates of the auxiliary map after the first and subsequent appli-  
598 cations, particularly valuable when the auxiliary map is contracting, as demonstrated below for the specific  
599 cases considered in Section 6.2. To track the (possible) contraction of the region for each update, we define  
600  $\mathcal{A}_n^{(N)}$  in (6.4)-(6.5) below. There  $\mathcal{A}_n^{(N)} = \mathcal{R}_n$  for all  $N$  if the region does not contract, while  $\mathcal{A}_n^{(1)} = \mathcal{R}_n$  and  
601  $\mathcal{A}_n^{(N)} \subseteq \mathcal{R}_n$  for  $N > 1$  for a contracting region, updated as the auxiliary map is updated. For the system  
602 studied here, it is only for  $n = 1$  that  $\mathcal{A}_n^{(N)}$  contracts.

603 Likewise, the auxiliary map  $\eta_n^{(N)}$  is given in terms of two maps  $\eta_{\max}$ ,  $\eta_{\min}$  that bound  $\phi_{k+1}$  for  $v_k \in$   
604  $[v_{\min}, v_{\max}]$ :

$$605 \quad (6.2) \quad \eta_n^{(N)} = \begin{cases} \phi_{k+1} = \eta_{\max}^{(N)}(\phi_k), & \text{where } \eta_{\max}^{(N)} := \max_{v_k \in \mathcal{A}_n^{(N)}} \{g_n(v_k, \phi_k)\}, \\ \phi_{k+1} = \eta_{\min}^{(N)}(\phi_k), & \text{where } \eta_{\min}^{(N)} := \min_{v_k \in \mathcal{A}_n^{(N)}} \{g_n(v_k, \phi_k)\}. \end{cases}$$

606 We then write the full auxiliary map, replacing  $\mathcal{M}$  (4.1) with  $\mathcal{M}_{\mathcal{A}}^{(N)}$ , which is composed of a combination  
607 of maps  $(f_n, g_n)$  and  $(\xi_n^{(N)}, \eta_n^{(N)})$ , with  $v_k, \phi_k$  corresponding to impact velocities on  $\partial B$  as in (4.1). For our  
608 system it is only  $\mathcal{A}_1^{(N)}$  that contracts as  $N$  increases, so we define the full auxiliary map as

$$609 \quad (v_{k+1}, \phi_{k+1}) = \mathcal{M}_{\mathcal{A}}^{(N)}(v_k, \phi_k),$$

$$610 \quad (6.3) \quad \mathcal{M}_{\mathcal{A}}^{(N)}(v_k, \phi_k) \equiv \begin{cases} (\xi_1^{(N)}(v_k), \eta_1^{(N)}(\phi_k)) & \text{for } (v_k, \phi_k) \in \mathcal{A}_1^{(N)}, \\ (\xi_3^{(N)}(v_k), \eta_3^{(N)}(\phi_k)) & \text{for } (v_k, \phi_k) \in \mathcal{R}_3, \\ (f_n(v_k, \phi_k), g_n(v_k, \phi_k)) & \text{for } (v_k, \phi_k) \in \mathcal{R}_n, n = 2, 4, 5. \end{cases}$$

611 We define region  $\mathcal{A}_1^{(N)} \subseteq \mathcal{R}_1$  to allow a change in its size over the  $N$  updates of the auxiliary construction,

$$612 \quad (6.4) \quad \mathcal{A}_1^{(N)} = \begin{cases} \mathcal{R}_1 & \text{for } N = 1, \\ \mathcal{B}_1^{(N)} & \text{otherwise.} \end{cases}$$

$$613 \quad (6.5) \quad \mathcal{B}_1^{(N)} \equiv [\min v_{k+\ell}, \max v_{k+\ell}] \times [\min \phi_{k+\ell}, \max \phi_{k+\ell}]$$

$$614 \quad \text{for } (v_{k+\ell}, \phi_{k+\ell}) = \left( \mathcal{M}_{\mathcal{A}}^{(N-1)} \right)^\ell (v_k, \phi_k), \ell \gg 1.$$

615 Stated in words, (6.4)-(6.5) simply indicate that for the  $N^{\text{th}}$  ( $N > 1$ ) update of  $(\xi_1^{(N)}(v_k), \eta_1^{(N)}(\phi_k))$ , the  
616 region  $\mathcal{A}_1^{(N)}$  is updated to the limiting range of  $(v_k, \phi_k)$  obtained from a large number of iterations of  
617  $(\xi_1^{(N-1)}(v_k), \eta_1^{(N-1)}(\phi_k))$ .

618 **Remark 6.1.** *As demonstrated below, updating the region  $\mathcal{A}_1^{(N)}$  and  $\mathcal{M}_{\mathcal{A}}^{(N)}$  is valuable for the region(s)*  
619 *in which the dynamics are contracting since these updates allow a relaxation of the worst-case scenario*  
620 *imposed by the maxima and minima used in the definitions. Thus, we apply this update accordingly below to*  
621 *approximate the size of the attracting region.*

622 **6.2. Application of the auxiliary map  $\mathcal{M}_{\mathcal{A}}^{(N)}$ .** In Section 5, the application of  $\mathcal{M}$  via cobweb phase  
623 portraits indicates that the absorbing dynamics are concentrated in  $\mathcal{R}_1$  for the larger values of  $d$  considered  
624 in this study. Specifically, in Fig. 13, we see attracting solutions contained in  $\mathcal{R}_1$  in Case FP and PD, while  
625 the trajectories oscillate between  $\mathcal{R}_1$  and  $\mathcal{R}_2$  in Case CD.

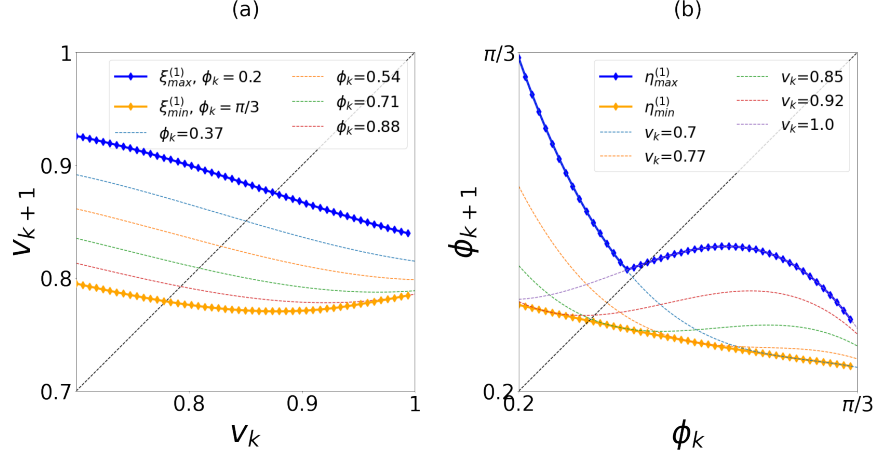


Fig. 14: Visualization of the auxiliary maps  $\xi_1^{(1)}$  and  $\eta_1^{(1)}$  ((6.1) and (6.2)) for  $\mathcal{R}_1^+$ , as the lower (orange diamonds) and upper (blue diamonds) bounds of the maps for  $v_{k+1} = f_1(v_k, \phi_k)$  and  $\phi_{k+1} = g_1(v_k, \phi_k)$ . In (a), the family of curves corresponds to the map  $f_1$  for fixed  $\phi_k$  values. Likewise, in (b) for  $g_1$  with fixed  $v_k$  values.

626 While we could construct an auxiliary map in the setting where the dynamics revisit regions with  
627 transient dynamics (e.g.,  $\mathcal{R}_2$ ), this would require a different construction to be useful in demonstrating  
628 global stability. Instead, the absorbing dynamics suggest a more efficient approach. From Fig. 13, the  
629 absorbing domain covers values in  $\mathcal{R}_1$  for Cases FP and PD, and in a region just outside of  $\mathcal{R}_1$  for Case CD.  
630 This suggests constructing the auxiliary map on a slightly expanded region  $\mathcal{R}_1^+ \supseteq \mathcal{R}_1$ , noting that this does  
631 not reduce the accuracy of the approximation as it uses the more accurate  $2D$  approximation over a larger  
632 region, reducing the region over which the separable approximation ( $f_2, g_2$ ) is used. Then we can expand  
633 the size of Region  $\mathcal{R}_1$  to  $\mathcal{R}_1^+$  sufficiently so that the long-term dynamics remain in  $\mathcal{R}_1^+$  and  $\mathcal{R}_1^+ \supseteq \mathcal{R}_1$ , and  
634 here we consider the auxiliary map for  $\mathcal{R}_1^+$  only.

635 The following are the ranges of the initial region  $\mathcal{A}_1^{(1)} = \mathcal{R}_1^+$  for the three cases, the fixed point (FP)  
636 case, the period-doubling (PD) case, and the chaotic dynamics (CD) case of the composite map  $\mathcal{M}$ :

637 (6.6) **Case FP:**  $\mathcal{R}_1^+ := \{(v_k, \phi_k) : v_k \in [0.7, 1] \text{ and } \phi_k \in [0.2, \pi/3]\}$   
638 (6.7) **Case PD:**  $\mathcal{R}_1^+ := \{(v_k, \phi_k) : v_k \in [0.65, 1] \text{ and } \phi_k \in [0.13, \pi/3]\}$   
639 (6.8) **Case CD:**  $\mathcal{R}_1^+ := \{(v_k, \phi_k) : v_k \in [0.64, 1] \text{ and } \phi_k \in [0.08, \pi/3]\}$

640 Figure 14 illustrates this construction of  $\xi_1^{(1)}$  and  $\eta_1^{(1)}$  in (6.1) and (6.2) for Case FP, with  $\mathcal{A}_1 = \mathcal{R}_1^+$  and  
641  $N = 1$ . In the phase plane  $(v_k, v_{k+1})$ , the family of curves  $f_1(v_k, \phi_k)$  do not cross each other, so  $\xi_{\max}^{(1)} :=$   
642  $f_1(v_k, \min(\phi_k))$  and  $\xi_{\min}^{(1)} := f_1(v_k, \max(\phi_k))$  for  $\phi_k \in [0.2, \pi/3]$ , thus yielding closed-form expressions for  
643  $\xi_1^{(1)}$  in terms of  $f_1$ . In contrast for  $\phi_k$ , the family of curves for  $g_1(v_k, \phi_k)$  with fixed  $v_k$  cross each other so  
644 that the envelope for  $g_1$  is found computationally from the definition of  $\eta_{\max}^{(1)}$  and  $\eta_{\min}^{(1)}$  in (6.2). Note that  
645 the shape of the auxiliary map  $(\xi_1^{(1)}, \eta_1^{(1)})$  indicates its contracting properties in  $\mathcal{R}_1^+$ , discussed further below.  
646 Auxiliary maps for  $\mathcal{R}_3$  can also be constructed using the method described in Section 6.1. However, since  
647  $\mathcal{R}_3$  is a transient region, we do not pursue its construction here but focus on the use of the auxiliary map in  
648  $\mathcal{R}_1^+$ .

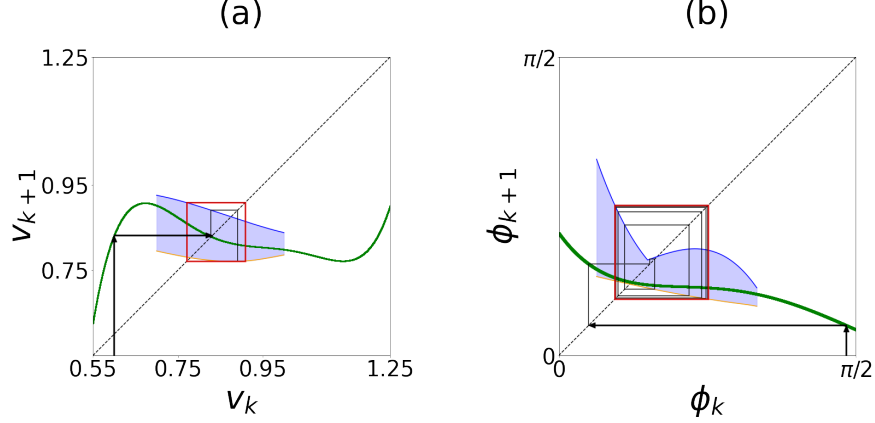


Fig. 15: Application of  $\mathcal{M}_{\mathcal{A}}^{(1)}$  (6.3) for  $d = 0.35$  with initial conditions  $(v_0, \phi_0)$  in  $\mathcal{R}_2$ . The green lines show  $\mathcal{R}_2$  approximate maps (4.5), and the blue and orange curves show  $(\xi_{\max}^{(1)}, \eta_{\max}^{(1)})$  and  $(\xi_{\min}^{(1)}, \eta_{\min}^{(1)})$ , respectively for  $\mathcal{R}_1^+$  (6.1)-(6.2). The areas between these curves are shaded in blue, representing the possible values of  $v_k$  and  $\phi_k$  in  $\mathcal{R}_1^+$ . Analogous to the cobweb phase portraits for  $\mathcal{M}$  above, the map  $(f_2, g_2)$  is used for  $(v_k, \phi_k) \in \mathcal{R}_2$ , and the auxiliary map is used for  $(v_k, \phi_k) \in \mathcal{R}_1^+$ , as discussed in Remark 4.2. The last 40 steps of the cobwebs are shown in red, indicating the attracting orbit within  $\mathcal{R}_1^+$  for  $\mathcal{M}_{\mathcal{A}}^{(1)}$ .

649 We apply the cobweb phase portrait method, combined with the update of the auxiliary map region  
 650  $\mathcal{A}_1^{(N)}$  within the composite auxiliary map  $\mathcal{M}_{\mathcal{A}}^{(N)}$ , to three cases with distinct dynamics: Case FP,  
 651 and Case CD.

652 Figure 15 illustrates the cobweb phase portraits for  $\mathcal{M}_{\mathcal{A}}^{(1)}$ , with initial conditions in  $\mathcal{R}_2$  for simplicity of  
 653 exposition. The cobweb trajectories for  $v_k$  and  $\phi_k$  quickly leave  $\mathcal{R}_2$  after two steps, with  $(v_k, \phi_k)$  reaching  
 654 the attracting region  $\mathcal{R}_1^+$ . Then in both of the  $v_k - v_{k+1}$  and  $\phi_k - \phi_{k+1}$  phase planes, the cobweb iterations  
 655 follow the auxiliary map  $\mathcal{A}_1^+$ . Specifically, this maps  $v_k$  to  $v_{k+1}$  using the upper-bound auxiliary map  $\xi_{\max}^{(1)}$ ,  
 656 followed by  $v_{k+1}$  to  $v_{k+2}$  using the lower-bound auxiliary map  $\xi_{\min}^{(1)}$ , and then continuing with alternating  
 657 upper and lower auxiliary maps. Then, the auxiliary map captures the worst-case scenario of the trajectory  
 658 in  $\mathcal{R}_1^+$ , yielding the maximum range in this region. Likewise, the auxiliary maps for  $\phi_k \in \mathcal{R}_1^+$  are iterated,  
 659 yielding a trajectory that covers the range of  $\phi_k$ . In contrast to the composite map  $\mathcal{M}$ , for which  $v_k, \phi_k$  reach  
 660 fixed points (see Fig. 13),  $\mathcal{M}_{\mathcal{A}}^{(N)}$  has an attracting orbit, due to the use of the max and min in (6.1)-(6.2).  
 661 We use the bounds on this limiting behavior, shown in red in Fig. 15, to provide an update to  $\mathcal{A}_1^{(N+1)}$  in  
 662  $\mathcal{M}_{\mathcal{A}}^{(N+1)}$  as in (6.4)-(6.5) for the  $N + 1^{\text{st}}$  step of the computer-assisted characterization of the attracting  
 663 dynamics.

664 Figure 16 illustrates the updates of region  $\mathcal{A}_1^{(N)}$  and  $\mathcal{M}_{\mathcal{A}}^{(N)}$  in the FP case. Each row shows results for a  
 665 different update, specifically  $N = 1, N = 2$ , and  $N = 11$ . The red box highlights the last 10% of the cobweb  
 666 iterations, indicating the limiting dynamics for  $\mathcal{M}_{\mathcal{A}}^{(N)}$ . For  $N = 1$ ,  $\mathcal{A}_1^1 = \mathcal{R}_1^+$  is defined as in (6.6) and is also  
 667 the same as in Fig. 15. The size of the corresponding absorbing domain (indicated by the red box) shrinks  
 668 with  $N$ , and  $\mathcal{A}_1^{(N)}$  for  $N > 1$  is updated accordingly, as in (6.4)-(6.5). For increasing  $N$ , Figs. 16 (c),(d) and  
 669 (e),(f) illustrate the smaller range of  $v_k$  and  $\phi_k$  given by  $\xi_{\max/\min}^{(N)}$  and  $\eta_{\max/\min}^{(N)}$ , mirroring the smaller size  
 670 of  $\mathcal{A}_1^{(N)}$ . Figure 17 then shows how the length and width of the absorbing domain for  $v_k$  and  $\phi_k$  decreases  
 671 with increasing  $N$ . Thus, even though the max/min characteristics of the auxiliary map do not allow the  
 672 limiting behavior of  $\mathcal{M}_{\mathcal{A}}$  to be a fixed point, nevertheless, for Case FP, we see that region  $\mathcal{A}_1^{(N)}$  shrinks to  
 673 a negligible size for large  $N$ .

674 Similar to the cobweb illustration of the updates in the Case FP, Fig. 18 and Fig. 20 illustrate the updates  
 675 of the region  $\mathcal{A}_1^{(N)}$  and  $\mathcal{M}_{\mathcal{A}}^{(N)}$  in Case PD and Case CD, respectively. The setup in Fig. 18 and Fig. 20 is  
 676 the same as in Fig. 16, with each row showing results from updates of  $\mathcal{A}_1^{(N)}$ . In Case PD,  $N = 1, N = 2$ ,  
 677 and  $N = 11$  are shown; while in Case CD,  $N = 1$  and  $N = 6$  are shown. Moreover, in contrast to the

678 Case FP, where the limiting dynamics approaches a point for  $N$  large, for Cases PD and CD, the size of the  
679 absorbing domain saturates to its limiting size at a finite  $N$ . In Case PD, the limiting dynamics converge to  
680 an attracting period-2 orbit (2-cycle) for both  $v_k$  and  $\phi_k$  when  $N$  is large, with much of the size reduction of  
681  $\mathcal{A}_1^{(N)}$  occurring in the first two updates, as shown in Fig. 19. In contrast to case FP, the attracting 2-cycle  
682 has a limiting size dictated by  $|p_v - q_v|$  and  $|p_\phi - q_\phi|$ .

683 Similar to Case PD, Fig. 20 shows that the limiting dynamics of Case CD when  $N$  is large yields  
684 attracting orbits over a larger range of  $v_k$  and  $\phi_k$ . In addition to the larger size of the attracting region,  
685 the limiting behavior of  $\phi_k$  is an orbit with period-4 (4-cycle), while for  $v_k$ , the orbit has period 2 (2-  
686 cycle), as shown in Fig. 20(c),(d). While the difference in the periodic behavior in the auxiliary map for  
687  $v_k$  and  $\phi_k$  may seem like a contradiction at first glance, in fact, there is no reason for  $v_k$  and  $\phi_k$  to have  
688 the same periodicity, since their auxiliary maps have been decoupled through the use of the bounds on the  
689 region  $\mathcal{A}_1^{(N)}$  and the corresponding max/min in (6.1)-(6.2). In this case, the attracting region obtained  
690 from the auxiliary map slightly underestimates that of the exact map (approximately 2% error). Additional  
691 computational exploration (not shown) indicates this error follows from sensitivity of the relatively simple  
692 approximate polynomial maps in this region where the maps are more complex.

693 The pairs of points  $(p_v, q_v)$  and  $(p_\phi, q_\phi)$  shown in Figs. 16 -20 for the largest value of  $N$  indicate the  
694 maximum  $q_\bullet$  and minimum  $p_\bullet$  of the attracting orbits for  $v$  and  $\phi$ . Likewise, these values can be used to  
695 determine the size of the globally absorbing domain, as discussed in the next section.

696 **6.3. Global Dynamics.** The auxiliary map method developed in the previous subsection opens the  
697 door to characterizing the global dynamics of the composite map. The cobweb phase plane dynamics  
698 simulated for the auxiliary map  $\mathcal{M}_A^{(N)}$ , as shown in Figs. 16-20, demonstrate the convergence to stable  
699 period- $m$  orbits, or  $m$ -cycles, in the FP, PD, and CD cases. Since these  $m$ -cycles bound a subset of the  
700 auxiliary map's phase space, their existence and global stability imply the existence of a globally stable  
701 absorbing domain for the trajectories of the composite map  $\mathcal{M}$  (4.1). The bounds on the absorbing domains  
702 are indicated as  $q_v, p_v, q_\phi$ , and  $p_\phi$  in Figs. 16 - 20 for the largest value of  $N$  shown. Computing these values  
703 as the roots of  $m$  iterations of the maps (6.1) and (6.2) for appropriate  $m$ , we obtain their stability and thus  
704 bounds on the absorbing domain for the dynamics.

705 First, to obtain the bounds on  $v_k$  used in the  $N + 1^{\text{st}}$  update, we consider the second iterate map for  
706  $v_{k+2}$ , given by (6.1)

$$707 \quad (6.9) \quad v_{k+2}(v_k) = \xi_{\min}^{(N)}(\xi_{\max}^{(N)}(v_k)).$$

708 The maps  $\xi_{\min/\max}^{(N)}$  can be written explicitly in terms of  $f_1$  evaluated at  $\phi_{\min/\max}$  (6.1), since the family of  
709 curves  $f_1(v_k, \phi_k)$  for fixed  $\phi_k \in [\phi_{\min}, \phi_{\max}]$  do not cross each other, analogous to  $f_1$  shown in Fig. 14(a).  
710 Then we have the closed-form expression for the first and second iterate maps for  $v_k$ , where the second  
711 iterate map for  $v_{k+2}$  is a 9<sup>th</sup>-order polynomial of the form

$$712 \quad (6.10) \quad v_{k+2}(v_k) = f_1(f_1(v_k, \phi_{\max}), \phi_{\min}) \\ 713 \quad = \alpha_0 + \alpha_1 v_k^1 + \alpha_2 v_k^2 + \alpha_3 v_k^3 + \alpha_4 v_k^4 + \alpha_5 v_k^5 + \alpha_6 v_k^6 + \alpha_7 v_k^7 + \alpha_8 v_k^8 + \alpha_9 v_k^9.$$

715 Here  $\alpha_i, i = 1, \dots, 9$  are polynomials that depend on  $d$  and on  $\phi_{\min}$  and  $\phi_{\max}$ , whose coefficients  $b_0, b_1, \dots, b_9$   
716 are listed in Supplementary Section III. The (stable) root  $v_{k+2} = v_k = p_v$  of (6.10) corresponds to the  
717 minimum on the limiting behavior of  $\xi_1^{(N)}$  (6.1), with the maximum  $q_v$  obtained by

$$718 \quad (6.11) \quad v_k = p_v, \quad v_{k+1} = q_v = f_1(v_k, \phi_{\min}) = f_1(p_v, \phi_{\min}) = \xi_{\max}^{(N)}(p_v), \\ 719 \quad \implies v_{k+2} = p_v = f_1(v_{k+1}, \phi_{\max}) = f_1(q_v, \phi_{\max}) = f_1(f_1(p_v, \phi_{\min}), \phi_{\max}) = \xi_{\min}^{(N)}(p_v).$$

720 These values  $p_v$  and  $q_v$ , together with the limiting behavior indicated by the red boxes for sufficiently large  
721  $N$ , are shown in Figs. 16-20 for the FP, PD, and CD cases.

722 Similarly, the limit cycles for  $\phi_k$  are based on the definition of  $\eta_1^{(N)}$  in (6.2). For the FP and PD cases,  
723 we consider

$$724 \quad (6.12) \quad \phi_{k+2}(\phi_k) = \eta_{\min}^{(N)}(\eta_{\max}^{(N)}(\phi_k)).$$

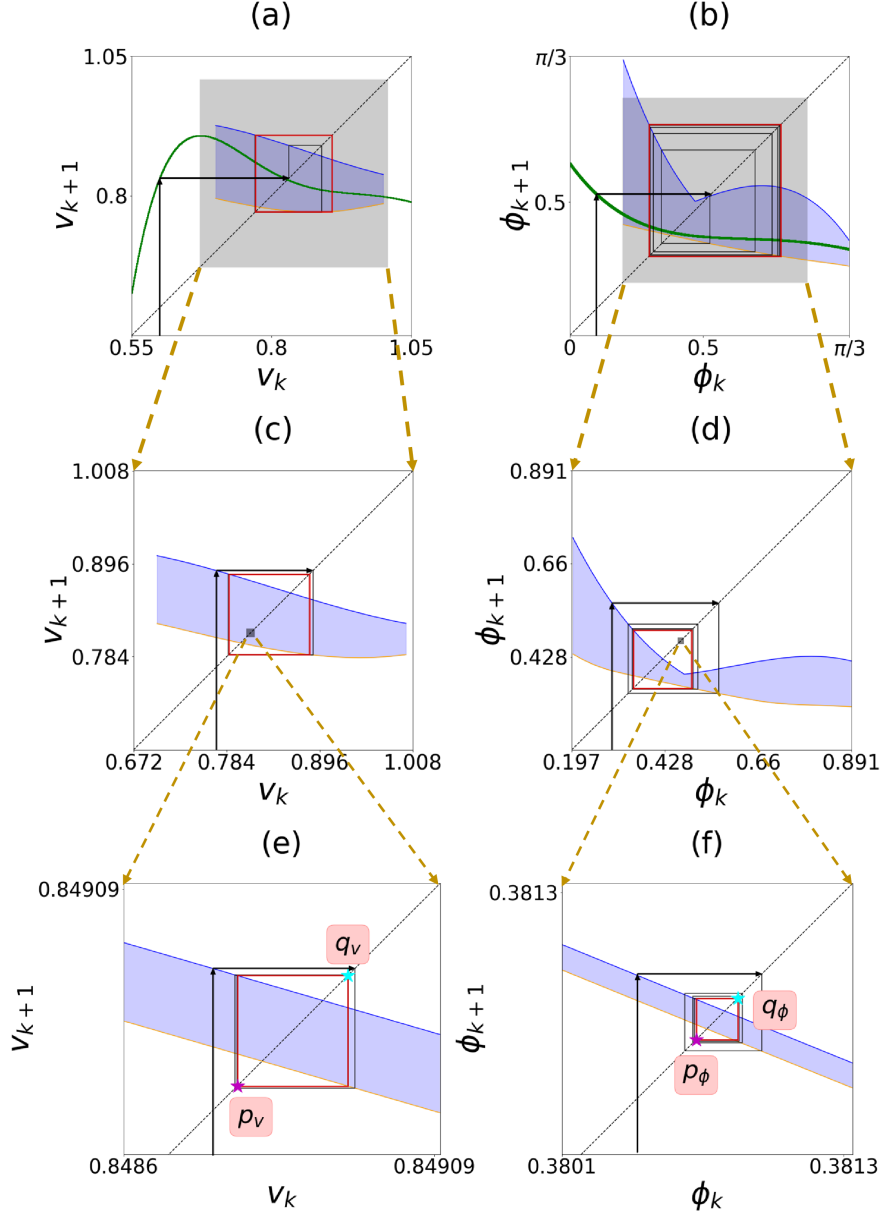


Fig. 16: Illustration of the 1<sup>st</sup>, 2<sup>nd</sup>, and 11<sup>th</sup> update of the auxiliary map  $\mathcal{M}_A^{(N)}$  (6.3) for Case FP ( $d = 0.35$ ). For each  $N$ , 400 steps are taken, and the last 40 steps are highlighted in red. This red orbit also defines  $\mathcal{A}_1^{(N)} \subseteq \mathcal{R}_1^+$  for  $N > 1$ , based on the limiting orbit from the  $(N - 1)^{\text{st}}$  update (see (6.4)-(6.5)). In (a) and (b),  $N = 1$  and  $\mathcal{A}_1^{(1)} = \mathcal{R}_1^+$ , defined in (6.6). As in Fig. 15, the initial condition is in  $\mathcal{R}_2$ , and the first few steps are governed by  $(f_2, g_2)$  (4.5) (green line). In (c),(d)  $N = 2$ , and (e),(f)  $N = 11$ , with the  $N^{\text{th}}$  initial conditions for  $N > 1$  given by the last state from the  $N - 1^{\text{st}}$  update, obtained from the attracting orbit in red. The gray boxes and dashed orange lines between figures indicate the zoom-in region shown in the subsequent row. The stars with  $(p_v, q_v)$  and  $(p_\phi, q_\phi)$  in panels (e) and (f) indicate the min and max of the attracting orbit. For  $N = 2$ ,  $\mathcal{A}_1^{(2)} : v_k \in [0.772, 0.908]$  and  $\phi_k \in [0.297, 0.791]$ , and for  $N = 11$ ,  $\mathcal{A}_1^{(11)} : v_k \in [0.8488, 0.8490]$  and  $\phi_k \in [0.3804, 0.3811]$ .



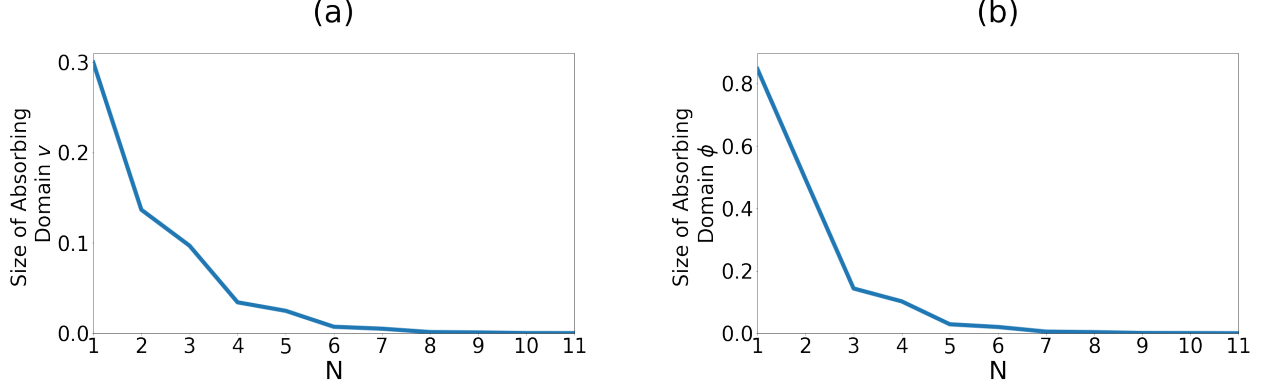


Fig. 17: Illustration of the size of the domain  $\mathcal{A}_N$  for each  $N$ , showing that the absorbing domain size decreases monotonically for Case FP, reaching 0.000185 and 0.0001867 in the  $v_k, \phi_k$  directions, respectively.

725 In contrast to (6.10) for  $v_k$ , the family of curves  $g_1(v_k, \phi_k)$ , in the definition of  $\eta_{\min/\max}$  (6.2) cross each  
 726 other for different fixed  $v_k \in [v_{\max}, v_{\min}]$ , analogous to Fig. 14(b). Then, there is no closed-form expression  
 727 for the first and second iterative maps  $\phi_{k+1}$  and  $\phi_{k+2}$ , and  $\eta_{\max/\min}$  are determined numerically in (6.12).

728 For the FP and PD cases, we calculate  $p_\phi$  and  $q_\phi$ , which give the minimum and maximum of the limiting  
 729 behavior shown by the red boxes in Fig. 16(f) and Fig. 18(f) for sufficiently large  $N$ . They are given by

$$730 \quad (6.13) \quad \phi_k = p_\phi, \quad \phi_{k+1} = q_\phi = \max_{v_k} g_1(v_k, \phi_k) = \max_{v_k} g_1(v_k, p_\phi) = \eta_{\max}^{(N)}(p_\phi),$$

$$731 \quad \implies \phi_{k+2} = p_\phi = \min_{v_k} g_1(v_k, \phi_{k+1}) = \min_{v_k} g_1(v_k, q_\phi) = \min_{v_k} g_1(v_k, \max_{v_k} g_1(v_k, p_\phi)) = \eta_{\min}^{(N)}(\eta_{\max}^{(N)}(p_\phi)).$$

732 Similarly, for the CD case, the minimum and maximum for  $\phi_k$  are generated computationally using the  
 733 fourth iterate map for  $\phi_{k+4}$ .

$$734 \quad (6.14) \quad \phi_{k+4}(\phi_k) = \eta_{\min}^{(N)} \left( \eta_{\max}^{(N)} \left( \eta_{\min}^{(N)} \left( \eta_{\max}^{(N)}(\phi_k) \right) \right) \right).$$

735 For sufficiently large  $N$  as illustrated in Fig. 20(d), there are four fixed points for the period-4 cycle  $\phi_{k+4}$ ,  
 736 calculated as

$$737 \quad \phi_k = p_\phi = \phi_{k+4}, \quad \phi_{k+1} = q_\phi = \eta_{\max}^{(N)}(p_\phi),$$

$$738 \quad (6.15) \quad \phi_{k+2} = \gamma_\phi = \eta_{\min}^{(N)}(q_\phi) = \eta_{\min}^{(N)}(\eta_{\max}^{(N)}(p_\phi)),$$

$$739 \quad \phi_{k+3} = \sigma_\phi = \eta_{\max}^{(N)}(\gamma_\phi) = \eta_{\max}^{(N)}(\eta_{\min}^{(N)}(\eta_{\max}^{(N)}(p_\phi))),$$

$$740 \quad (6.16) \quad \phi_{k+4} = \eta_{\min}^{(N)}(\sigma_\phi) = \eta_{\min}^{(N)}(\eta_{\max}^{(N)}(\eta_{\min}^{(N)}(\eta_{\max}^{(N)}(p_\phi)))).$$

741 Notice that for the CD case, there is a period-2 orbit in  $v_k$  (6.12) and a period-4 orbit in  $\phi_k$ . This unusual  
 742 property follows from the fact that the auxiliary maps for  $v_k$  and  $\phi_k$  are uncoupled, each using the (fixed)  
 743 max and min of the other variable as provided by the previous update.

744 The curves obtained from applying the iterates given in (6.10), (6.12), and (6.14) are shown in Fig. 21.  
 745 Panels (a)-(d) illustrate the stability of the fixed points  $p_v$  and  $p_\phi$  for the period-2 cycles in Cases FP and  
 746 PD. There, the curves show the limiting behavior of the second iterate of  $\mathcal{M}_{\mathcal{A}}^{(N)}$ , given by (6.9) and (6.12).  
 747 They intersect the diagonals in the  $v_{k+2} - v_k$  and  $\phi_{k+2} - \phi_k$  phase planes with a slope less than unity. Then,  
 748 for sufficiently large  $N$  we obtain the stable fixed points  $p_v$  and  $p_\phi$ , likewise implying the stability of the  
 749 fixed points  $q_v$  and  $q_\phi$ , which all together provide the range of the attracting region for  $\mathcal{M}_{\mathcal{A}}^{(N)}$  in Fig. 16  
 750 and Fig. 18. Similarly, for the CD case, in Fig. 21(e),(f) the curves show the limiting behavior of  $\mathcal{M}_{\mathcal{A}}^{(N)}$   
 751 for sufficiently large  $N$ . These curves, obtained from (6.9) for  $v_k$  and the fourth iterate map for  $\phi_k$  (6.14),  
 752 again intersect the diagonals in the phase planes with a slope less than unity, indicating the stability of  $p_v$ ,

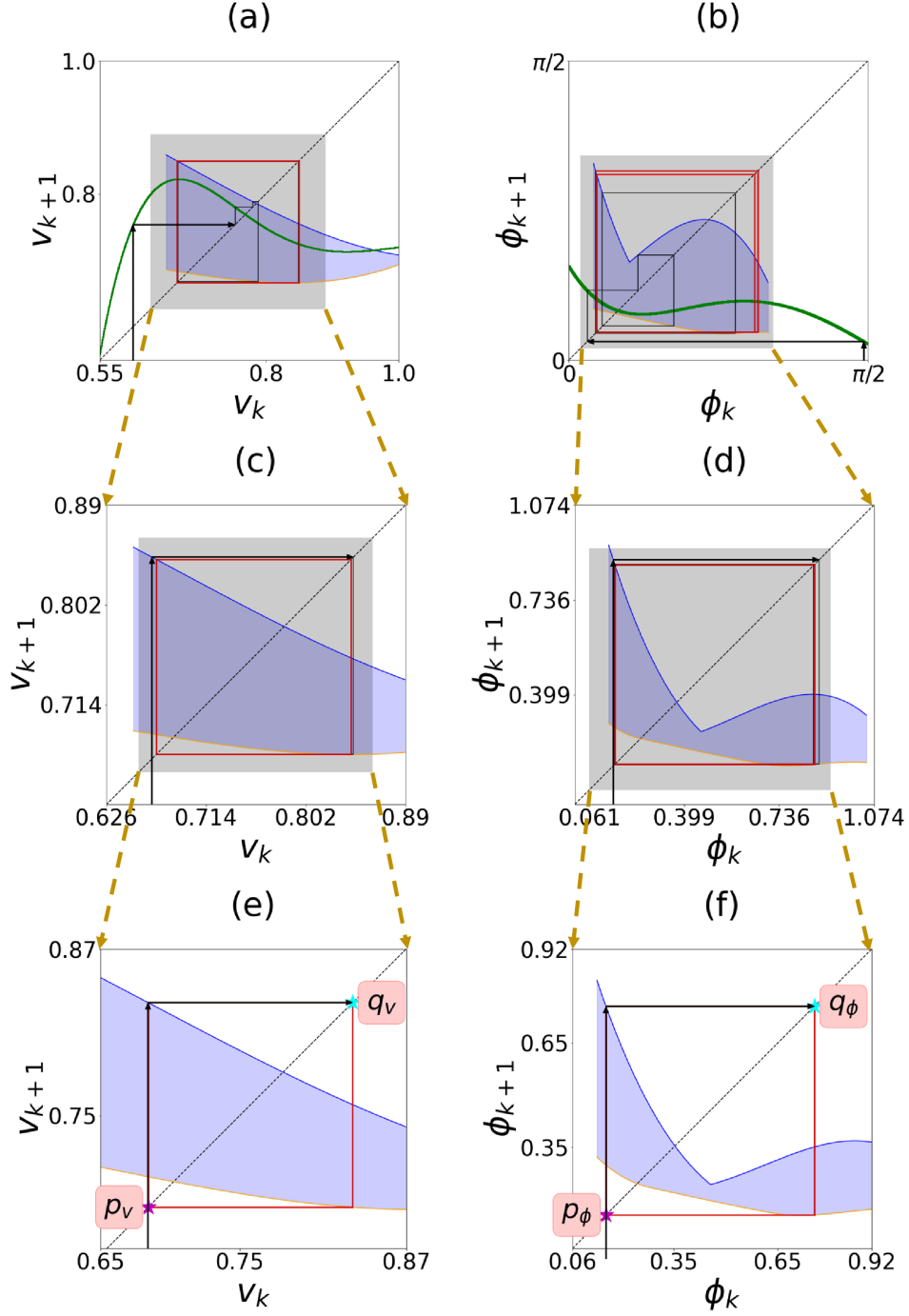


Fig. 18: Illustration of the 1<sup>st</sup>, 2<sup>nd</sup>, and 11<sup>th</sup> update of the auxiliary map  $\mathcal{M}_{\mathcal{A}}^{(N)}$  (6.3), for Case PD ( $d = 0.30$ ), using the same procedure as in Fig. 16. Here  $\mathcal{A}_1^{(1)} = \mathcal{R}_1^+$  (6.7) in (a) and (b); for  $N = 2$  in (c) and (d),  $\mathcal{A}_1^{(2)} : v_k \in [0.666, 0.850]$  and  $\phi_k \in [0.146, 0.977]$ ; and for  $N = 11$  in (e) and (f),  $\mathcal{A}_1^{(11)} : v_k \in [0.684, 0.832]$  and  $\phi_k \in [0.156, 0.758]$ , where the size of  $\mathcal{A}_1^{(N)}$  for  $N > 1$  follows directly from the limiting (red) behavior in  $N - 1$ <sup>st</sup> update ((6.4)-(6.5)). As in Fig. 16, the gray boxes and dashed arrows between figures indicate the zoom-in region in the next row. The stars with  $(p_v, q_v)$  and  $(p_\phi, q_\phi)$  in panels (e) and (f) indicate the min and max of the attracting orbit.

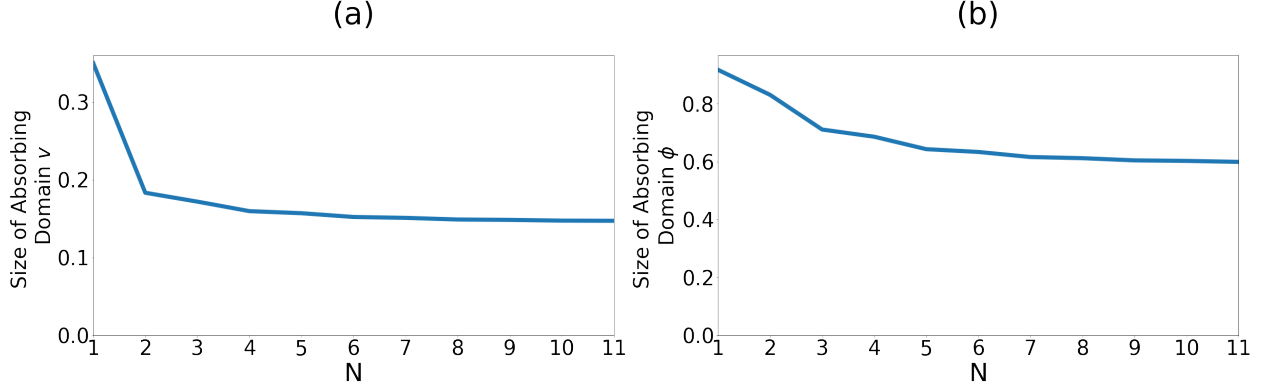


Fig. 19: Illustration of the size of the absorbing domain for case PD that decreases to a limiting size, with the final limiting size as 0.1472 and 0.5991 for  $v$  and  $\phi$ , respectively.

753  $q_v$  and  $p_\phi$ ,  $q_\phi$ ,  $\sigma_\phi$  and  $\gamma_\phi$  in Fig. 20. Then  $p_v$ ,  $q_v$ ,  $p_\phi$  and  $q_\phi$ , provide the range of the attracting region. The  
 754 unstable fixed point  $\phi_u$  between  $p_\phi$  and  $\gamma_\phi$  confirms that all trajectories are absorbed into the 4-cycle, as  
 755 shown in Fig. 20(d), and  $p_\phi, \gamma_\phi$  correspond to the two smallest values of the period-4 fixed points. Further  
 756 discussion is given in Remark 6.2.

757 The following statement summarizes the results for the existence of a globally attracting absorbing  
 758 domain on the auxiliary composite map  $\mathcal{M}_A^{(N)}$ , also indicating the extension of the result to higher-order  
 759 cycles of the auxiliary map that may appear for parameters not considered here, e.g., other values of  $d$ . To  
 760 streamline this Remark 6.2, we assume that the update index  $N$  is sufficiently large so that the periodic  
 761 cycle and corresponding absorbing domain of  $\mathcal{M}_A^{(N)}$  has reached its limiting size, thus not changing with  
 762 increased  $N$ . For example, for the PD case shown in Fig. 18, a good choice would be  $N \geq 11$ .

763

764 **Remark 6.2.** [Existence of an Absorbing Domain (sufficient conditions)]. A globally stable  $m$ -cycle of the  
 765 auxiliary map  $\mathcal{M}_A^{(N)}$  with  $A_1^{(N)} \in R_1^+$  bounds a globally stable absorbing domain  $\mathcal{D}^{(N)} = \{p_v < v_k < q_v, p_\phi <$   
 766  $\phi_k < q_\phi\}$ . Here,  $p_v$  and  $q_v$  are, respectively, the smallest and largest values of the period- $m$  fixed point of the  
 767  $m^{\text{th}}$  iterate map for  $v_{k+m}(v_k)$ , obtained analogously to (6.12) and (6.14) via  $m$  iterates of (6.1). Similarly,  
 768  $p_\phi$  and  $q_\phi$  are the smallest and largest values of the period- $m$  fixed points of the corresponding  $m^{\text{th}}$  iterate map  
 769  $\phi_{k+m}(\phi_k)$ . In general, we expect the  $m$ -cycles of the auxiliary map to occur for  $m$  even, given its max/min  
 770 structure.

771 As described in Section 6.1, one can apply the auxiliary approach for all regions  $\mathcal{R}_j$  for  $j = 2, 3, 4, 5$ ,  
 772 which confirms the transient behavior for regions outside of  $\mathcal{R}_1$ . Combining this transient behavior with the  
 773 results of this section, we have the complete confirmation of the bounds on the attracting domains for  $\mathcal{M}$   
 774 for different  $d$ , obtained via the limiting regions of the auxiliary map as applied in Sections 6.2, 6.3.

775 **7. Conclusion.** While the study of VI systems through local stability analysis has gained significant  
 776 momentum, understanding their global dynamics and bifurcations remains challenging due to the limited  
 777 applicability of classical global stability methods developed for smooth dynamical systems. In particular,  
 778 the focus in the engineering literature has been on linear stability and bifurcations, yet global behavior is  
 779 important in design.

780 In this paper, we propose a computer-assisted analysis based on reduced smooth maps for studying  
 781 the global dynamics of the VI pair. The framework is designed to be generic, ideally for application to  
 782 other non-smooth dynamical systems. The global stability analysis is facilitated by an approximation of  
 783 the exact map for the states at impact, specifically the relative impact velocity  $\dot{Z}_k$  between the outer (the  
 784 capsule) and the inner (the ball) masses and the impact phase  $\psi_k$  relative to the forcing. The exact non-  
 785 smooth maps for these quantities are given by complex coupled transcendental equations for  $\dot{Z}_k$  and  $\psi_k$ .  
 786 While the non-smooth dynamics present a challenge in using commonly defined maps, they also provide  
 787 an opportunity for designing a new approach for impacting systems. Specifically, we use short sequences

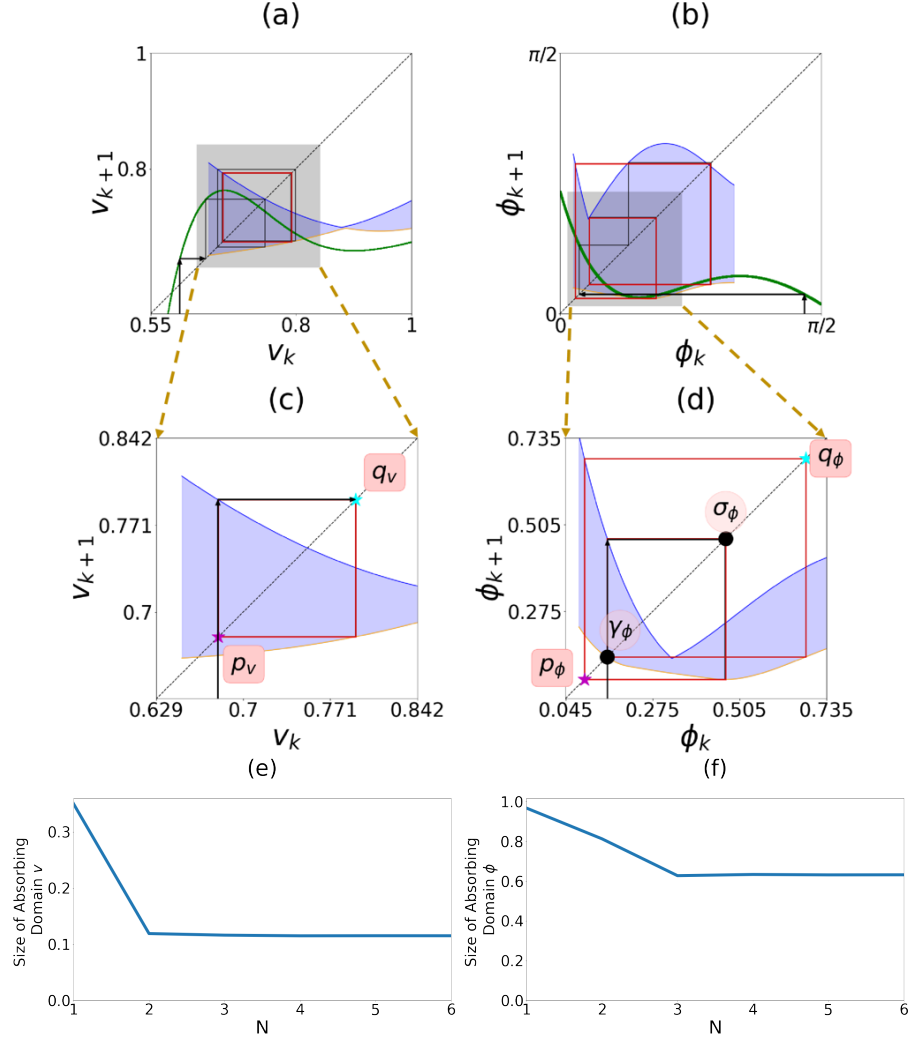


Fig. 20: Illustration of the 1<sup>st</sup> and 2<sup>nd</sup> update of the auxiliary map  $\mathcal{M}_{\mathcal{A}}^{(N)}$  (6.3), for  $d = 0.26$ , corresponding to Case CD, using the same procedure as in Fig. 16. Here,  $\mathcal{A}_1^{(1)} = \mathcal{R}_1^+$  (6.8) in (a) and (b); for  $N = 6$  in (c) and (d),  $v_k \in [0.673, 0.789]$  and  $\phi_k \in [0.093, 0.725]$ . As above, the size of  $\mathcal{A}_1^{(N)}$  for  $N > 1$  follows directly from the limiting (red) behavior at the  $N - 1$ <sup>st</sup> update ((6.4)-(6.5)). As in Fig. 16, the gray boxes and dashed arrows between figures indicate the zoom-in region in row 2. The limiting periodic behavior is 2-cycle and 4-cycle for the (decoupled) auxiliary maps of  $v_k$  and  $\phi_k$ . Panels (e) and (f) show the decrease of the size of the absorbing domain to a limiting size with the limiting size equal to 0.115 and 0.631 for  $v$  and  $\phi$ , respectively. The stars with  $(p_v, q_v)$  and  $(p_\phi, q_\phi)$  in panels (c) and (d) indicate the min and max of the attracting orbit.

788 of returns to one side of the capsule to define building blocks for the maps. The output of such a return  
789 map yields surfaces for  $\dot{Z}_{k+1}$  and  $\psi_{k+1}$  in terms of  $\dot{Z}_k$  and  $\psi_k$ . Return maps based on these building blocks  
790 give the foundation for dividing the state space into a small number of regions with potentially attracting or  
791 transient behavior, thus yielding valuable, distinguishing features that can be used for global stability results.  
792 Generating polynomial approximations of the exact return maps for  $\dot{Z}_k$  and  $\psi_k$  on each region in state space,  
793 we combine these to obtain a piecewise smooth approximate composite map to reconstruct the dynamics of  
794 the system. This framework is computationally efficient. It reduces the main computation to constructing  
795 polynomial return maps for only short-time realizations of the impact pair over the space of initial conditions,

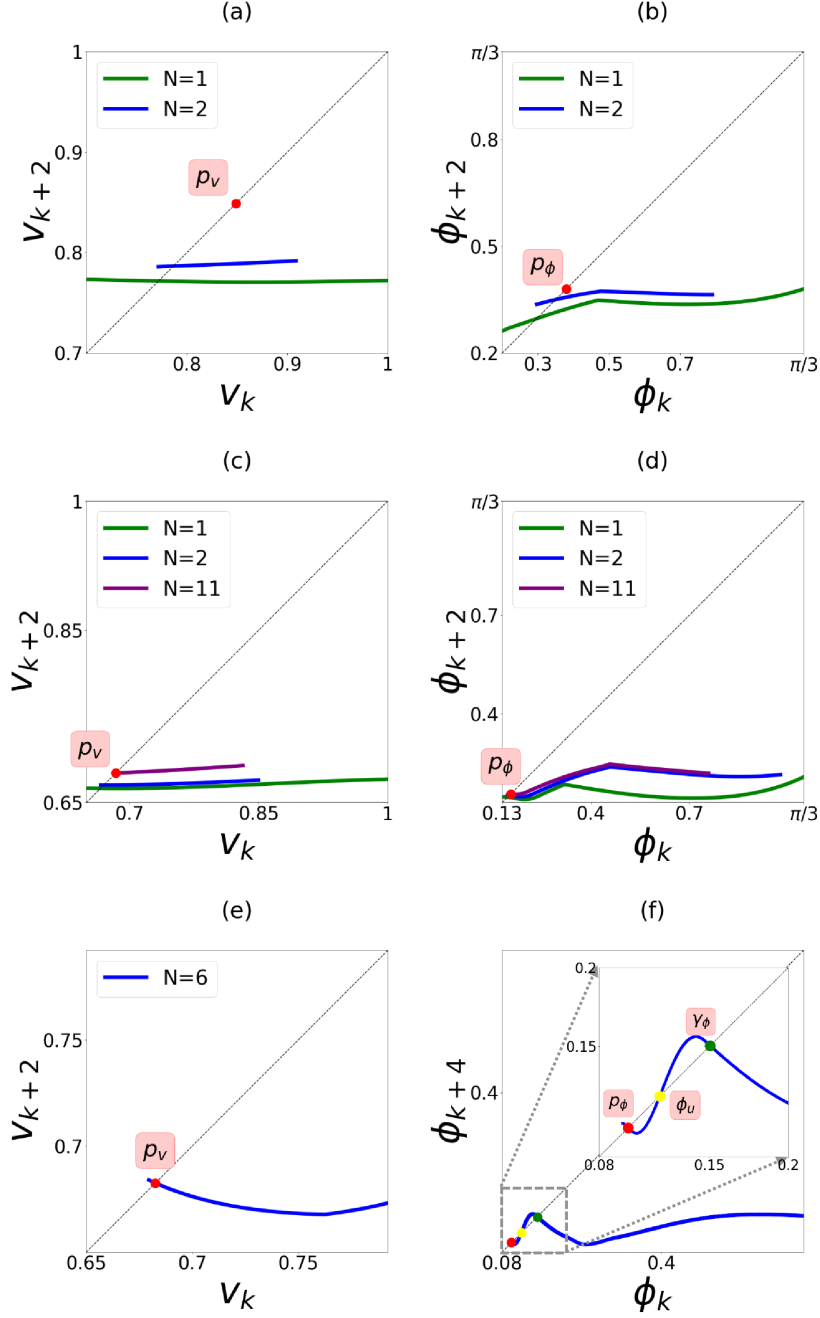


Fig. 21: Curves for the  $m^{\text{th}}$  iterate maps of  $\mathcal{M}_A^{(N)}$ , obtained from (6.9) and (6.12), intersecting the diagonals at  $v_{\min}$  and  $\phi_{\min}$ , with limiting values  $p_v$  and  $p_\phi$ , respectively, for sufficiently large  $N$ . Panels (a),(b): the FP case for  $N = 1, 2$ ; by  $p_v$  and  $p_\phi$ , respectively. Panels (c),(d): the PD case for  $N = 1, 2, 11$ . Panels (e) and (f): Case CD with the second iterate map for  $v_k$  (6.9) and the fourth iterate map for  $\phi_k$  (6.14) for  $N = 6$ . The zoomed inset in (f) highlights the intersection of two smallest fixed points,  $p_\phi$  and  $\gamma_\phi$ , of the period-4 cycle of the auxiliary map, also shown in Fig. 20(b). The point  $\phi_u$  is the unstable fixed point between these two values.

796 in contrast to long-time simulations over the entire state space traditionally used in deriving flow-defined  
 797 Poincaré maps for global dynamics of limit-cycle or chaotic systems. Yet, our approximate return maps can  
 798 be viewed as geometrical models of VI pair systems, analogous to geometrical Lorenz maps used to analyze  
 799 global dynamics and bifurcations in the chaotic Lorenz system [2, 44, 23] and its more analytically tractable  
 800 piecewise smooth counterpart [7]. While certain aspects of the computation-based analysis do not rely on  
 801 finding polynomial approximations for the return maps, we pursue them with the goal of explicit expressions  
 802 for the global analysis.

803 Anchored in relatively simple return maps, our framework is valuable for cobweb analysis in the phase  
 804 planes of the state variables. The relevant global analysis is facilitated by introducing 1D auxiliary maps  
 805 based on the extreme bounds of the 2D maps in the regions with different types of dynamics. Repeated  
 806 updates of these auxiliary maps within regions with attracting dynamics yield attraction basins for limit-  
 807 cycle and chaotic dynamics. Thus, our computer-assisted method of reducing non-smooth systems into a  
 808 composite piecewise smooth map provides a framework to study the global dynamics of non-smooth systems  
 809 with impacts. Here, we have focused on parameter regions corresponding to energetically favorable states  
 810 in VI pair-based energy harvesting systems, so that the results are relevant for recent designs of VI-based  
 811 energy harvesters [57] and nonlinear energy transfer [28]. While motivated by a specific vibro-impact energy  
 812 harvester, nevertheless, our approach uses generic return maps composed of short sequences of impacts that,  
 813 in turn, decompose the full dynamics. Thus, the paradigm can be generalized for application in other non-  
 814 smooth systems. It may also be interesting to see if this approach, motivated by a particular class of applied  
 815 models, is relevant for 2D maps considered in generic mathematical settings [35].

816 Adapting these findings to realistic external environments remains critical for future exploration. Fu-  
 817 ture work will focus on refining these theoretical frameworks and methodologies to effectively integrate  
 818 vibro-impact systems into practical applications. This pursuit involves enhancing our understanding of the  
 819 underlying dynamics and engineering solutions that can withstand and thrive in realistic external environ-  
 820 ments.

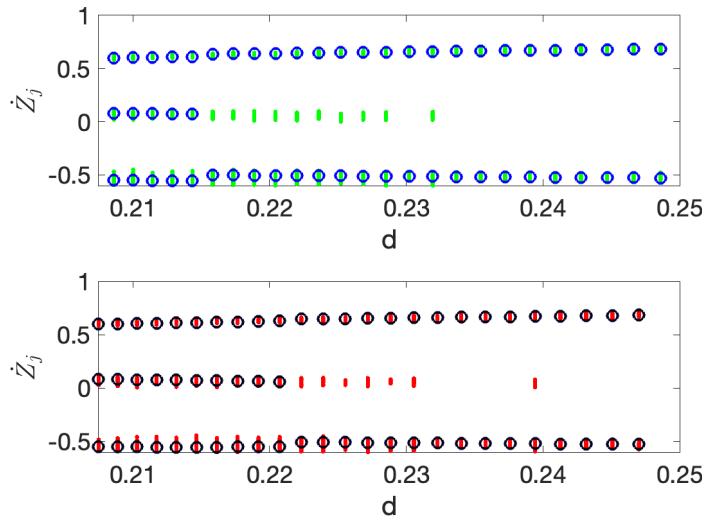


Fig. 22: Bifurcation diagrams for  $\dot{Z}_j$  from (2.6) based on continuation-type methods for decreasing  $d$  (top) and increasing  $d$  (bottom). Blue and black open circles correspond to deterministic forcing, and green and red dots correspond to additive noise forcing via an Ornstein-Uhlenbeck process  $\zeta$ , with limiting behavior  $\zeta \sim N(0, 0.002)$ . Parameters:  $r = 0.25$ ,  $\beta = \pi/6$ .

821 One example of a realistic external setting is the consideration of the VI energy harvester, illustrated in  
 822 Fig. 1(a), under stochastic external forcing. Figure 22 gives the bifurcation structure with two different types  
 823 of periodic behavior for the system (2.1)-(2.3), shown via the impact velocity  $\dot{Z}_j$  vs. the non-dimensional  
 824 capsule length parameter  $d$ . Both panels show deterministic (open circles) vs. stochastic (dots) results for

825  $\dot{Z}_j$ . The top and bottom panels show bifurcation diagrams obtained via a continuation-type method for  
 826 decreasing and increasing  $d$ , respectively. Comparing these indicates bi-stability of two different periodic  
 827 behaviors. For larger  $d$ , we observe 1:1 periodic behavior with alternating impacts on  $\partial T$  with  $\dot{Z}_j < 0$  and  $\partial B$   
 828 with  $\dot{Z}_j > 0$  per forcing period. For smaller  $d$ , we observe 2:1 behavior with two impacts on  $\partial B$  followed by a  
 829 single impact on  $\partial T$  per forcing period. The bi-stability is apparent from the co-existence of branches for the  
 830 1:1 and 2:1 solutions in a range of  $d$ , approximately  $0.221 < d < .216$ . At the same time, the stochastic results  
 831 shown by the green and red points indicate the regular appearance of 2:1 behavior, even for larger values of  
 832  $d$  beyond the region of bi-stability. A preliminary analysis, based on the algorithm from Section 4 with an  
 833 augmented set of return maps analogous to (3.1), includes both  $\mathcal{P}_{BTB}$  to capture 1:1 behavior and a new  
 834 map  $\mathcal{P}_{BBTB}$  to capture 2:1 behavior. These maps capture the attraction to either 1:1 and 2:1 behaviors or  
 835 both. Furthermore, this novel return map framework also provides critical information about the stochastic  
 836 sensitivity of the 1:1 behavior. Specifically, the geometry of the surfaces of these maps, analogous to those  
 837 shown in Fig. 6, indicates how the noise can bias the dynamics towards 2:1 behavior. We leave the details  
 838 of that analysis to future work, noting that the algorithm's combined flexibility and efficiency allow for a  
 839 straightforward augmentation that includes new return maps representing the 2:1 behavior. Then, within the  
 840 dynamical characterization of the state space provided by our algorithm, we can study non-smooth dynamics  
 841 in a stochastic setting.

842 This paper has focused on the development of a novel return map formulation as the basis for a computer-  
 843 assisted global analysis, obtaining explicit expressions wherever possible. There are a number of other fea-  
 844 tures that we expect are valuable for future generalizations that we have not pursued here. For example,  
 845 we expect that more steps of the algorithm could be automated, such as integrating defined criteria to aid  
 846 in partitioning and comparing approximations for different orders of polynomials for the composite map.  
 847 Furthermore, while we have given the algorithm in terms of 2D maps for simplicity of exposition, we expect  
 848 that the ideas of this approach can be adapted to higher dimensions. In addition, if we relax the demand for  
 849 a nearly explicit global analysis, we anticipate that accurate auxiliary maps that are purely computation-  
 850 based could be used to approximate the attracting region(s).

851

852

## REFERENCES

- 853 [1] V. ACARY, H. DE JONG, AND B. BROGLIATO, *Numerical simulation of piecewise-linear models of gene regulatory networks*  
 854 *using complementarity systems*, Physica D: Nonlinear Phenomena, 269 (2014), pp. 103–119.
- 855 [2] V. AFRAIMOVICH, V. BYKOV, AND L. SHILNIKOV, *The origin and structure of the Lorenz attractor*, Dokl. Akad. Nauk  
 856 USSR, 234 (1977), pp. 336–339.
- 857 [3] A. A. ANDRONOV, A. A. VITT, AND S. E. KHAIKIN, *Theory of Oscillations*, Fizmatgiz, Moscow, 1959.
- 858 [4] V. AVRUTIN, L. GARDINI, I. SUSHKO, AND F. TRAMONTANA, *Continuous and discontinuous piecewise-smooth one-*  
 859 *dimensional maps: invariant sets and bifurcation structures*, World Scientific, 2019.
- 860 [5] I. BELYKH, M. BOCIAN, A. R. CHAMPNEYS, K. DALEY, R. JETER, J. H. MACDONALD, AND A. MCROBIE, *Emergence of*  
 861 *the London Millennium Bridge instability without synchronisation*, Nature Communications, 12 (2021), p. 7223.
- 862 [6] I. BELYKH, R. KUSKE, M. PORFIRI, AND D. J. W. SIMPSON, *Beyond the Bristol book: Advances and perspectives in non-*  
 863 *smooth dynamics and applications*, Chaos: An Interdisciplinary Journal of Nonlinear Science, 33 (2023), p. 010402.
- 864 [7] V. N. BELYKH, N. V. BARABASH, AND I. V. BELYKH, *Sliding homoclinic bifurcations in a Lorenz-type system: Analytic*  
 865 *proofs*, Chaos: An Interdisciplinary Journal of Nonlinear Science, 31 (2021), p. 043117.
- 866 [8] V. N. BELYKH AND I. BELYKH, *Belykh map*, Scholarpedia, 6 (2011), p. 5545.
- 867 [9] L. BENADERO, A. EL AROUDI, G. OLIVAR, E. TORIBIO, AND E. GOMEZ, *Two-dimensional bifurcation diagrams: background*  
 868 *pattern of fundamental DC–DC converters with PWM control*, International Journal of Bifurcation and Chaos, 13  
 869 (2003), pp. 427–451.
- 870 [10] Z. CAO, H. MA, X. YU, J. SHI, H. YANG, Y. TAN, AND G. REN, *Global dynamics of a vibro-impact energy harvester*,  
 871 Mathematics, 10 (2022), p. 472.
- 872 [11] S. COOMBES AND P. C. BRESSLOFF, *Mode locking and arnold tongues in integrate-and-fire neural oscillators*, Physical  
 873 Review E, 60 (1999), p. 2086.
- 874 [12] D. COSTA, R. KUSKE, AND D. YURCHENKO, *Qualitative changes in bifurcation structure for soft vs hard impact models*  
 875 *of a vibro-impact energy harvester*, Chaos, 32 (2022), p. 103120.
- 876 [13] H. DANKOWICZ AND X. ZHAO, *Local analysis of co-dimension-one and co-dimension-two grazing bifurcations in impact*  
 877 *microactuators*, Physica D: Nonlinear Phenomena, 202 (2005), pp. 238–257.
- 878 [14] G. DERKS, P. GLENDINNING, AND A. SKELDON, *Creation of discontinuities in circle maps.*, Proc. R. Soc. A, 477 (2021),  
 879 p. 20200872.
- 880 [15] M. DI BERNARDO, C. BUDD, A. CHAMPNEYS, AND P. KOWALCZYK, *Piecewise-smooth Dynamical Systems: Theory and*  
 881 *Applications*, Springer, 2007.
- 882 [16] M. DI BERNARDO, C. J. BUDD, A. R. CHAMPNEYS, P. KOWALCZYK, A. B. NORDMARK, G. O. TOST, AND P. T. PIIRONEN,

- 883 *Bifurcations in nonsmooth dynamical systems*, SIAM Review, 50 (2008), pp. 629–701.
- 884 [17] M. DI BERNARDO, M. I. FEIGIN, S. J. HOGAN, AND M. E. HOMER, *Chaos, Solitons and Fractals*, 10 (1999), pp. 1881–1908.
- 885 [18] M. DI BERNARDO, F. GAREFALO, L. GLIELMO, AND F. VASCA, *Switchings, bifurcations, and chaos in DC/DC converters*,
- 886 *IEEE Transactions on Circuits and Systems I: Fundamental Theory and Applications*, 45 (1998), pp. 133–141.
- 887 [19] M. F. DIMENTBERG AND D. V. IOURTCHEIKO, *Random Vibrations with Impacts: A Review*, *Nonlinear Dynamics*, 36
- 888 (2004), pp. 229–254.
- 889 [20] B. ERMENTROUT, Y. PARK, AND D. WILSON, *Recent advances in coupled oscillator theory*, *Philosophical Transactions of*
- 890 *the Royal Society A*, 377 (2019), p. 20190092.
- 891 [21] A. FILIPPOV, *Differential Equations with Discontinuous Right-Hand Sides*, Kluwer Academic Press, 1988.
- 892 [22] P. GLENDINNING, *The border collision normal form with stochastic switching surface.*, *SIAM J. Appl. Dyn. Syst.*, 13
- 893 (2014), pp. 181–193.
- 894 [23] J. GUCKENHEIMER AND P. HOLMES, *Nonlinear Oscillations, Dynamical Systems, and Bifurcations of Vector Fields*, vol. 42,
- 895 Springer, 1983.
- 896 [24] M. HASLER, V. BELYKH, AND I. BELYKH, *Dynamics of stochastically blinking systems. Part II: Asymptotic properties*,
- 897 *SIAM Journal on Applied Dynamical Systems*, 12 (2013), pp. 1031–1084.
- 898 [25] R. A. IBRAHIM, *Vibro-impact dynamics: Modeling, mapping and applications*, *Lecture Notes in Applied and Computa-*
- 899 *tional Mechanics*, (2009).
- 900 [26] M. JEFFREY, *Hidden Dynamics. The Mathematics of Switches, Decisions and Other Discontinuous Behaviour*, Springer,
- 901 New York, 2018.
- 902 [27] ———, *Modeling with Nonsmooth Dynamics.*, vol. 7 of *Frontiers in Applied Dynamical Systems: Reviews and Tutorials*,
- 903 Springer, New York, 2020.
- 904 [28] R. KUMAR, R. KUSKE, AND D. YURCHENKO, *Exploring effective TET through a vibro-impact nonlinear energy sink over*
- 905 *broad parameter regimes*, *Journal of Sound and Vibration*, 570 (2024), p. 118131.
- 906 [29] S. KWAN, A. LEE, C. ATHANASOULI, R. KUMAR, AND R. KUSKE, *Markov chain modeling of inelastic impacts in energy*
- 907 *harvesters*, GT REU Summer Program 2023, poster.
- 908 [30] Z. LAI AND E. RODGERS, *On energy harvesting from a vibro-impact oscillator with dielectric membranes*, *Mechanical*
- 909 *Systems and Signal Processing*, 107 (2018), pp. 105–121.
- 910 [31] R. I. LEINE AND T. HEIMSCH, *Global uniform asymptotic attractive stability of the non-autonomous bouncing ball system*,
- 911 *Physica D: Nonlinear Phenomena*, 241 (2012), pp. 2029–2041.
- 912 [32] R. I. LEINE AND H. NIJMEIJER, *Dynamics and bifurcations of non-smooth mechanical systems*, vol. 18, Springer Science
- 913 & Business Media, 2013.
- 914 [33] H. LI, A. LI, X. KONG, AND H. XIONG, *Dynamics of an electromagnetic vibro-impact nonlinear energy sink, applications*
- 915 *in energy harvesting and vibration absorption*, *Nonlinear Dynamics*, (2022), pp. 1807–1819.
- 916 [34] T. LI, S. SEGUY, AND A. BERLIOZ, *Optimization mechanism of targeted energy transfer with vibro-impact energy sink*
- 917 *under periodic and transient excitation*, *Nonlinear Dynamics*, 87 (2017), p. 2415–2433.
- 918 [35] R. LOZI, L. EFREMOVA, M.-S. ABDELOUAHAB, S. EL ASSAD, AND M. PLUHACEK, *Foreword to the special issue of Journal*
- 919 *of Difference Equations and Applications on Lozi, Henon, and other chaotic attractors, theory and applications*,
- 920 *Journal of Difference Equations and Applications*, 29 (2023), pp. 861–875.
- 921 [36] A. C. LUO AND R. P. HAN, *The dynamics of a bouncing ball with a sinusoidally vibrating table revisited*, *Nonlinear*
- 922 *Dynamics*, 10 (1996), pp. 1–18.
- 923 [37] A. C. J. LUO AND Y. GUO, *Vibro-Impact Dynamics*, John Wiley & Sons Ltd, Oxford, UK, 2013.
- 924 [38] G. W. LUO, X. H. LV, AND L. MA, *Periodic-impact motions and bifurcations in dynamics of a plastic impact oscillator*
- 925 *with a frictional slider*, *European Journal of Mechanics, A/Solids*, (2008).
- 926 [39] J. F. MASON AND P. T. PHIROINEN, *Interactions between global and grazing bifurcations in an impacting system*, *Chaos:*
- 927 *An Interdisciplinary Journal of Nonlinear Science*, 21 (2011), p. 013113.
- 928 [40] A. B. NORDMARK, *Non-periodic motion caused by grazing incidence in an impact oscillator*, *Journal of Sound and*
- 929 *Vibration*, 145 (1991), pp. 279–297.
- 930 [41] A. B. NORDMARK, *Universal limit mapping in grazing bifurcations*, *Physical Review E*, 55 (1997), p. 266.
- 931 [42] E. PAVLOVSKAIA, M. WIERCIGROCH, AND C. CELSO GREBOGI, *Two-dimensional map for impact oscillator with drift*, *Phys.*
- 932 *Rev. E*, 70 (2004), p. 036201.
- 933 [43] A. POLYNIKIS, S. HOGAN, AND M. DI BERNARDO, *Comparing different ode modelling approaches for gene regulatory*
- 934 *networks*, *Journal of Theoretical Biology*, 261 (2009), pp. 511–530.
- 935 [44] C. ROBINSON, *Homoclinic bifurcation to a transitive attractor of Lorenz type*, *Nonlinearity*, 2 (1989), p. 495.
- 936 [45] M. SAHARI, A.-K. TAHA, AND L. RANDRIAMIHAMISON, *Bifurcations in 2D spatiotemporal maps*, *International Journal of*
- 937 *Bifurcation and Chaos*, 31 (2021), p. 2150091.
- 938 [46] L. SERDUKOVA, R. KUSKE, AND D. YURCHENKO, *Stability and bifurcation analysis of the period-T motion of a vibroimpact*
- 939 *energy harvester*, *Nonlinear Dynamics*, 98 (2019), pp. 1807–1819.
- 940 [47] L. SERDUKOVA, R. KUSKE, AND D. YURCHENKO, *Post-grazing dynamics of a vibro-impacting energy generator*, *Journal of*
- 941 *Sound and Vibration*, 492 (2021), p. 115811.
- 942 [48] L. SERDUKOVA, R. KUSKE, AND D. YURCHENKO, *Fundamental competition of smooth and non-smooth bifurcations and*
- 943 *their ghosts in vibro-impact pairs*, *Nonlinear Dyn*, 111 (2023), p. 6129–6155.
- 944 [49] A. D. SHAW, A. R. CHAMPNEYS, AND M. I. FRISWELL, *Normal form analysis of bouncing cycles in isotropic rotor stator*
- 945 *contact problems*, *International Journal of Mechanical Sciences*, 155 (2019), pp. 83–97.
- 946 [50] S. W. SHAW AND R. H. RAND, *The transition to chaos in a simple mechanical system*, *International Journal of Non-Linear*
- 947 *Mechanics*, 24 (1989), pp. 41–56.
- 948 [51] D. SIMPSON, V. AVRUTIN, AND S. BANERJEE, *Nordmark map and the problem of large-amplitude chaos in impact oscilla-*
- 949 *tors*, *Phys. Rev. E*, 102 (2020), p. 022211.
- 950 [52] D. J. W. SIMPSON, *Detecting invariant expanding cones for generating word sets to identify chaos in piecewise-linear*



951 *maps*, Journal of Difference Equations and Applications, 29 (2023), pp. 1094–1126.

952 [53] D. J. W. SIMPSON AND R. KUSKE, *The influence of localized randomness on regular grazing bifurcations with applications*

953 *to impacting dynamics*, Journal of Vibration and Control, 24 (2018), pp. 407–426.

954 [54] P. THOTA, X. ZHAO, AND H. DANKOWICZ, *Co-dimension-two grazing bifurcations in single-degree-of-freedom impact*

955 *oscillators*, Journal of Computational and Nonlinear Dynamics, 1 (2006), pp. 328–335.

956 [55] A. F. VAKAKIS, O. V. GENDELMAN, L. A. BERGMAN, A. MOJAHED, AND M. GZAL, *Nonlinear targeted energy transfer:*

957 *state of the art and new perspectives*, Nonlinear Dynamics, 108 (2022), p. 711–741.

958 [56] D. YURCHENKO, *Tuned Mass and Parametric Pendulum Dampers Under Seismic Vibrations*, Springer Berlin Heidelberg,

959 Berlin, Heidelberg, 2014, pp. 1–22.

960 [57] D. YURCHENKO, Z. LAI, G. THOMSON, D. VAL, AND R. BOBRYK, *Parametric study of a novel vibro-impact energy*

961 *harvesting system with dielectric elastomer*, Applied Energy, 208 (2017), pp. 456–470.

962 [58] Y. ZHANG AND X. FU, *Stability of periodic motions in an inclined impact pair*, Eur. Phys. J. Spec. Top., 228 (2019),

963 pp. 1441–1457.

964 [59] Z. T. ZHUSUBALIYEV AND E. MOSEKILDE, *Bifurcations and chaos in piecewise-smooth dynamical systems: applications*

965 *to power converters, relay and pulse-width modulated control systems, and human decision-making behavior*, vol. 44,

966 World Scientific, 2003.

## 967 Appendix A. Return Maps and Composite Map Construction.

968 **A.1. Division of state space for the return maps.** We show the regions in the state space  $(\dot{Z}_k, \psi_k)$

969 whose images correspond to BB, BTB, and BTTB motion, with  $P_{BB}$  and  $P_{BTB}$  as defined in (3.1) in Section

970 3, and  $P_{BTTB}$ . Figure 23 shows the full range of  $\psi_k$ , from 0 to  $2\pi$ , and a larger range of  $\dot{Z}_k$  as compared

971 to Fig. 3. The region with  $\phi_k > \pi$  is comprised of mostly BB motion and, as discussed in Remark 3.2 and

972 shown in Fig. 7, is strongly transient. Likewise, the yellow regions, corresponding to BTTB motion, are

973 strongly transient for  $\beta > 0$ , which drives the motion away from multiple impacts on the top membrane  $\partial T$ .

974 Therefore, we restrict our attention to the state space with range  $\psi_k \in [0, \pi]$  and  $\dot{Z}_k \leq 1.25$  (below the yellow

975 regions) when constructing the composite map  $\mathcal{M}$ , with a focus on understanding the attracting region and

976 those regions in state space in close proximity to it.

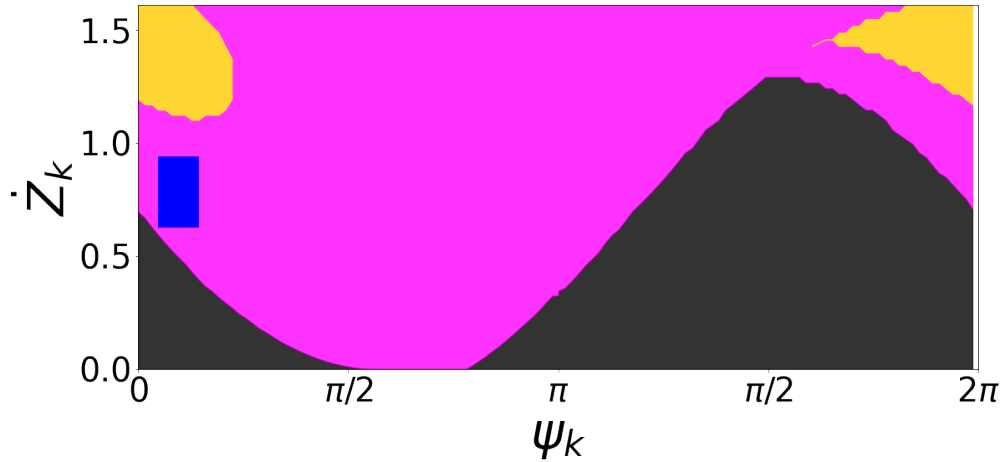


Fig. 23: Division of the  $(\dot{Z}_k, \psi_k)$  state space, corresponding to exact return maps with BTB motion (blue and magenta regions), BB motion (black regions), and BTTB motion (yellow regions). Parameter:  $d = 0.26$ .

977 **A.2. Phase plane projection of the exact maps.** Figure 24 shows the projections of the exact

978 maps, defined by (3.1) in Section 3, on the  $\dot{Z}_k - \dot{Z}_{k+1}$  and  $\psi_k - \psi_{k+1}$  phase planes, as referenced in Remark

979 3.2. This 2-D projection of Fig. 6 gives separate views of the dynamics for  $\dot{Z}_k$  and  $\psi_k$  in their respective

980 phase planes. The points delineate curves for  $\dot{Z}_{k+1}$  and  $\psi_{k+1}$  in the image of the return map, some of which

981 cross both diagonals in the  $\dot{Z}_k - \dot{Z}_{k+1}$  and  $\psi_k - \psi_{k+1}$  planes. The slopes of the curves that intercept the

982 diagonals suggest that there is a smaller subregion of the state space  $(\dot{Z}_k, \psi_k)$  that is attracting.

983 **A.3. Comments on Region  $\mathcal{R}_1$ .** In the next six sections of the appendix, we further comment on

984 the details of the algorithm implementation for the specific VI pair model, as discussed in Section 4.2.

985 In order to capture the full dynamics for all  $d$  near the diagonals of both phase planes  $\dot{Z}_k - \dot{Z}_{k+1}$  and

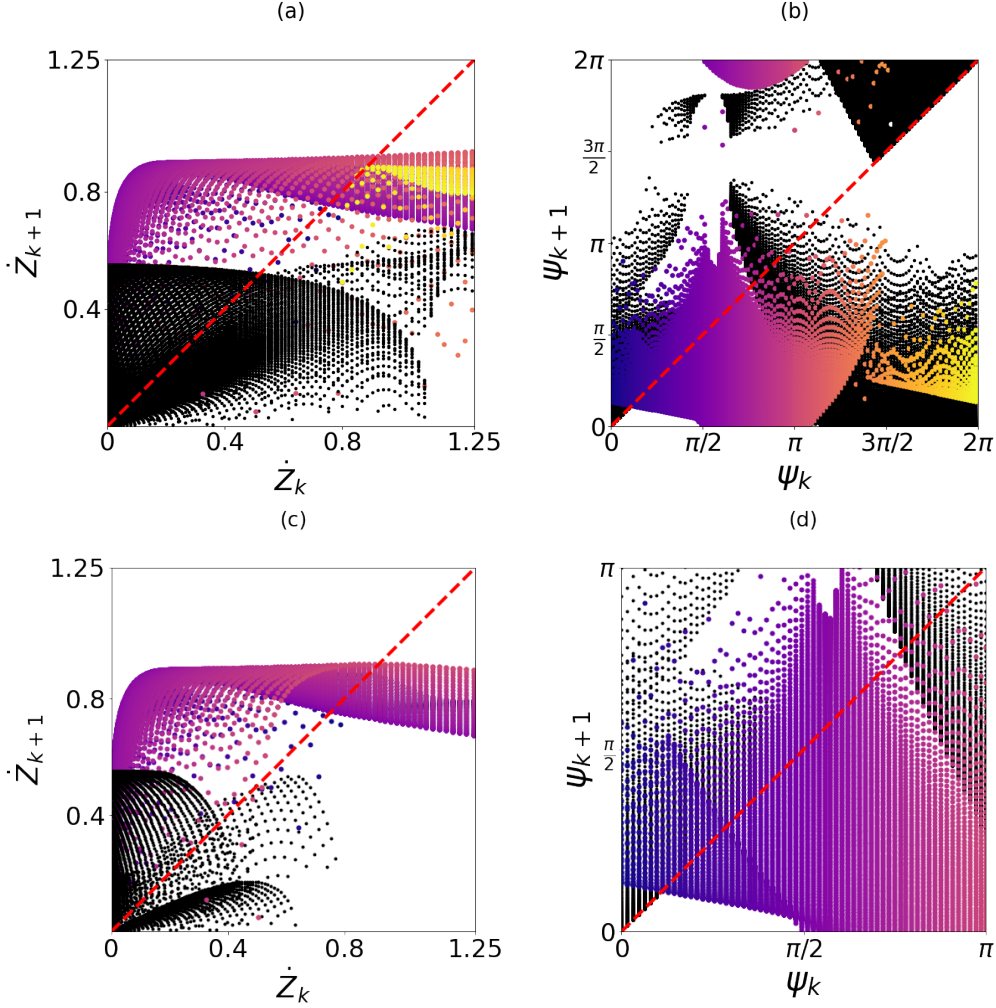


Fig. 24: (a),(b): Using the method illustrated in Fig. 5, we show the first return on  $\partial B$  using (3.1) for fixed values of  $\psi_k$  in the range of  $[0, 2\pi]$  and sweeping through initial values  $\dot{Z}_k \in (0, 1.25)$  with  $d = 0.35$ . The colored points correspond to BTB motion, and the black points correspond to BB motion. The points with the same color on the left and right panels correspond to images from the same  $\psi_k$ . (c),(d): Zoomed-in results from (a)-(b) on the region of state space for  $\psi_k \in (0, \pi)$ , complementing the region shown in Fig. 7.

986  $\psi_k - \psi_{k+1}$ , we define region  $\mathcal{R}_1$  as the union of the subregions obtained using (4.2). Figure 25 illustrates the  
 987 location of the subregion (green) based on the filter in (4.2) corresponding to one  $d$  value. These are shown  
 988 relative to the union of the subregions over all  $d$  in the range of interest (blue). Through this definition, we  
 989 can use the same map for  $\mathcal{R}_1$  for all  $d$  considered rather than finding different approximate maps for each  $d$ .

990 We have explored a range of  $\delta$  values,  $\delta = 1.2, 1.3, 1.4$ , which is the filter parameter in (4.2). In summary,  
 991 a smaller  $\delta$  yields a smaller  $\mathcal{R}_1$  which allows a more accurate approximation of  $f_1$  and  $g_1$  to the surface of the  
 992 exact map. On the other hand, a larger  $\mathcal{R}_1$  can capture more dynamics near this region which is desirable. In  
 993 that case, one can compensate for the increased error associated with larger  $\delta$  by increasing the polynomial  
 994 orders in the approximation. Here, we chose  $\delta = 1.2$  for the benefit of a simpler expression to construct the  
 995 approximate map.

996 In considering the choice for the order of polynomials, we note that higher-order polynomials give  
 997 more accurate approximations, but this will increase the complexity of the 2D map. Hence, we choose the  
 998 lowest order polynomial such that the approximation can also reproduce similar dynamics to the exact map.  
 999 In this case, the polynomial map is quadratic in  $\phi_k$  and cubic in  $v_k$ . Specifically, the polynomials given

1000 in the map  $(f_1(v_k, \phi_k), g_1(v_k, \phi_k))$  (4.3)-(4.4) in  $\mathcal{R}_{1,2}$  approximate the surface using the Matlab function  
 1001 `fit([x,y],z,fitType)` with argument `fitType` set to "poly23". A detailed comparison between the order  
 1002 of the polynomials used in the approximation and the associated error is given in Table 1 and Fig. 26.

1003 Table 1 compares different types of approximation error statistics,  $R^2$ , and the Summation Squared  
 1004 Error (SSE), using different  $\delta$  and different orders of polynomials. Figure 26 indicates that a smaller  $\delta$  gives  
 1005 a better approximation for a given polynomial order, as a larger  $\delta$  includes more variability of the surfaces  
 1006 for  $(\dot{Z}_{k+1}, \psi_{k+1})$ . Table 1 shows that the combination of  $\delta = 1.2$  and the polynomial order poly23 gives the  
 1007 best result.

$\delta$	Poly degree	$v_{k+1}$		$\phi_{k+1}$	
		$R^2$	SSE	$R^2$	SSE
1.2	poly23	0.9992	$2.2705 \times 10^{-5}$	0.9998	$2.2181 \times 10^{-5}$
1.3	poly23	0.99827	0.0025092	0.99984	0.0032939
1.3	poly33	0.99827	0.0025055	0.99994	0.0011577
1.4	poly23	0.99735	0.0055033	0.99981	0.0055713
1.4	poly33	0.99735	0.0054874	0.9999	0.0031359

Table 1: Comparison of the approximation error  $R^2$  and SSE in  $\mathcal{R}_1$  for different  $\delta$  and different polynomial orders. Here,  $R^2 = 1 - \frac{SSE}{SST}$ , where the Summation Squared Error and the Summation Squared Total are given by  $SSE = \sum_i^n (y_i - \hat{y}_i)^2$  and  $SST = \sum_i^n (y_i - \bar{y})^2$ , respectively. Here,  $y_i$  is the exact value corresponding to  $\dot{Z}_{k+1}$  or  $\psi_{k+1}$ , and  $\hat{y}_i$  is the estimation  $v_{k+1}$  or  $\phi_{k+1}$ , and  $\bar{y}$  is the average of all exact values  $\overline{\dot{Z}_{k+1}}$  or  $\overline{\psi_{k+1}}$ .

1008 **A.4. Comments on Region  $\mathcal{R}_2$ .** The surfaces generated over  $\mathcal{R}_2$  correspond to the BTB behavior.  
 1009 As described in Remark 4.1, we use separable maps to represent the dynamics of Region  $\mathcal{R}_2$ . Recall that the  
 1010 separable map takes the form of a single variable polynomial, e.g.  $v_{k+1} = f_2(v_k)$  and  $\phi_{k+1} = g_2(\phi_k)$  (4.5)  
 1011 in this case. Given the strongly transient nature of the dynamics in  $\mathcal{R}_2$ , also indicated by the steep surfaces  
 1012 shown in Fig. 6, this 1-D approximation with separable maps is sufficient to represent the dynamics of  $\mathcal{R}_2$ .

1013 **A.5. Comments on Region  $\mathcal{R}_4$ .** Similar to Region  $\mathcal{R}_2$ , the surfaces over  $\mathcal{R}_4$  also correspond to the  
 1014 BTB behavior. However, the surfaces in this region must be approximated separately because of its steep  
 1015 descending surfaces over smaller values of  $\dot{Z}_k$ , making it difficult to obtain a good approximation over the  
 1016 combined regions of  $\mathcal{R}_2$  and  $\mathcal{R}_4$ . The approximate location of  $\mathcal{R}_4$  is given by  $\{(\dot{Z}, \psi_k) : \dot{Z}_k < 0.55, 1.1 <$   
 1017  $\psi_k < 2.5, \text{ and } \dot{Z}_k > 0.63 - 0.53\psi_k\}$ .

1018 Similar to  $\mathcal{R}_2$ , we use separable maps for the approximation in  $\mathcal{R}_4$ , choosing two 1-D maps that represent  
 1019 the dynamics given by the surfaces for  $\dot{Z}_{k+1}$  and  $\psi_{k+1}$

$$\begin{aligned}
 1020 \quad v_{k+1}(v_k) &= f_4(v_k) = b_{40}v_k^8 + b_{41}v_k^7 + b_{42}v_k^6 + b_{43}v_k^5 + b_{44}v_k^4 + b_{45}v_k^3 + b_{46}v_k^2 + b_{47}v_k + b_{48}, \\
 1021 \quad (A.1) \quad \phi_{k+1}(\phi_k) &= g_4(v_k) = a_{40}\phi_k^4 + a_{41}\phi_k^3 + a_{42}\phi_k^2 + a_{43}\phi_k + a_{44}.
 \end{aligned}$$

1023 The steep drop of the surface for smaller values of  $\dot{Z}_{k+1}$ , as shown in Fig. 11(f), indicates that the dynamics  
 1024 in  $\mathcal{R}_4$  is also strongly transient. That is, at the fixed point of  $v_{k+1} = f_4(v_k)$  the slope is  $|f_4'(v_k)| > 1$ , as  
 1025 shown in Fig. 11(e).

1026 **A.6. Comments on Region  $\mathcal{R}_3$ .** The approximation for  $\mathcal{R}_3$  covers the surfaces in Fig. 6 over the  
 1027 region  $\{(\dot{Z}_k, \psi_k) : 0 < \dot{Z}_k < 0.63 - 0.53\psi_k\}$  within the state space considered. The approximations for the

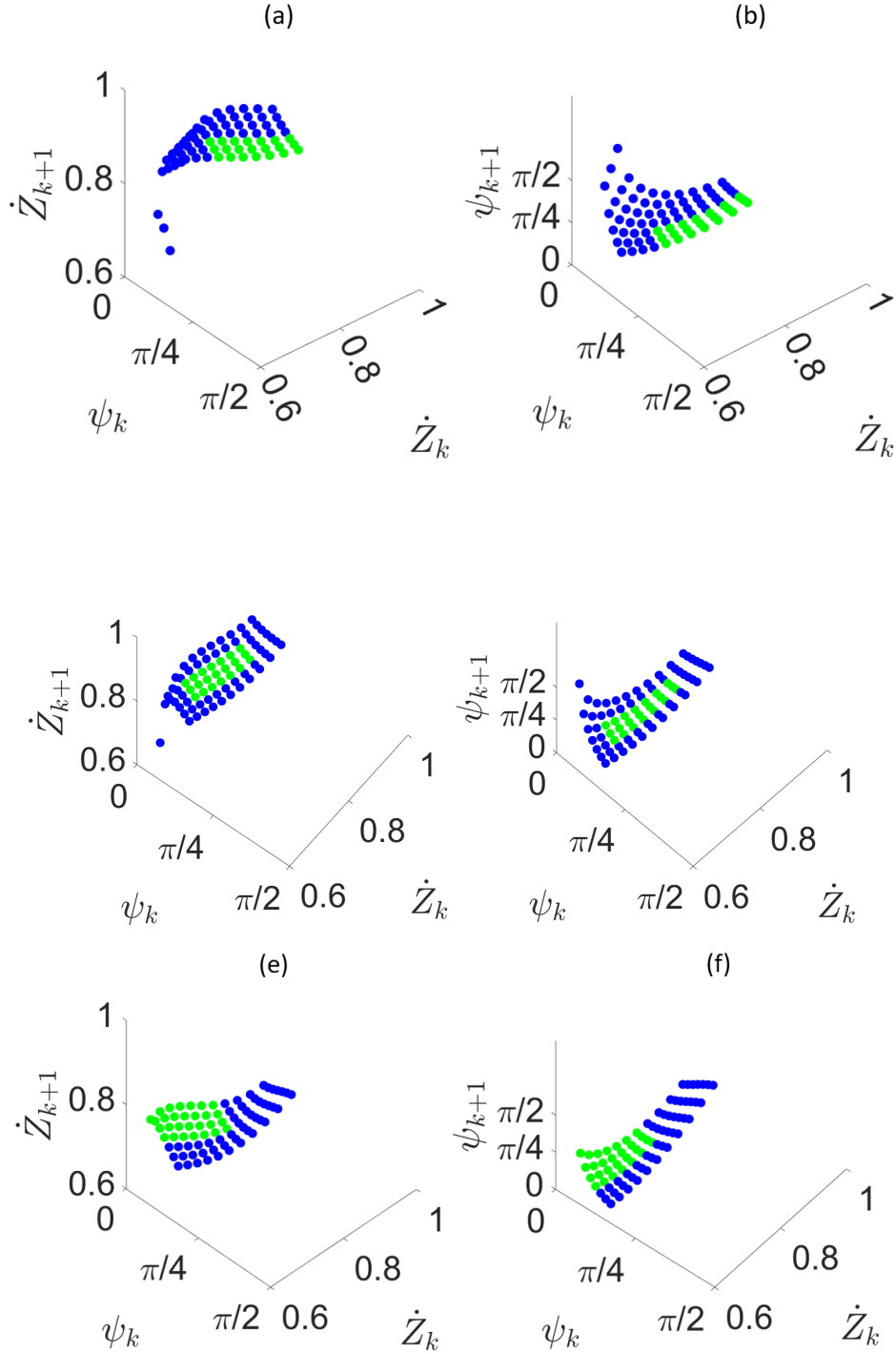


Fig. 25: Illustration of the location change of the subregions filtered by (4.2), as shown in green. The blue region surrounding it is the union of all such regions  $\cup_{d \in [0.26, 0.35]} \mathcal{R}_{1,2}$ , as described in (4.2). (a),(b):  $d = 0.35$ ; (c),(d):  $d = 0.30$ ; (e),(f):  $d = 0.26$ .

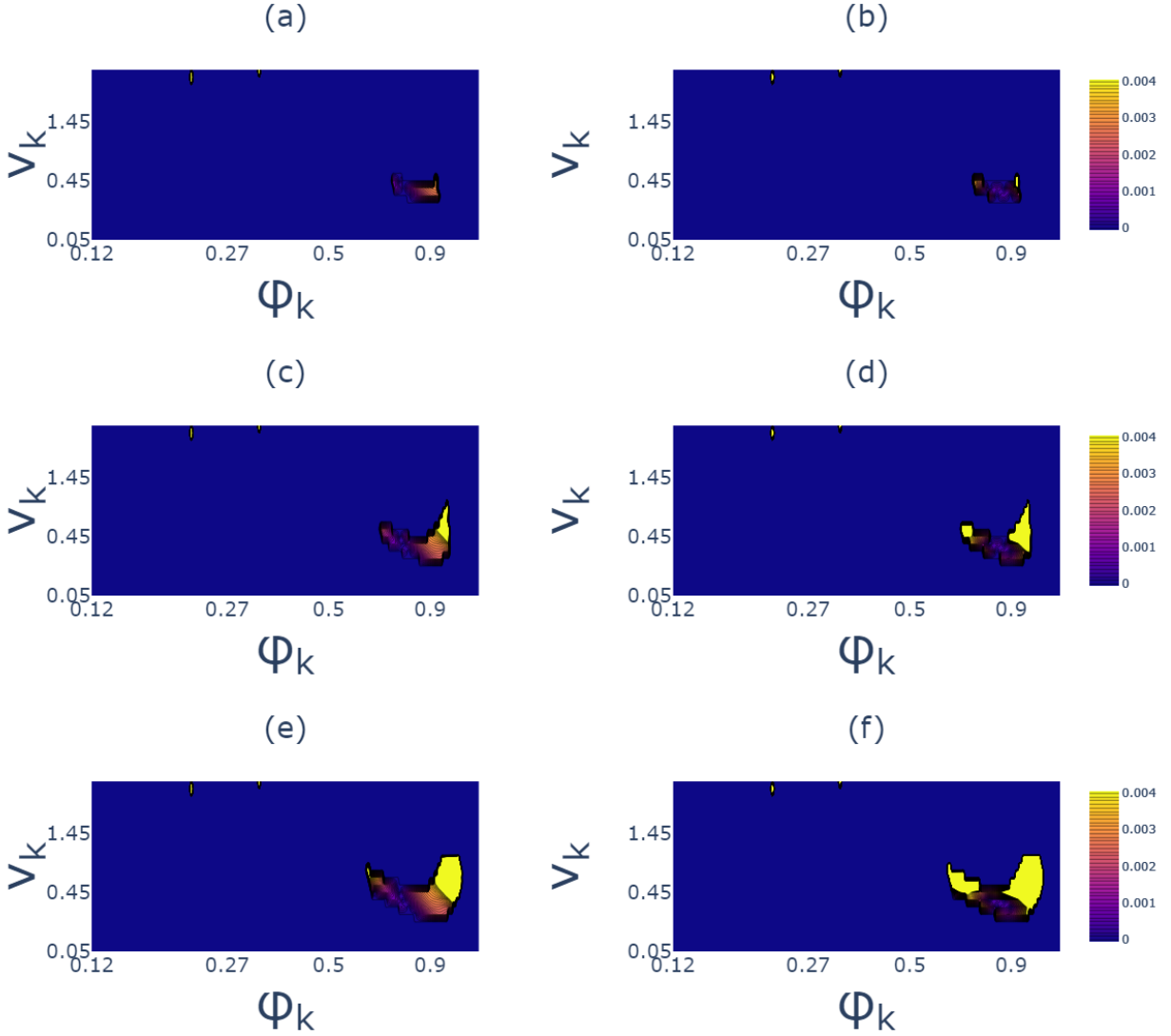


Fig. 26: Heat maps corresponding to the approximation error in Region  $\mathcal{R}_1$  with different  $\delta$  in (4.2). The approximation errors  $\epsilon_v = |\dot{Z}_{k+1} - v_{k+1}|$  are shown in (a),(c),(e) and  $\epsilon_\phi = |\psi_{k+1} - \phi_{k+1}|$  are shown in (b),(d),(f) for  $(\dot{Z}_{k+1}, \phi_{k+1})$  in the exact map and  $(v_{k+1}, \phi_{k+1})$  in the coupled 2-D approximate map (4.3)-(4.4) for  $\mathcal{R}_1$ . Note lighter colors indicate larger errors  $\epsilon$ . As  $\delta$  increases, the size of  $\mathcal{R}_1$  increases, which includes more variation that yields the larger approximation error. (a)-(b):  $\delta = 1.2$ ; (c)-(d):  $\delta = 1.3$ ; (e)-(f):  $\delta = 1.4$ , and  $d = 0.35$  in all panels.

1028 lower triangular surfaces in this region are given by

$$\begin{aligned}
1029 \quad v_{k+1}(v_k, \phi_k) &= f_3(v_k, \phi_k) = b_{300} + b_{301}\phi_k + b_{302}v_k + b_{303}\phi_k^2 + b_{304}\phi_kv_k + b_{305}v_k^2 + b_{306}\phi_k^3 + b_{307}\phi_k^2v_k \\
1030 \quad &+ b_{308}\phi_kv_k^2 + b_{309}v_k^3 + b_{310}\phi_k^3v_k + b_{311}\phi_k^2v_k^2 + b_{312}\phi_kv_k^3 + b_{313}v_k^4 + b_{314}\phi_k^3v_k^2 \\
1031 \quad &+ b_{315}\phi_k^2v_k^3 + b_{316}\phi_kv_k^4 + b_{317}v_k^5, \\
1032 \quad \phi_{k+1}(v_k, \phi_k) &= g_3(v_k, \phi_k) = a_{300} + a_{301}\phi_k + a_{302}v_k + a_{303}\phi_k^2 + a_{304}\phi_kv_k + a_{305}v_k^2 + a_{306}\phi_k^3 + a_{307}\phi_k^2v_k \\
1033 \quad &+ a_{308}\phi_kv_k^2 + a_{309}v_k^3 + a_{310}\phi_k^4 + a_{311}\phi_k^3v_k + a_{312}\phi_k^2v_k^2 + a_{313}\phi_kv_k^3 + a_{314}v_k^4 + a_{315}\phi_k^4v_k \\
1034 \quad (A.2) \quad &+ a_{316}\phi_k^3v_k^2 + a_{317}\phi_k^2v_k^3 + a_{318}\phi_kv_k^4 + a_{319}v_k^5.
\end{aligned}$$

1036 As discussed in Section 4.1, Iteration 1 steps iv) and vi), there is also a nearly vertical surface in this  
 1037 region, shown in Fig. 6. It represents strongly transient dynamics corresponding to rapid transitions from  
 1038 BB to BTB behavior, so we treat this as immediately transient. As a result, we use the lower triangular  
 1039 surface to capture the dynamics of this region, taking the map (A.2) over all of  $\mathcal{R}_3$ . We find that these  
 1040 surfaces do not shift or change shape with  $d$  varying. Therefore, the coefficients in (A.2) are constant instead  
 1041 of being functions of  $d$ .

1042 **A.7. Comments on Region  $\mathcal{R}_5$ .** Region  $\mathcal{R}_5$  corresponds to smaller  $\dot{Z}_k < 0.55$ , as in  $\mathcal{R}_4$ , and for  
 1043 larger  $\psi$ :  $2.5 < \psi_k < \pi$ . The dynamics in this region are BB motion instead of BTB motion, with the map  
 1044  $(f_5, g_5)$  based on a separable approximation as in  $\mathcal{R}_2$  and  $\mathcal{R}_4$ . The green curves in Fig. 27(a),(b) capture  
 1045 the dynamics on the surfaces for  $\dot{Z}_{k+1}$  and  $\psi_{k+1}$ , and are approximated with orange curves that give the  
 1046 separable maps

$$1047 \quad v_{k+1}(v_k) = f_5(v_k) = |b_{50}v_k^4 + b_{51}v_k^3 + b_{52}v_k^2 + b_{53}v_k + b_{54}|,$$

$$1048 \quad (A.3) \quad \phi_{k+1}(\phi_k) = g_5(\phi_k) = a_{50}\phi_k^3 + a_{51}\phi_k^2 + a_{52}\phi_k + a_{53}.$$

1050 The coefficients  $a_{5i}, b_{5i}, i = 0, 1, \dots, 4$ , are functions of  $d$ , with  $a_{54} = 0$  in  $\phi_{k+1}$ .

1051 Note there is a small nearly vertical area in the surface for  $\psi_{k+1}$ , similar to that observed in  $\mathcal{R}_3$  mentioned  
 1052 in Appendix A.6. As discussed in step vi) of Iteration 1 of the algorithm (Section 4), we treat this as  
 1053 immediately transient, taking the map (A.3) over all of  $\mathcal{R}_5$ .

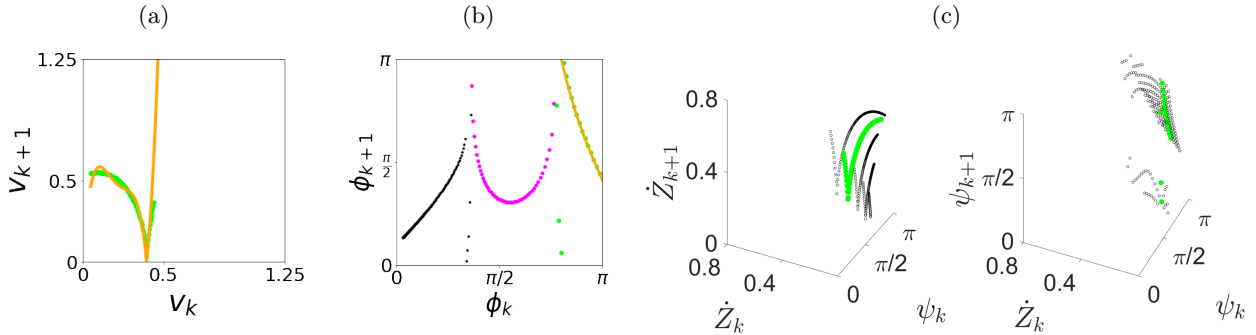


Fig. 27: Approximation of  $(Z_{k+1}, \psi_{k+1})$  in  $\mathcal{R}_5$  for  $d = 0.35$ , which has ranges  $\dot{Z}_k < 0.55$  and  $2.5 < \psi_k < \pi$ . Panels (a),(b) compare the orange curves for the approximate separable map (A.3) with the green curves in the corresponding phase planes. In panel (c), the green curves are generated with the exact map (3.1), giving a separable representation of the variation of the surface for fixed  $\psi_k = 3.05$  (left) and  $\dot{Z}_k = 0.12$  (right).

1054 **A.8. The pseudocode used in the programming the composite map.** Here, we provide the  
 1055 pseudocode for the approximate composite map for  $(v_n, \phi_n)$ , as used in Figure 12, with references to the  
 1056 bounds and maps for each region  $\mathcal{R}_n$ .

1057 **Algorithm: Composite map for  $(v_n, \phi_n)$**   
 1058 **if**  $\phi_k > \pi$  OR  $\phi_k < 0$ , **then**  
 1059 Reset as in Section 4.2, Iteration 1, step vi):  $\phi_{k+1} = 1.2$  and  $v_{k+1} = v_k$   
 1060 **else if**  $0.63 \leq v_k \leq 0.94$  AND  $0.15 \leq \phi_k \leq 0.45$ . **then**  
 1061 Use Region  $\mathcal{R}_1$  approximate maps (4.3)-(4.4):  
 1062 **else if**  $v_k > 0.63 - 0.53\phi_k$  AND  $v_k > 0.55$  AND  $(v_k, \phi_k) \notin \mathcal{R}_1$ , **then**  
 1063 Use  $\mathcal{R}_2$  approximate map (4.5):  
 1064 **else if**  $v_k > 0.63 - 0.53\phi_k$  AND  $1.1 < \phi_k < 2.5$  and  $v_k < 0.55$ , **then**  
 1065 Use  $\mathcal{R}_4$  approximate map (A.1):  
 1066 **else if**  $2.5 < \phi_k < \pi$  AND  $v_k < 0.55$ , **then**

```
1067     Use  $\mathcal{R}_5$  approximate map (A.3):
1068 else if  $v_k < 0.63 - 0.53\phi_k$ , then
1069     Use  $\mathcal{R}_3$  approximate map (A.2):
1070 end if
```